FACULTY OF SCIENCE AND TECHNOLOGY

MASTER'S THESIS

Study programme / specialisation: MSc. in Petroleum Engineering / Production and Process	The *Spring* semester, *2023* Open
Author: Imad Chidiac	
Supervisor at UiS: Prof. Zhixin Yu Co-supervisor: Prof. Sachin Maruti Chavan	
Thesis title: Low Pressure Adsorption of Carbon Dioxide and Nitrogen on Activated Carbon and Zeolite 13X	
Credits: 30 ECTS	
Keywords: Adsorption, Carbon Dioxide, Nitrogen, Isotherm, Activated Carbon, Zeolite 13X, Low Pressure, IAST, Selectivity, Heat of Adsorption	Pages: 69 + appendix: 8 Stavanger, *12/06/2023*

Acknowledgements

I would like to express my deepest thanks to both my advisors who have provided me with unwavering support. Professor Zhixin and Professor Sachin I sincerely appreciate your continuous effort towards making my experience throughout the semester as smooth as possible. In addition, I would like to extend my thank for Sanjay and Senith who have supported me throughout my lab work.

I am grateful for the opportunity to have been provided with samples from *Beyonder* the company, and for Obinna who has also been very supportive throughout my thesis work. I am grateful to every single person who has contributed to my success throughout my time at the University of Stavanger and especially for this thesis.

Finally, a message of appreciation for my parents Khalil and Marleine who have sacrificed so much for me to be able to have the best possible opportunities. I dedicate this thesis to them, my siblings Edmond & Lara, and to my late grandfather Jeddo Edmond who has paved the way and instilled the values and work ethic which I needed to succeed. Without them I would not be in the position that I am, and for that I will be forever grateful.

Abstract

Several gas separation techniques have been used throughout the year, however the most cost effective and energy efficient gas separation process to date is that of adsorption. Adsorption of carbon dioxide from flue or biogas streams is mostly done on activated carbons and zeolites.

In this study, carbon dioxide and nitrogen adsorption on activated carbon and Zeolite 13X samples were studied. The samples are consisted of three activated carbons synthesized by a battery company called Beyonder, in addition to a commercial activated carbon as well as a commercial zeolite 13X sample. The first part of the work is characterization of the samples using Scanning Electron Microscopy (SEM), Thermogravimetric analysis (TGA) and Nitrogen Physisorption for BET surface area and pore size distribution determination. Initial SEM data of the activated carbon samples has visually described size differences among the tested samples which were the cause of different activation intensities. In addition, the commercial activated carbon and zeolite 13X samples have shown more uniformity in their structure as compared to the non-commercial samples.

The carbon samples from Beyonder: SAC22-029, SAC21-037, and SAC21-050 were synthesized by the same base raw material and were shown to have surface areas of 931 m^2/g, 2158 m^2/g, and 2613 m^2/g respectively according to increasing activation intensities where SAC21-050 was subjected to the highest among the samples. Also, the commercial activated carbon sample YEC8B and the commercial Zeolite 13X sample have surface areas of 1672 m^2/g and 395 m^2/g respectively. In addition to relating higher surface area of the carbon samples to their higher activation intensities, pore size distribution of those samples was calculated based on the Non-Local Density Function Theory (NLDFT). The pore size distribution of SAC22-029, SAC21-037, and SAC21-050 were compared which has shown that increasing activation intensities results in an increase in micropore volumes up to a certain extent after which the increase in activation intensity resulted in the collapse of micropores into larger mesopores.

Due to the heavy load on the adsorption instrument, the adsorption measurements was only done on the highest surface area carbon and the zeolite 13X sample in order to compare the carbon dioxide adsorption capacities of both samples. Adsorption of nitrogen and carbon dioxide was tested on both samples at three different temperatures and has shown SAC21-050 to have a higher adsorption capacity of nitrogen at all temperatures compared to zeolite. The activated carbon sample recorded a maximum capacity of 9 cm^3/g at 283.15K as compared to zeolite having 6.5 cm^3/g. In contrast, zeolite 13X has shown a significant superiority of adsorbing carbon dioxide when compared to the activated carbon sample. The zeolite sample shows a maximum capacity of 92 cm^3/g at 283.15K as compared to that of activated carbon having a maximum of around 65 cm^3/g. The difference in performance will be explained as being a cause of the surface chemistry differences between the two types of samples, their pore size distribution, their heat of adsorption, and their CO_2/N_2 selectivity.

The experimental data was fitted with the Langmuir and the Dual-Site Langmuir-Freundlich adsorption models where the latter has proven to be more accurate at representing the data. As a result, the DSLF model was chosen for further Ideal Adsorbed Solution Theory selectivity calculations due to the inclusion of the surface heterogeneity constant.

Zeolite 13X was determined to have a higher selectivity for carbon dioxide over nitrogen and a higher heat of adsorption making it more suitable for carbon dioxide separation. Taking into consideration some constraints of zeolite which includes its hydrophilic nature that will adhere its adsorption capability.

Table of Contents

Table of Figures

List of Tables

Abbreviations

GHG – Greenhouse Gases

AC – Activated Carbon

MOF – Metal Organic Frameworks

PSA – Pressure Swing Adsorption

TSA – Temperature Swing Adsorption

CCS – Carbon Capture and Storage

BET – Brunauer-Emmett-Teller

SEM – Scanning Electron Microscopy

XRD – X-Ray Diffraction

TGA – Thermogravimetric Analysis

HP – High Pressure

LP – Low Pressure

NLDFT – Non-Local Density Function Theory

IAST – Ideal Adsorbed Solution Theory

1. Introduction

Global Warming has been one of the most highlighted issues that the world is currently facing due to the growing demand for energy. Fossil fuels such as coal, natural gas, and crude oil have been the main source of energy for decades [1]. This reliance on fossil fuels has consequently contributed to almost 75% of all carbon, methane and other greenhouse gas emissions [2]. It goes without question that the future of the energy sector is transitioning towards low-carbon emission processes.

1.1. Carbon Dioxide and Global Warming

Throughout the years Carbon Dioxide emissions has been on the rise due to several reasons which include growth in population and increased human activity that spans across different sectors which includes the energy sector [3]. This dependence on energy is likely to continue for several more decades regardless of the world shifting towards more carbon-free processes. However, this highlights today's most challenging task and that is reducing carbon dioxide emissions through more sustainable and energy efficient processes [4]. Failure to do so will certainly have both short- and long-term irreversible effects that will impact the quality of life of every living creature on the planet. Among the consequences of increased GHG emissions includes the melting of glaciers, increased flooding and abnormal rainfall, increased probability of hurricanes and natural disasters [5]. The term "Global Warming" is a natural effect that is necessary for everyone's survival, without the GHG effect the earth's temperature would decrease to -21 degrees Celsius [6]. However, it is the increased levels of greenhouse gas emissions which includes CO2, that will further trap excess heat and increase the earth's temperature beyond the normal limit. In the past 100 years, the average temperature of the earth has increased by 0.74% and is projected to dramatically increase to 6.4% by the end of the 21st century [7].

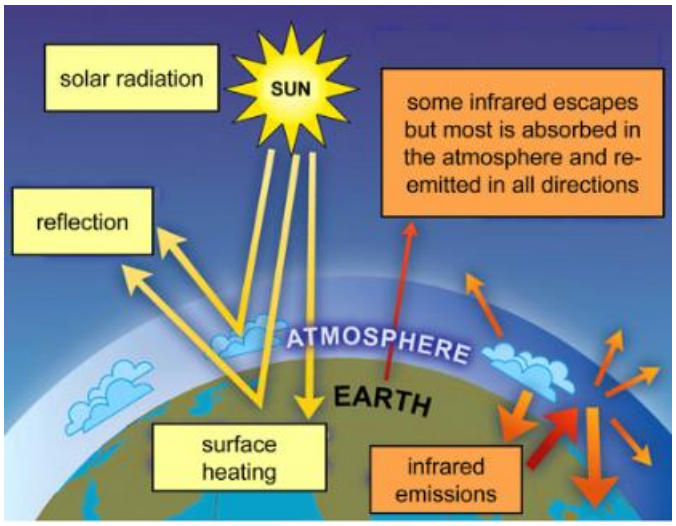

Figure 1. The Greenhouse Gas Effect [6]

The greenhouse gas effect is depicted in **figure 1** above where solar radiation passes through the atmosphere without any obstacles which provides heat to the earth's surface. Next, the heat is reflected as "infrared" heat which gets absorbed by the water vapor and carbon dioxide gas that surrounds the

earth's atmosphere. The more CO2 emitted into the blanket of gas in the earth's atmosphere, the more heat is trapped thus increasing the earth's temperatures gradually [6].

1.2. Carbon Dioxide

Among the above-mentioned methods for carbon dioxide separation, activated carbons and zeolites will be tested in this study and these samples consist of a cluster of micropores and mesopores. Thus, to really understand how effective these different carbon and zeolite samples will perform in the adsorption of the carbon dioxide molecules, the molecular size of carbon dioxide must be taken into consideration. The molecular size will give an insight on whether it will be difficult for carbon dioxide molecules to fit in the different pore sizes of the different tested samples.

Molecule	Molecular Weight	Kinetic Diameter (Å)
CO_2	44	3.3
O_2	32	3.46
N_2	28	3.64
H_2O	18	2.65
CH_4	16	3.8
H_2	2	2.89

Table 1. Molecular size and weight of different gases [8]

As shown in **Table 1**, carbon dioxide has a molecular size of 0.33 nm which is an important factor to consider later when the samples are characterized and tested for adsorption. There are several methods in which gases can be separated which includes PSA, TSA, membrane, and cryogenic separation techniques. Particularly, PSA is a very flexible operation where it can also be used to segregate and selectively capture carbon dioxide for CCS operations, considering CO_2 is one of the largest greenhouse gas contributors. Other greenhouse gas emissions are due to the flaring or venting of methane gas for example, where methane concentrations in the year 2021 have reached a record high [9]. In addition, traditionally and up until today large-scale bulk gas separation is done through amine units and wet scrubbing applications [10], [11]. These traditional processes have proven to leave a significant carbon footprint which has prompted the industry to look for more sustainable solutions. Thus, in the pursuit of developing more sustainable applications, separation, and purification of industrial gas streams via adsorption has been a key area of study in publications during the past two decades. The rise in interest in this area of study is linked not only to the importance of testing and developing efficient processes to selectively purify/separate undesired gases, but also due to the high availability of solid adsorbents [12]. Several solid adsorbents such as AC, zeolites, silica gels, and MOFs have been studied and applied to the different mentioned gas separation technologies in the energy industry today. **Figure 2** below illustrates the different types of technologies associated with CCS as well as Carbon Dioxide gas separation methods.

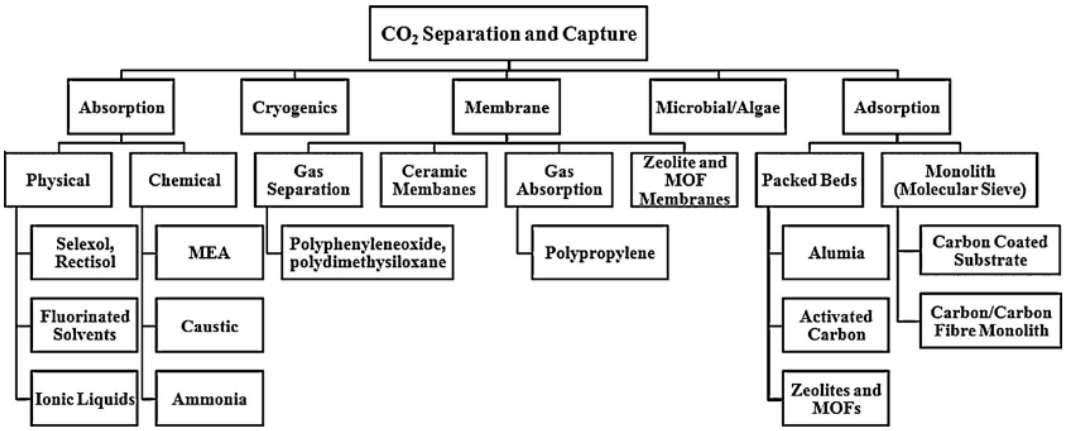

Figure 2. CO2 capture and separation available technologies [4]

The existing CO2 capture technology today is highly expensive and energy demanding which highlights the importance of developing and enhancing more efficient processes [13]. Considering the wide range of solid adsorbents, the focus in this study will include four different types of activated carbon samples as well as a commercial zeolite 13X sample. Knowing this, in the following section we will look at the phenomenon known as adsorption to better understand the basics of what makes solid adsorbents so important for gas separation.

1.3. Aim of the Thesis

The scope of this study is firstly accurately characterizing the different solid adsorbents with the potential of being effective in CO2 capture and gas separation applications. The characterization will consist of having a closer look at the pore structures of the samples using a scanning electron microscope (SEM). In addition, further characterization of the samples will include low nitrogen physisorption for BET surface area and pore size distribution measurements. This will help determine the different pore sizes and give a wider perspective as to which solid will have a more suitable structure to accommodate carbon dioxide molecules. Also, the final part of the characterization will include thermogravimetric analysis which will allow us to gain insight on the thermal stability of these solids under high temperature conditions.

After characterization of the different samples, two of the samples will be tested for low pressure adsorption with carbon dioxide and nitrogen using the gas adsorption instrument (Microtrac BELSORP MAX II) for differentiating the adsorption performance, determining the heat of adsorption, and performing IAST selectivity analysis. The highest surface area carbon sample as well as the Zeolite 13X sample are selected to test for both carbon dioxide and nitrogen at three different temperatures (283.15K, 293.15K, and 303.15K) for pressures of up to 1 bar. This choice in structure for the experimental testing is due to the limited number of measurements I was able to perform since many other students also use the same instrument for their projects and it is not always readily available.

The following key evaluations will be made:

- Successfully characterizing the samples and analyze the difference in surface area and pore size distributions and the reasons behind the differences.
- Obtain adsorption isotherm data for both nitrogen and carbon dioxide for the highest surface area sample (SAC21-050) as well as Zeolite 13X at three temperatures and determining which is more suitable for CO_2 adsorption.
- Fitting the experimental data with the Langmuir and Dual-Site Langmuir Models and selecting the most accurate model for IAST selectivity analysis.
- Combining the characterization data, adsorption data, selectivity as well as the heat of adsorption data to determine the difference between activated carbons and zeolite 13X for carbon dioxide adsorption applications.

2. Literature Review

2.1. Adsorption Isotherms and Hysteresis

The adsorption process is generally dependent on the properties of both the gases being adsorbed as well as the properties of solid adsorbents used. For the gas, it is important to understand its chemical structure, molecular size as well as electron configuration [14]. For the solid adsorbent, it is equally important to understand its chemical nature, pore size, and pore size distribution. In addition, pressure and temperature conditions will also influence the rate at which a gas adsorbs on a solid surface. The adsorption process can be either chemical (chemisorption) or physical (physisorption) where chemisorption results in much stronger bonds (higher heat of adsorption).

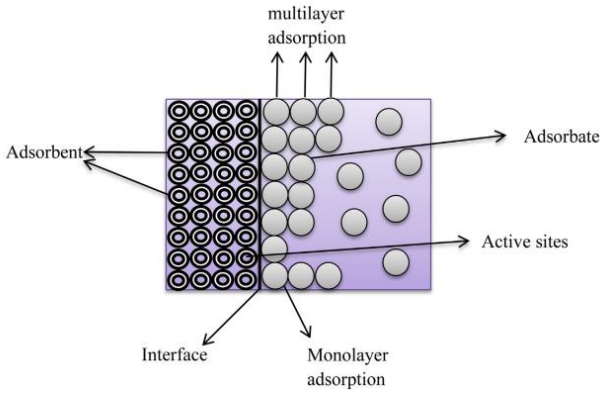

Figure 3. Adsorption Schematic on a Solid [15]

Physisorption is a phenomenon that happens when gas molecules form a bond with a solid surface due to the unbalanced forces between them [16]. Different types of gases have different affinities, which means the tendency of unlike species (gases and adsorbents) to form a bond. Adsorption of a gas on a porous material (i.e. solid adsorbents) is described quantitatively by an adsorption isotherm, which by definition is the amount of gas adsorbed by the solid adsorbent at varying pressures and a constant temperature [17]. There are several different adsorption models that describe the adsorption behavior of gases depicted in **figure 3**. The Langmuir model for example assumes a monolayer coverage as seen above, while other models describe dual-layer such as the Dual-Site Langmuir Adsorption model or other multilayer adsorption models.

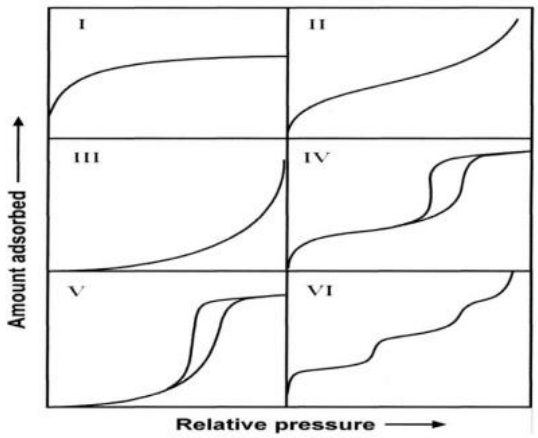

Figure 4. The IUPAC classification of Adsorption Isotherms (adsorption and desorption pathways) [17]

Adsorption isotherms follow the International Union of Pure and Applied Chemistry (IUPAC) classification system as seen in **figure 4** above. Along with the classification of isotherms, the behavior of isotherms is also related to the predominant pore sizes of the solid adsorbents. Thus, porous materials are also classified through IUPAC [17]:

- Microporous: up to 2.0 nm → Type (I)
- Mesoporous: between 2.0 – 50 nm → Types (IV, V)
- Nonporous and Macroporous: exceeding 50 nm → Types (II, III, VI)

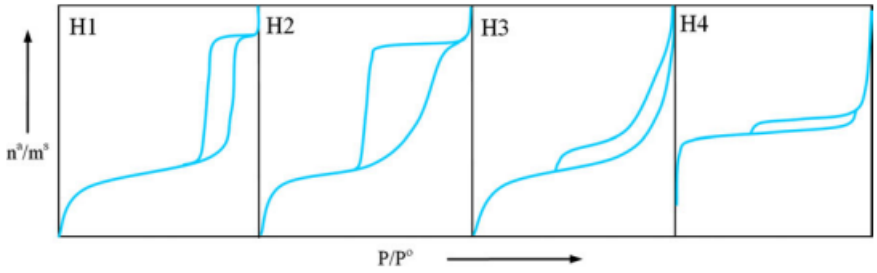

Figure 5. The IUPAC classification of Adsorption Hysteresis Loops [18]

In addition to the types of adsorption isotherms, hysteresis loops should also be taken into close consideration when looking at adsorption data. There are four types of hysteresis loops as classified by the IUPAC shown in **figures 5-6**. The type H1 loop is for solids that is characterized in having uniform pore sizes and shapes. Type H2 loop is for solids having what is called an “ink-bottle-shaped” pore structures where the pore opening is smaller than the inner pore structure itself. Type H3 is characterized for solids having a variation of different pore structures. Finally, the type H4 hysteresis loop is for a structure having few mesopores which are in turn limited by micropores [18].

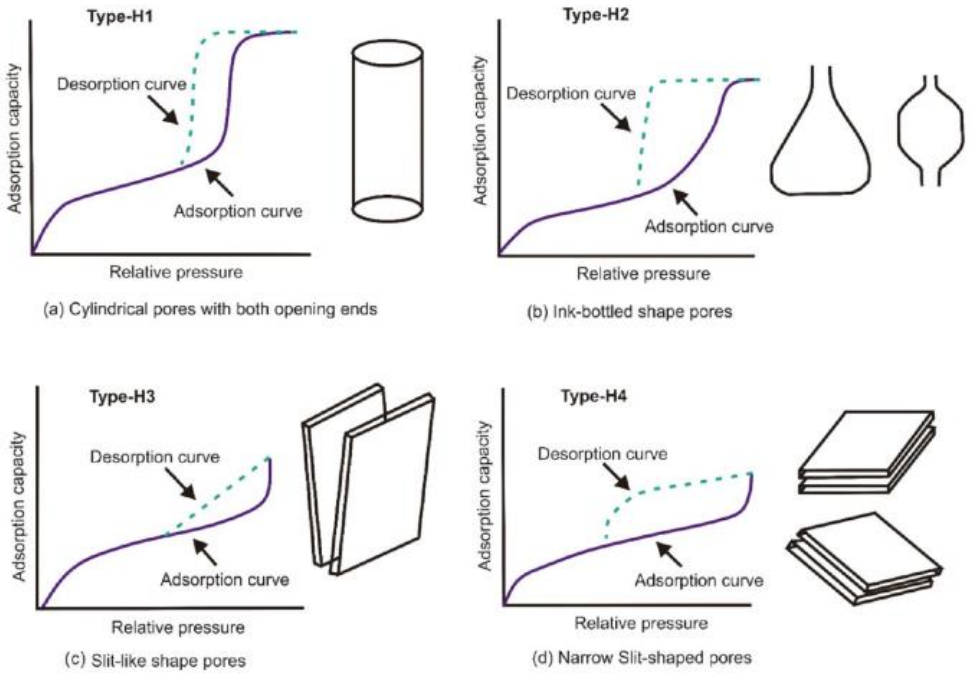

Figure 6. Pore Types corresponding to Hysteresis Loops [19]

2.1.1. Isosteric Heat of Adsorption

To fully understand the adsorption behavior of a gas on a solid adsorbent, the isosteric heat of adsorption must be taken into consideration. The adsorption process is an exothermic one, where heat is released due to the difference in energy states between the gas phase (lower energy state) and the adsorbent phase (higher energy state). This thermodynamic parameter is essential when it comes to practical gas separation processes, where the isosteric heat of adsorption ultimately governs the separation performance of the adsorption process [20]. The isosteric heat of adsorption is typically measured in one of two ways which are [21]:

i. Measured directly using calorimeter
ii. Measured indirectly through adsorption isotherms at different temperatures

In the literature, direct measurement using calorimetry is rarely used compared to using adsorption isotherms by means of the following Clausius-Clapeyron Equation [22]:

$$q_{st,i} = RT^2\left(\frac{\partial lnP}{\partial T}\right)_{n,i} \quad (1.1)$$

Where (R) is the universal gas constant, (T) is the system temperature, and (n) is the amount of gas adsorbed. When using the Clausius-Clapeyron equation, it is important to note that there are certain assumptions to be aware of which include [21]:

i. Bulk phase gas is assumed to behave ideally
ii. Volume of the gas phase is much larger compared to volume of adsorbed phase making it negligible

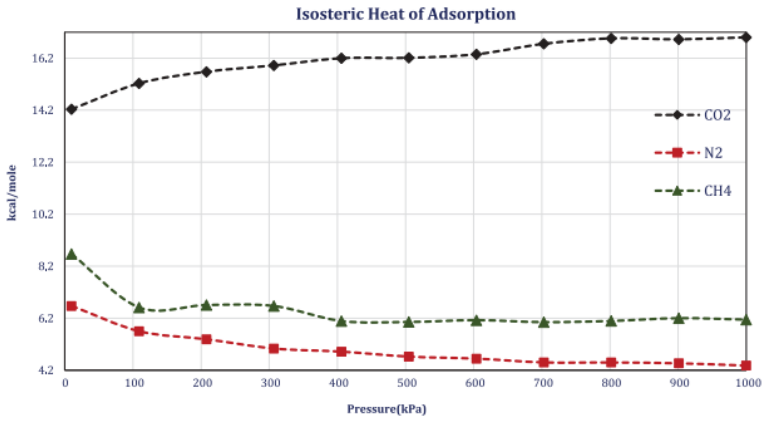

Figure 7. Simulation results of isosteric heat of adsorption of CO2, N2, and CH4 pure gases on zeolite 13X from [20]

A higher value of the isosteric heat of adsorption indicates a higher selectivity of the specific gas to the solid adsorbent. As an example in **figure 7** above, the selectivity of carbon dioxide is clear over nitrogen and methane [20]. The magnitude of the heat of adsorption will determine the affinity of the pore surface towards the carbon dioxide molecules, thus playing a crucial role in determining the adsorptive selectivity as well as the energy required for the regeneration process [23]. In other words, the isosteric heat of adsorption is a representation of the strength of the interaction between adsorbate and adsorbent molecules [10],[24]. When considering calculating the heat of adsorption using different adsorption isotherms, it is essential to note the existing isotherms in the literature. The adsorption isotherms combined with the Clausius-Clapeyron equation mentioned above will allow us to calculate the heat of adsorption. A more practical version of the above equation is used for manual calculations and is in the form of equation (1.2) [25]:

$$Q_{st} = RT_1T_2\frac{\ln\left({}^{P_2}/_{P_1}\right)}{T_2-T_1} \quad (1.2)$$

2.1.2 Langmuir Isotherm Model

The Langmuir Adsorption model as a definition describes monolayer coverage of gases on the surface of the adsorbent. The model was developed in 1918 by Langmuir where the model he proposed was based on several assumptions which included [22]:

i. The rate of adsorption is equal to the rate of desorption
ii. The adsorbed molecules have no intermolecular interactions between them
iii. Each site on the adsorbent can have only one molecule adsorbed to it
iv. Adsorption occurs on a homogeneous surface, where adsorption energy is constant across all sites

Based on the above assumptions, the Langmuir Adsorption Model can be expressed using the following equation [26]:

$$\theta = \frac{KP}{1+KP} \quad (2)$$

Where (θ) is the occupancy of adsorbed sites, (K) is the Langmuir constant, and (P) is the pressure. It is important to note that the Langmuir constant (K) is independent of the Pressure (P), and only the temperature is the influence. Thus, (K) can be determined experimentally [22]. The Langmuir constant can be expressed by the Van 't Hoff Equation as follows [21]:

$$K_i = K_i^o \exp\left(\frac{E_i}{RT}\right) \quad (3)$$

Where (K_i^o) is called the pre-exponential factor and (E_i) is the adsorption energy. Applying the Clausius-Clapeyron equation described by equation (1.1) with the Langmuir Adsorption model, the pure isosteric heat of adsorption can be described by the following equation [21]:

$$q_{st,i} = E_i \quad (4)$$

Equation (4) along with **figure 8** below shows that the isosteric heat of adsorption when using the Langmuir Adsorption model remains constant.

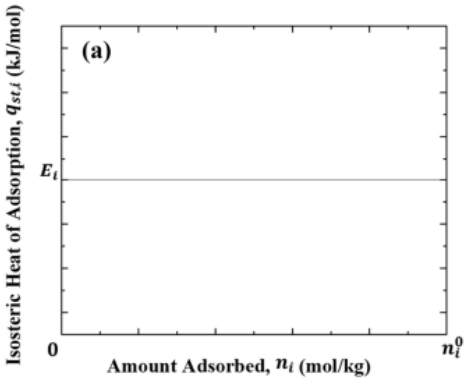

Figure 8. Isosteric Heat of Adsorption for Langmuir Adsorption Isotherm Model [21]

2.1.3. Toth Isotherm Model

The Toth Adsorption model is quasi-Gaussian energy distribution model that is considered one of the most reliable in representing the adsorption of gases on both low and high pressure conditions [27]. The Toth isotherm is expressed as equation (5):

$$n = \frac{abp}{\left[1+(bp)^f\right]^{1/f}} \quad (5)$$

Where the saturation capacity and the affinity parameter are expressed as the terms ***a*** and ***b*** respectively [22]. Unlike the Langmuir model, the Toth model includes the temperature dependent surface heterogeneity parameter expressed as equation (6) [21]:

$$f = f^o + \frac{\beta}{T} \quad (6)$$

When the surface heterogeneity parameter is equal to 1 (i.e., f = 1), the Toth isotherm expressed in equation (5) is reduced to the Langmuir Isotherm as depicted in **figure 9** below.

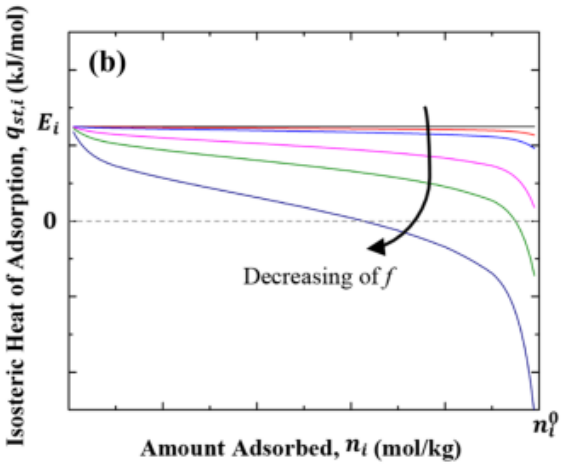

Figure 9. Isosteric Heat of Adsorption for Toth Adsorption Isotherm Model [21]

2.1.4. Freundlich Isotherm Model

The Freundlich Isotherm model is used to describe multilayer adsorption behavior on heterogeneous surfaces unlike the Langmuir Isotherm. The assumption in this model is that there is a nonuniform affinity and heat of adsorption towards the heterogeneous surface where the interaction occurs [28]. Thus, the model is expressed by equation (7):

$$q_e = bC_e^{1/n} \quad (7)$$

Where the adsorption capacity is denoted by "b" in L/mg and the term "1/n" describes the surface heterogeneity which in turn determines whether adsorption is favorable or not:

- 0 < 1/n < 1 → Favorable Adsorption
- 1/n > 1 → Unfavorable Adsorption
- 1/n = 1 → Irreversible Adsorption

The linearized form of the above equation can be expressed as equation (8):

$$\ln q_e = \ln b + \frac{1}{n} \ln C_e \quad (8)$$

By using $\ln q_e$ versus $\ln C_e$, the linearized form of the Freundlich model can be plotted having the slope "$\frac{1}{n}$" and the y-intercept as "$\ln b$" [28].

2.1.5. Dual Site Langmuir-Freundlich Isotherm Model

The DSLF model is based on the same assumptions as the Langmuir model, yet in comparison takes into consideration the surface heterogeneity factor. In addition, this model assumes gas adsorption on two sites instead of one as compared to the Langmuir model where each site has its own adsorption energy. The DSLF model is expressed by equation (9):

$$N = N_1^{max} \times \frac{b_1 p^{1/n_1}}{1 + b_1 p^{1/n_1}} + N_2^{max} \times \frac{b_2 p^{1/n_2}}{1 + b_2 p^{1/n_2}} \quad (9)$$

Where p is the pressure (kPa), N is the adsorbed amount per mass of adsorbent (varies depending on the units used). The saturation capacities are denoted by N_1^{max} and N_2^{max} of the two sites (same unit as N). The affinity coefficients are denoted by b_1 and b_2 for the two sites (1/kPa). The terms n_1 and $n_2$are the deviation constants from a homogenous surface of a solid [29].

2.2. Solid Adsorbents

Understanding the basics of adsorption of gases on solid adsorbents is one essential pillar in the adsorption process. In addition to that, different types of solid adsorbents are going to be tested. Among the solids that are of interest mentioned in the literature for adsorption of CO_2 are AC, zeolites, and MOFs [30].

2.2.1. Activated Carbon

Since the 1920's the production of large-scale activated carbons has increased gradually increased due to its low cost, high porosity, high surface area, and high adsorption capacity [31]. Activated carbons are prepared from a wide range of carbon types consisting of different carbon structures. It is the porosity, overall structure, method of preparation, and activation (physical or chemical) of the chosen carbon material that will eventually determine its efficacy during adsorption processes [32]. The production of AC can occur through different types of raw material ranging from waste tires (non-organic) to agricultural by-products (organic) such as peanut shells and walnut shells for example [31],[33]. The selection of appropriate raw material before producing activated carbons is a crucial matter since the composition of the material structure such as carbon, nitrogen, hydrogen, oxygen, and sulfur will influence the physiochemical properties of the AC [34]. Physical adsorption on carbonaceous solid adsorbents have been studies in the literature for separation, purification, and gas storage purposes [35].

AC are porous solids with high versatility in CO_2 adsorption applications as a result of their surface chemistry and structural properties [30]. AC consist of a graphite-like structure that are characterized with a high degree of structural disorder [36]. In addition, an ideal graphite structure consists of fused hexagons held apart by Van Der Waals forces which through their varying lengths and widths ultimately create the cavities known as the pore structures as seen in **figures 10-11** below [37].

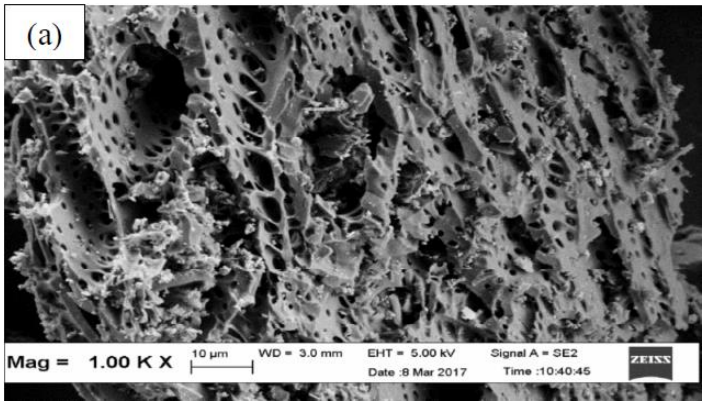

Figure 10. SEM image of AC pore structure from activated palm kernel shell [36]

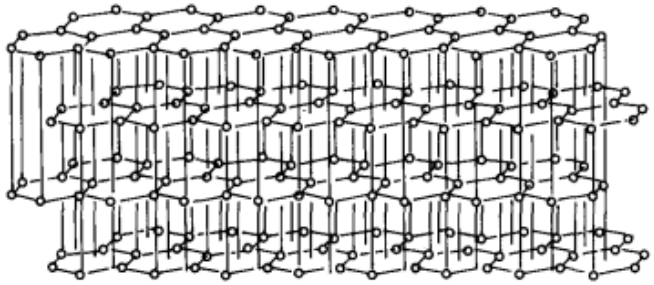

Figure 11. Schematic representation of graphite structure [37]

As mentioned earlier, the chemical characteristics of AC are determined by the presence of heteroatoms (i.e., atoms present that are not carbon). Surface functional groups which are formed by these heteroatoms determine the acidic or basic nature of the AC as shown in **figure 12** below. Functional groups containing oxygen is linked to the nature of the AC as being acidic. Considering the outer functional groups are what make up a major part of the adsorption surface, the adsorption capacity will thus be affected by the concentration of oxygen on that surface. Oxygen on the surface of the AC can be in the form of lactone, carbonyl, carboxylic, and ether groups. These oxygen groups are formed by means of oxidation via gases (CO_2, air, steam, and oxygen gas) or liquid oxidants. In comparison, functional groups containing nitrogen are linked to the basicity of the AC surface. The presence of nitrogen functional groups increases the adsorption capacity of activated carbons in the process of adsorbing carbon dioxide, mainly because of an increase in the volume of the micropores as well as increased basicity [38]. The nitrogen is introduced by means of reacting the AC with reagents such as amines, nitric acid, and NH_3 or by nitrogen containing precursors used for activation. The interaction between AC and acid molecules is enhanced by the presence of the nitrogen functional groups [11].

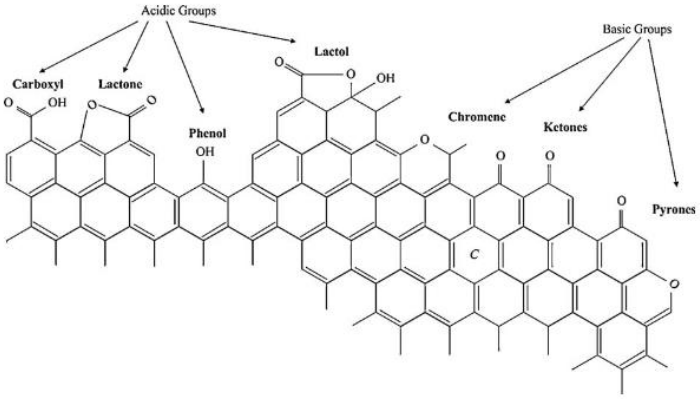

Figure 12. Acidic and basic functional groups on AC [11]

The ability of the AC to effectively adsorb the desired gases such as carbon dioxide and methane depends on the internal accessibility of those gases to the surface. The pore shape, size, and volume and their distribution will ultimately define the adsorption capacity of the AC in practice [37]. In addition, the level of contamination present in the pores will also play a role in the adsorption capacity. Since most of the adsorption process happens within the micropores, with higher contamination levels usually requires a higher contact time for adsorption [31]. The amount of contaminants such as ash is related to the raw material that was used as a precursor [37].

2.2.2. Zeolite 13X

Zeolites are based on silicate frameworks where the substitution of some of the Si with Al (or other metals) results the framework to having a negative charge, and having cations such as Na or other alkali/alkaline earth metals within the pores [39]. These cations can be exchanged to modify the pore size, thus influencing the adsorption characteristics based on the desired application. A decrease in the Si/Al ionic ratio of the zeolite results in a negatively charged surface which has shown to be more suitable for CO_2 adsorption [40]. Zeolites have a high thermal as well as chemical stability which makes it a promising subject to investigate.

Specifically, zeolite 13X has a considerable high surface area which has shown promising capabilities in CO_2 adsorption applications [23].

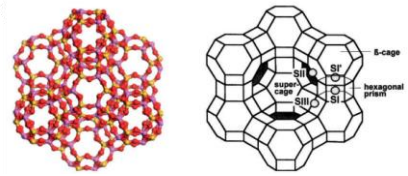

Figure 13. Structural Diagram of Zeolite 13X [41]

Zeolites have a defined crystalline cage-like structures as shown in **figure 13** having a uniform pore size in intervals of 0.5 to 1.2 nm which allows the zeolite to separate molecules by the molecular sieving effect [42]. Physical adsorption of microporous zeolite 13X has been reported to have a high adsorption capacity of CO_2 at ambient temperature conditions, however also requiring high energy requirements for the regeneration of the solid adsorbent [43].

The efficient adsorption of gases on zeolites is dependent on several factors which includes: size and shape of the molecules, structure and composition of the zeolite framework, cationic species in pore structure, charge density, purity, and molecular polarity [39],[44]. The behavior of CO_2 adsorption on the different forms of zeolites (3A,4A,5A, and 13X) depends on the pore sizes in which their names are based upon. In other words, CO_2 adsorption for larger pore zeolites (13X) depends on the electrostatic forces between the surface and gas. In comparison for smaller sized pore Zeolites (3A,4A), the adsorption behavior is due to a sieving effect (exclusion based on size) [40].

2.2.3. Metal Organic Frameworks (MOF)

MOFs are a class of porous materials that are synthesized by self-assembly of organic ligands and metal oxide clusters [43]. Specifically, they are considered as organic-inorganic hybrid solids with infinite and uniform framework structures built from organic linkers and inorganic metal nodes or metal containing clusters [45]. The synthesized crystalline material results in a high surface area, high pore volume, and regular porous structures and size [43].

The structure of MOFs varies depending on which organic ligands as well as inorganic metals used during the synthesis process. Among the most-researched MOFs to date is the $Zn_4O(BDC)_3$ (MOF-5) compound shown in **figure 14** below. This type of metal organic framework consists of tetrahedral $[Zn_4O]^{6+}$ clusters that are bridged by ditopic BDC^{2-} ligands that in turn form a cubic 3D network [23].

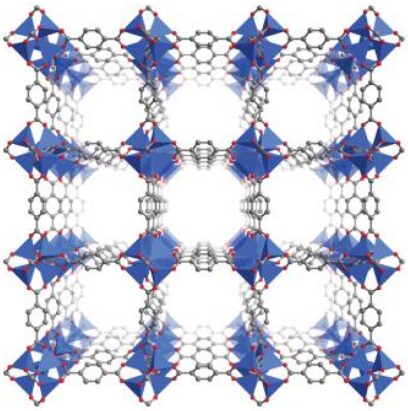

Figure 14. Crystal structure of Zn4O(BDC)3 (MOF-5). Blue tetrahedra represent ZnO4 units, while gray and red spheres represent C and O atoms, respectively [23]

In addition, another family of material has also been linked to have shown selective adsorption properties for CO_2 over other gases such as methane. One of these materials is the Al(OH)(BDC) (MIL-53) structure type MOF shown to the left in **figure 15** below along with its respective adsorption isotherm of CO_2 over Methane to the right.

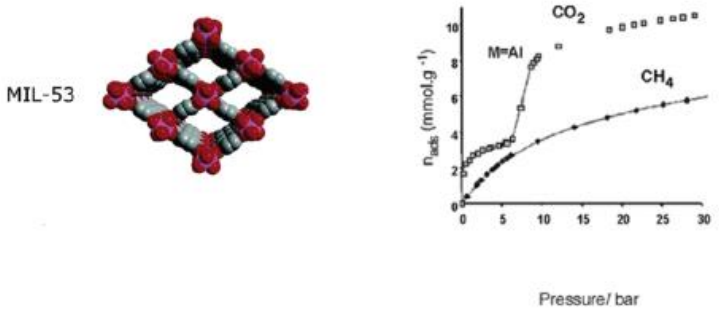

Figure 15. LEFT: Structure of MIL-53 (space-filling model; metal atoms are shown in pink, carbon atoms in black-gray, oxygen atoms in brown; H atoms omitted for clarity (left). RIGHT: Adsorption isotherms of CO2 and CH4 on MIL-53 at 304 K [45].

MOFs are of interest due to the ability to incorporate and modify organic linkers that will allow controlling pore size, pore shape and chemical potential of the adsorbing surface which will ultimately influence selectivity, kinetics, and adsorption capacity [39].

2.3. Materials Characterization

2.3.1. XRD

XRD is a common characterization method for solid adsorbents which provides key data which includes sample purity, phase identification, crystal size, and in certain cases morphology. The information obtained from XRD can be complimentary used with other microscopic and spectroscopic data [46]. The discovery of X-Ray diffraction in crystals dates to the year 1912 by Laue, Friedrich and Knipping in Munich. The development of the technique came after in the years preceding the First World War by W.H Bragg and W.L Bragg [46]. The development of the well-known Bragg's law is credited to the son (W.L Bragg) where he envisaged crystals in terms of layers or planes (assuming the angle of incidence is equal to the angle of reflection) instead of a three-dimensional network of rows of atoms which was the earlier work

of Lauer. Although Bragg's approach as shown graphically in **figure 16** is incorrect in the physical sense, it is correct in the geometrical sense and thus provided us with the Bragg Law Equation below [47]:

$$n\lambda = 2 \times d \times sin\theta \quad (10)$$

Where (λ) is the wavelength, (n) is the order of reflection, d is the lattice plane spacing, and (θ) is the angle of incidence/reflection to the planes.

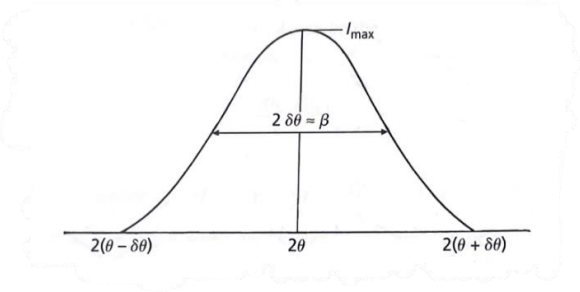

Figure 16. Schematic diagram of a broadened Bragg peak arising from a crystal of finite thickness [47]

The Scherrer equation is applied to the broadening from polycrystalline (powder), hence the name Powder X-Ray Diffraction. When crystallite size decreases from bulk size to nanoscale, the XRD peaks become broader [46]. Equation (11) below includes a correction factor K (usually considered to be 0.9, but can vary with different morphology of crystals) which accounts for particle shapes thus giving the simplified equation below:

$$D = \frac{K\lambda}{\beta cos\theta} \quad (11)$$

Where (D) is the width of the peak at half-length, and it is important to note that the diffraction angle (θ) in the Scherrer equation is used in radians (not in degrees).

2.3.2. Nitrogen Physisorption

The nitrogen physisorption is based on a simplified model of physisorption like that of Langmuir's theory where the surface of the adsorbent is considered as an array of equivalent sites and adsorption is done in a random manner. The assumption is based such that there are no interactions between molecules adsorbed on neighboring sites. Thus, the molecules in the first layer will act as sites for molecules in the second layer, and the same goes on for the higher number of layers. Even though the stated assumption allows no intermolecular interaction, the sites above the first layer are considered to have liquid-like properties [48].

The BET surface area determination from adsorption, which was developed in 1938, applies to the isothermal adsorption of nitrogen at a temperature of 77K. It acts as an extension for the Langmuir theory to further describe multilayer adsorption on surface of materials. The BET theory is based on equating the condensation rate of a single layer of adsorbate on a surface, to the desorption rate of the previous monolayer coverage on that surface [49]. Thus, the BET theory is based on the following equation:

$$\frac{n}{n_m} = \frac{CP}{(P-P_o)[1+(C-1)\left(\frac{P}{P_o}\right)]} \quad (12)$$

Where n (the amount of gas adsorbed), and P (the pressure) are parameters that are measured. The fitting parameters are P_o (vapor pressure of adsorbate), n_m (monolayer coverage), and C (attributed to the interactive strength between adsorbent and adsorbate, and should always be positive) [49]. The above equation can be expressed as the "linear BET plot" according to equation (13):

$$\frac{(\frac{P}{P_o})}{n(1-\frac{P}{P_o})} = \frac{1}{n_m C} + \frac{(C-1)}{n_m C}(\frac{P}{P_o}) \quad (13)$$

The terms n_m and C can therefore be calculated by solving for the equations of the equation of the slope of the line ($s = \frac{C-1}{n_m C}$) along with the y-intercept ($i = \frac{1}{n_m C}$). This method however is only applied to a specific range of vapor pressure range of P/P_o = 0.05 – 0.35, therefore adsorption of lower pressures may not accurately represent monolayer coverage due to the filling of micropores. Similarly, at higher pressures may also not be accurate due to capillary condensation [49]. For a quicker screening method which is also less accurate than the one mentioned above, a single point measurement can be done on the condition that the analysis is conducted in the linear region of the BET plot. The following single-point measurement for monolayer coverage is expressed as follow:

$$n_m = n(1 - \frac{P}{P_o}) \quad (14)$$

Through the above equation and by determining the monolayer coverage, the surface area can then be calculated using equation (15):

$$A = n_m N_A \sigma \quad (15)$$

Where N_A is Avogadro's number and σ is the molecular cross-sectional area of the adsorbate molecule (usually N_2 and its corresponding $\sigma = 0.162\ nm^2$).

In a theoretical approach, the isolated sites on the surface of the sample will start to adsorb the inflow of gas at low pressures. Second, as the pressure builds up gradually, monolayer adsorption across the surface area occurs. Third, as the pressure increases further, multilayer adsorption will start causing multilayer coverage where small pores are going to fill first. Here, the BET equation is used to calculate the surface area of the sample. Finally, as pressure increases further, all the surface area of the sample will be covered. The BJH formula can be used to calculate pore size distribution, pore volume, and pore diameter.

The pore size distribution data is based on the NLDFT method which has been the most commonly used in the process of characterizing activated carbons and other porous solids [50]. Even though the derivation of the NLDFT method, which is the updated version of the DFT model, was initially suited for activated carbons; It is also used for ordered porous silica [51]. When it comes to gas adsorption, the first DFT model was created during the 1980's by the work of Seaton et al. [52]. The initial model was then refined into using the non-local density approximation method which started being more implemented by the year 1993 for determining pore size distribution [53]. The NLDFT model is used to determine the density of the adsorbed gas within the pore of a solid under certain conditions, and in practice it is a very complex fitting and regression process that compares theoretical isotherms called "kernels" with experimental isotherms and determines the pore size of the sample. The detailed integral equations of the NLDFT model can be found in detail in [54].

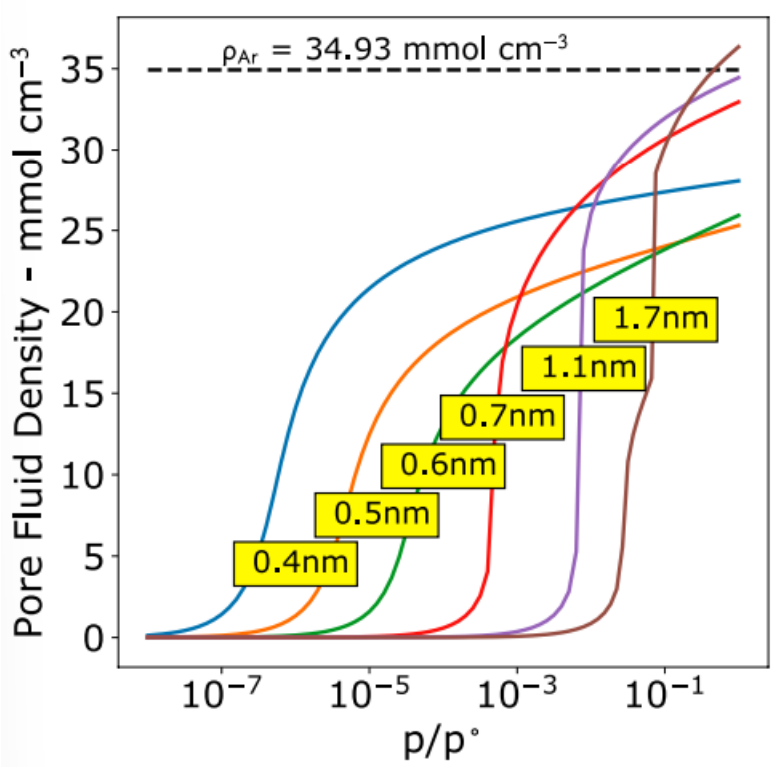

Figure 17. Theoretical Isotherms by NLDFT model for Pore Size Determination [55]

In **figure 17**, it is important to note the difference in pore sizes based on the different fluid density readings which is the main concept behind the NLDFT approach for pore size determination.

2.3.3. Scanning Electron Microscopy

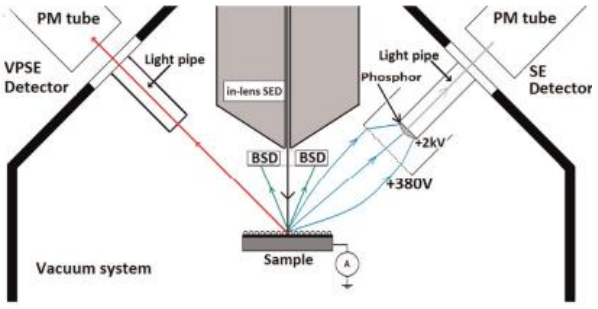

Figure 18. SEM Instrument Schematic [56]

The SEM microscope bombards the sample with charged electrons as described in **figure 18**. The choice of having lower or higher voltage selections is a matter of increased or reduced interaction volume, where having a higher voltage means a higher interaction volume with the sample. Having higher voltages does not necessarily mean a higher resolution, the choice is both sample- and microscope-dependent and therefore should be decided upon case-by-case [57]. Thus, a standard 20 kV voltage was sufficient for all samples examined under the microscope in this study.

SEM is a suitable method to inspect both micro- as well as nano- structures of solid adsorbents. The results and images obtained by the SEM can be combined with other procedures such as XRD mentioned earlier to provide absolute and clear results for crystal composition. An SEM with electron beams that are set in a range set as keV values, allows the production of clear images as **figure 19**, in the micrometer and nanometer ranges with less diffraction effects. The clarity of an SEM image is dependent on several factors which include the type of beam energy along with its corresponding intensity and width, and the proper preparation of sample being examined. Electron beams are deflected on the sample with a certain energy "E" through electromagnetic lenses within the microscope. The most common "E" values of SEM operations can go as low as 2-5 keV, and all the way up to 20-40 keV [58].

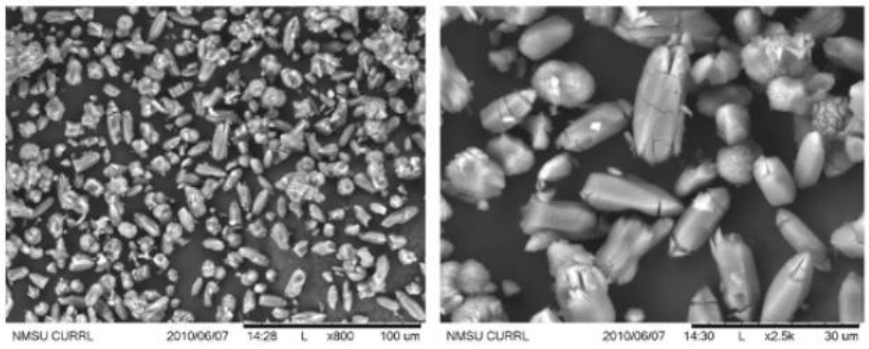

Figure 19. SEM image of Mg based MOF [10]

2.3.4. Thermogravimetric Analysis

Thermogravimetric Analysis is a characterization method consisting of exposing a solid adsorbent to high temperature conditions while measuring the corresponding weight loss of that sample. TGA is essential in determining ash content, volatile matter, and thermal stability of a sample being tested. The amount and type of ash in solid adsorbents comes down to what type of precursor that was used to synthesize the solid adsorbent [59]. TGA consists of exposing the sample to high temperature conditions up to 900^{o}C in a gradual manner while also measuring the sample weight as it is heated. When loss of mass is recorded, it is because of volatile components being flashed off. A TGA analysis was conducted on a biochar sample has shown a significant mass loss in the early stages of heating. Specifically, in the temperature range of 23-134^{o}C, the highest mass loss recorded is due to the moisture retained within the pore structure. As the temperature increases thereafter, the rate of mass loss decreases compared to the first stage of the heating ladder [60].

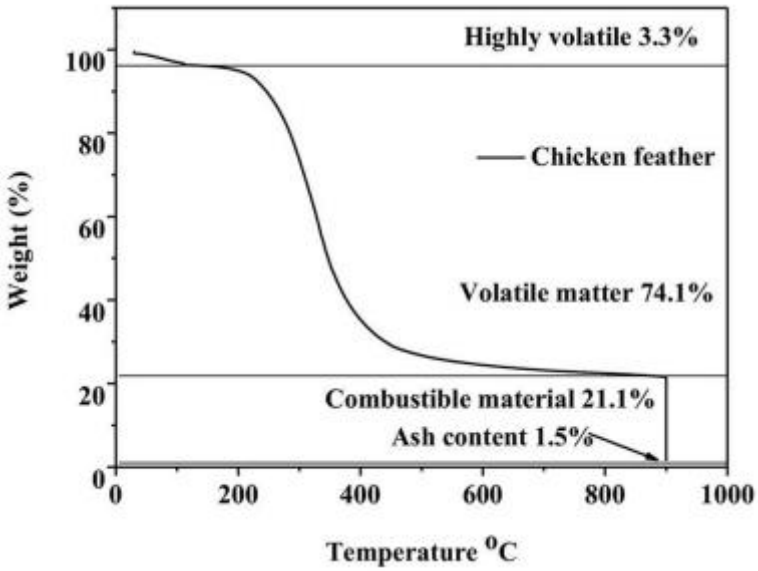

Figure 20. Sample TGA Analysis Chart [59]

Figure 20 above was used as a general example to clearly describe the three stages in a typical TGA analysis weight loss curve of a solid. The first stage being initial moisture or water loss, the second being the decomposition stage, and finally the constant mass remaining would be the total ash content of that sample.

2.4. Pressure Swing Adsorption

PSA units are typically used as a method of purifying gas streams in steam reforming processes. The concept of a PSA is using polybeds of solid adsorbents in a cyclic manner to purify any impurities in the stream. The process operates at a constant temperature, allowing it to achieve a cycle within a few minutes which makes it a highly effective and economical method for gas separation. The binding of impurities such as carbon dioxide, carbon monoxide, nitrogen, water vapor, and other carbon derivatives is a physical phenomenon. The increased use of PSA systems in the industry is linked to its flexible capability, and energy efficiency [61]. This flexibility is also owed to the wide range of microporous solid adsorbents which include AC, zeolites, silica gels, and polymeric adsorbents [12].

2.4.1. PSA Cycle Process

Operational steps are unique to every PSA process depending on its design, where some designs have several beds as shown in **figure 21**. However, the cycle process is based on several general steps which includes pressurization, adsorption, depressurization, and purging.

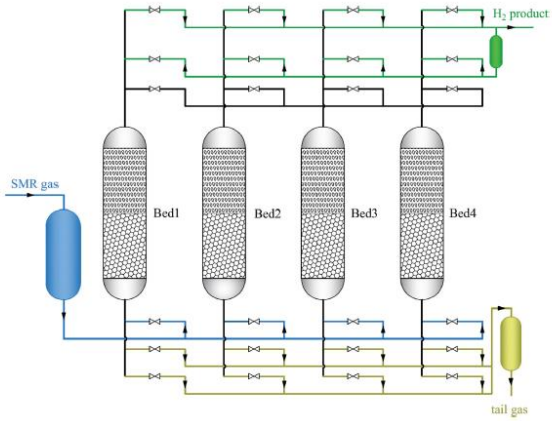

Figure 21. 4-Bed PSA System Schematic [62]

The feed gas composition used in the study for the system described in **figure 21** is: Hydrogen (76%), carbon dioxide (20%), methane (3.5%) and carbon monoxide (0.5%). A typical PSA process consists of the following steps:

- **Pressurization** is done by introducing the feed gas through the bottom-side as shown in **figure 21** above.
- **Adsorption** takes place as the impurities adsorb on the selected adsorbent layers selected for this process, in this case Zeolite and Activated Carbon. Highly pure hydrogen passes through the topside of the bed as the product, and impurities (CO_2, CH_4, CO) remain in the bed.
- **Depressurization Equalization** is done to relieve the pressure gradually from a high-pressure bed to a low-pressure one until equilibrium pressure is reached. This step can be divided into several pressure equalization steps to achieve higher hydrogen recovery results. This can be seen through steps II and V in the illustration in **figure 22**.
- The **Blowdown/Depressurization** step which is basically further decreasing the pressure inside the bed until an atmospheric pressure is achieved to allow for the purging of impurities.
- The **Purge** step is done by having a counter-current hydrogen flow in the bed to push the impurities from the adsorbents towards the purge stream. It is important to note that this does affects hydrogen recovery since a fraction of the pure hydrogen product is being used to flush the impurities [62].

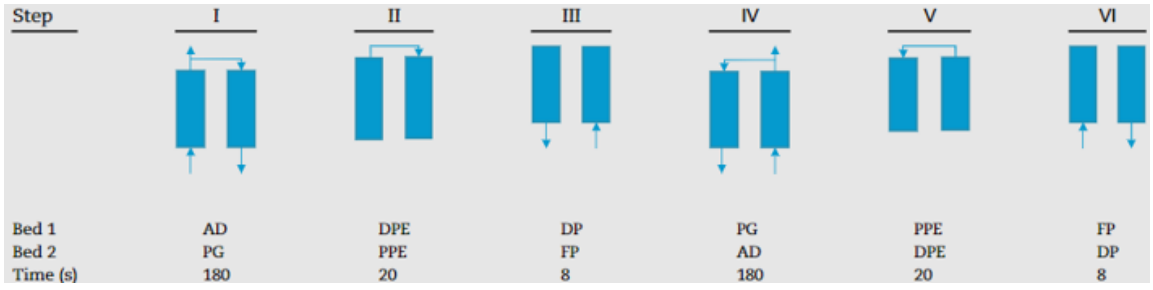

Figure 22. Dual PSA Cycle Sequence Diagram [63]

2.4.2. Commercial Solid Adsorbent Performance in PSA Systems

The solid adsorbents that will be tested in this thesis could be used in several gas separation systems including PSA. In addition, it is also important to review the research done in the literature on the same or similar structures of the solid adsorbents for comparison. The adsorbents that have been mostly linked to PSA systems for the separation of gases such as carbon dioxide, methane, and carbon monoxide have been AC as well as different forms of zeolites (3A,4A,5A, and 13X).

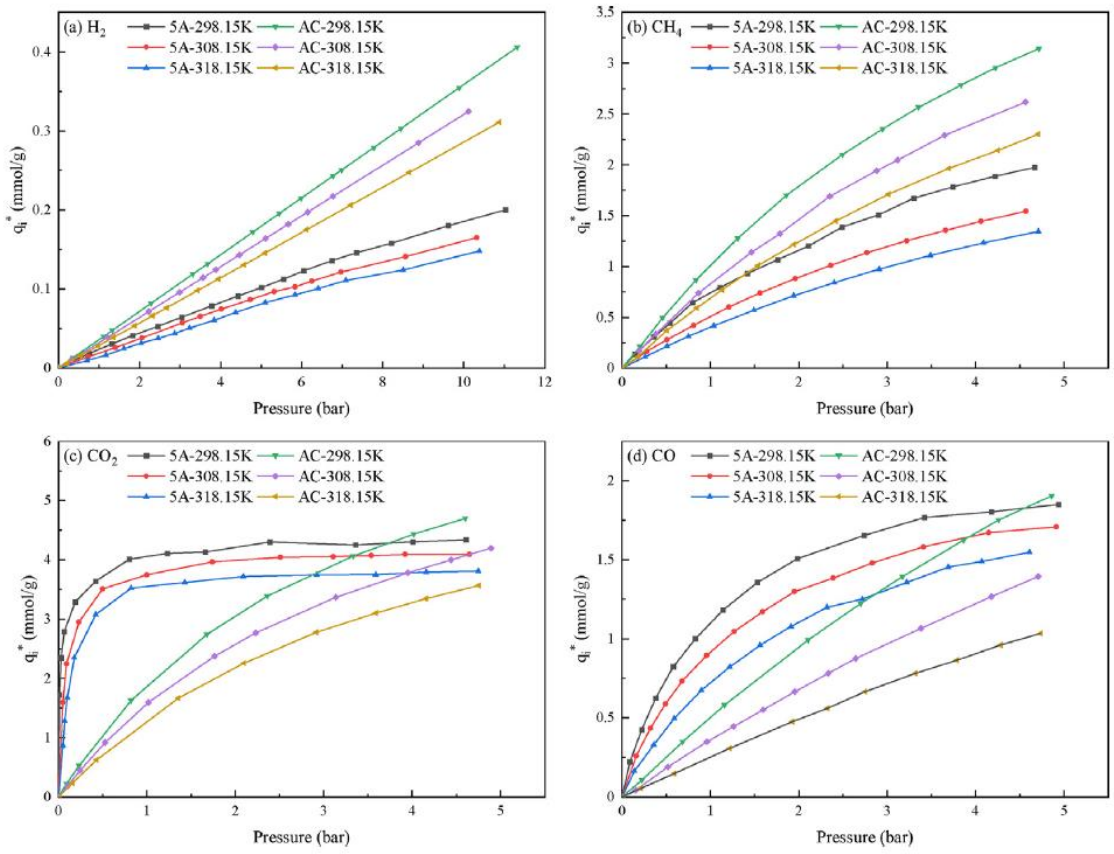

Figure 23. Comparative Adsorption Capacities of AC and 5A Zeolite on (a) H_2, (b) CH_4, (C) CO_2, and (d) CO [62]

Figure 23-a shows the adsorption capacity of hydrogen at different pressures. It is clear from the graph that hydrogen is very difficult to adsorb due to its volatile nature, and due to the low selectivity that AC and zeolite 5A have for hydrogen. In **figure 23-b** which is illustrating the adsorption capacity of methane. What can be seen is that Activated Carbon has a higher Adsorption Capacity than 5A Zeolite when it comes to methane adsorption. **Figure 23-c** shows the adsorption capacity of carbon dioxide where 5A Zeolite strongly adsorbs CO_2. This can be seen by the sharp increase on the isotherm which makes it very difficult to desorb/regenerate CO_2 from zeolite 5A. However, Activated Carbon can reach similar adsorption capacities for CO_2 when compared to zeolite 5A at certain pressures (in this case at 3.8 bars). The isotherm is clearly smooth compared to that of zeolite 5A which makes CO_2 much easier to desorb/regenerate. Finally figure 17 (d) displays the adsorption capacity of carbon monoxide. What can be observed in **figure 23-d** is that zeolite 5A has a higher Adsorption Capacity than Activated Carbon at partial pressures below 4.5 bars. It is important to note that the bottom layer of the beds in a typical PSA unit which is normally near the feed stream, is usually an Activated Carbon bed. The aim for this is that activated carbon is very

effective in removing impurities such as Carbon Dioxide (preventing it from reaching zeolite 5A to avoid regeneration difficulties) as well as methane. For further confirmation on the adsorption behavior of CO_2 on different solid adsorbents, the following experiments were conducted on Zeolite 13X, Zeolite 4A, and AC at low pressure and different temperatures shown below in **figures 24-25**.

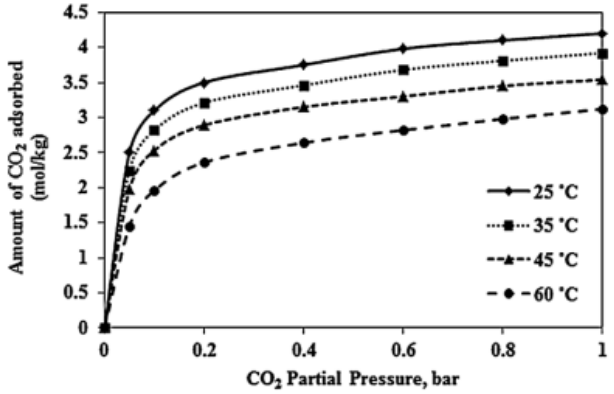

Figure 24. Low Pressure Adsorption Isotherm of CO_2 on Zeolite 13X [64]

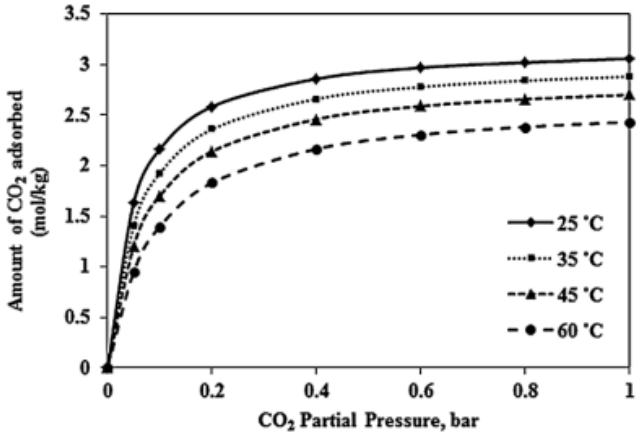

Figure 25. Low Pressure Adsorption Isotherm of CO_2 on Zeolite 4A [64]

As seen in **figures 24-25**, both adsorption isotherms follow a very similar trend when it comes to CO_2 adsorption on zeolites. The trend is also as that in **figure 23-c** in which CO_2 strongly and quickly adsorbs on the zeolite micropores. This specific test was run for 5 consecutive cycles to study the feasibility in regenerating zeolites after adsorbing CO_2. After every cycle, the results have shown a reduction in the amount of gas adsorbed after every cycle which clearly indicates that the adsorption process of CO_2 on zeolites is not completely reversible [64]. In other words, the desorption of CO_2 from zeolites can be obtained, however full regeneration cannot be obtained after several repeated cycles.

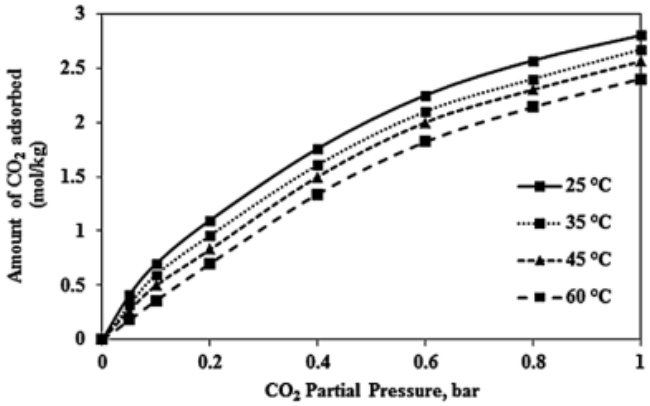

Figure 26. Low Pressure Adsorption Isotherm of CO_2 on AC [64]

Similarly, **figure 26** represents the same adsorption trend as that of **figure 23-c** for CO_2 on AC. The carbon dioxide gas is gradually adsorbed onto the AC micropores. This also means that regeneration of AC will be much easier and linear compared to zeolites. The results also show a lower adsorption capacity of CO_2 on AC compared to zeolites at low pressure. However, at higher pressures (up to 35 bars) the adsorption on AC is much higher than that of Zeolites [64].

3. Experimental Part

In this section the objective is to describe and present the relevant samples as well as the instruments used in this study. Each instrument used in the experiments will be mentioned and described, and the relevant data will be analyzed and discussed in the following sections.

3.1. Materials

The adsorbents being tested in this study are SAC22-029, SAC21-050, and SAC21-037 which are activated carbon samples synthesized by *Beyonder* which is a battery company operating in Stavanger-Norway. The samples will be characterized and compared to a commercially available activated carbon denoted by the sample YEC8B as well as a commercial zeolite 13X sample. There is no prior information on how the activated carbon samples were synthesized due to company privacy.

3.2. Characterization Methods:

A series of instruments have been used throughout the study for characterization of the samples mentioned.

3.2.1. SEM

The microscope used for getting the SEM images is the Zeiss Supra-35VP microscope located in the labs of UiS. The microscope is connected to nitrogen gas tanks in an adjacent room to provide a continuous and adequate flow of Nitrogen during sample inspections. Samples were prepared from the solid adsorbents to have a closer look at the pore structures of each ACs and zeolites. First, small pieces of double-sided tape were cut to fit the size of the sample holder which goes directly under the microscope. Once the outer surface of the tape is covered with the sample, excess powder is tapped off and the sample holder is placed inside the chamber. Once the samples are secured in place, the chamber is vacuumed, and the position of the microscope can then be chosen depending on which sample we're looking at first.

The microscope used is shown in **figure 27** where it is also connected to a computer and a control panel. The control panel along with the SEM software allows different display adjustments including brightness, contrast, zoom level, focus, aperture, and wobble stabilization. In addition, a voltage must be chosen where the typical voltage range for SEM microscopes is 15-20 kV [57].

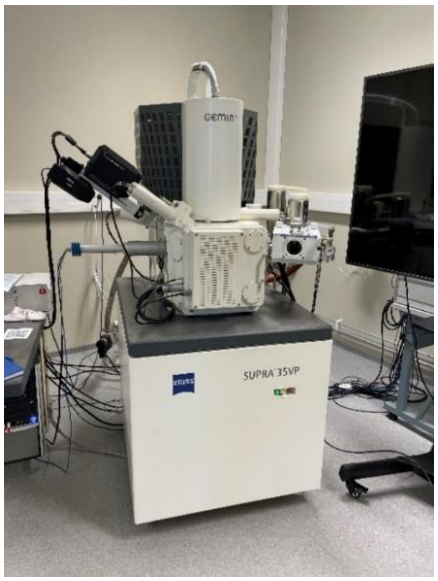

Figure 27. Zeiss Supra-35VP SEM used in the study (UiS)

3.2.2. TGA

The Mettler Toledo TGA/DSC 3+ shown in **figure 28** was used in this study as part of the characterization of the samples being examined. This thermogravimetric analyzer is a device that is well known for its use in characterizing different solids through mass and heat flux measurements as a function of time [65]. This device has a horizontally designed sealed oven which allows a smooth flow of method gas. The design also allows no disturbance to the measurements regardless of the gas used. The method temperature used for all test runs of the Thermogravimetric analysis is based on the literature standard of having a maximum temperature of 900^{o}C.

Figure 28. TGA Instrument at UiS

The TGA/DSC instrument is connected to the STAR© software on a separate computer where the method parameters can be set as shown in the table below. All the samples were tested in sample holders called ceramic crucibles which are made of Al_2O_3. An empty crucible is first set into the furnace where a built-in weight balance measures the weight of the crucible and then zeroed for reference. After all test parameters are set and the weight calibrated, the empty crucible is removed and is then half-filled with the sample. Next, the crucible is set in its designated position and once the required start temperature is reached within the furnace, the seal is then closed, and the measurement begins. The temperature is set to start at 25°C, increasing at a rate of 10 K/min, and ends at 900°C as is the standard testing for activated carbons in most of the literature. The weight is measured versus the temperature to evaluate the weight loss as a function of temperature. The method used is summarized in **Table 2**.

Method Gas	Air
Start Temperature [°C]	25
End Temperature [°C]	900
Air Flow Rate [ml/min]	25
Heating Rate [K/min]	10

Table 2. TGA Experimental method parameters

3.2.3. Nitrogen Physisorption

Sample characterization is continued with the use of the Tristar II 3020 – BET instrument that uses nitrogen physisorption to determine the surface area and pore size distribution of the samples. The samples are weighed-in and placed in a glass tube which are used for both degassing and adsorption measurement inside the instrument. The activated carbon samples used for the nitrogen physisorption characterization measurements have been degassed for 22 hours at 200°C for pre-treating and removing moisture. The zeolite 13X was degassed at a higher temperature 250°C for the same time to flash out any moisture adsorbed when preparing the samples due to its hydrophilic nature as compared to activated carbons. The pre-treatment conditions, sample weights, and the corresponding weight loss is recorded and summarized in Table 3 below.

Sample	Degassing Time [hours]	Degassing T [°C]	Weight Before [g]	Weight After [g]	Weight Loss [%]
SAC21-050	22	200	0.0872	0.0845	3.096
SAC22-029	22	200	0.0745	0.0728	2.282
SAC21-037	22	200	0.0809	0.0705	12.855
YEC8B	22	200	0.0967	0.0930	3.826
Zeolite 13X	22	250	0.3791	0.3747	1.161

Table 3. BET Experimental sample parameters used in measurement results

After degassing, the glass tubes are transferred from the degasser to the adsorption instrument where it has 3 designated ports for simultaneous measurements. After insertion, liquid nitrogen is filled in a container placed under where the tubes where they will be fully submerged. Liquid nitrogen has a temperature of 77K which will provide the nitrogen gas with ideal conditions for adsorption.

3.2.4. Low Pressure Adsorption Analysis

The BELSORP MAX II used in the study is shown in **figure 29** and is a very flexible instrument that can conduct measurements for gas adsorption (at both LP and HP), chemisorption, surface area and pore size distribution. The preparation of samples is slightly different depending on whether the measurements are done at LP or HP. For low pressure, up to two samples can be tested at once where the samples are placed in glass sample holders. For LP adsorption which was done for all the samples in this study, a glass sample holder is used at pressures up to 1 bar. The instrument is also capable of handling various types of gases at different temperature and pressure conditions.

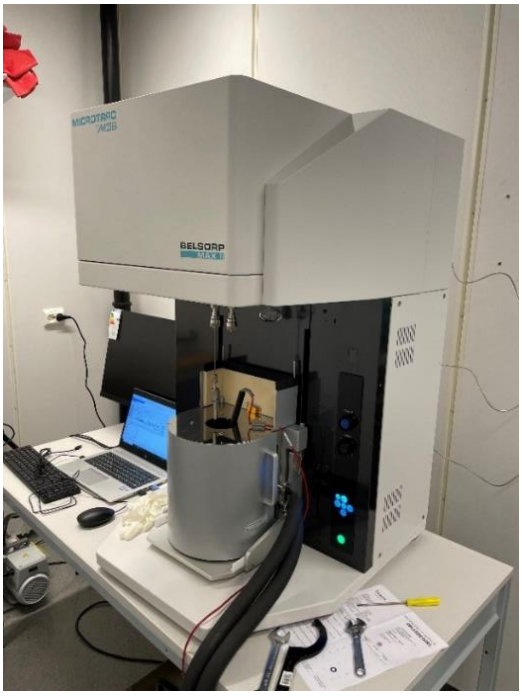

Figure 29. BELSORP MAX II Instrument used in the adsorption analysis (at UiS)

Degassing of the samples can be done in one of two ways. The first way is done within the instrument itself where a 4-port detachable furnace can be attached after installing the HP sample in port #2 (the only port on the instrument that is specific for high pressure analysis). The heater and controller used in the instrument's degassing process are shown in **figure 30**.

Figure 30. BELSORP MAX II heater and controller used for degassing [66]

The second way of degassing the samples is using the BELPREP degassing unit which is done externally which is also shown in **figure 31** below.

Figure 31. BELPREP external degassing unit (at UiS)

All the instrument's capabilities are accomplished accurately because of electropolished manifolds and lines which prevents corrosion and wetting. In addition, the valves used in the BELSORP MAX II are pneumatic which minimizes errors and leaks when under high vacuum conditions [66].

4. Results and Discussion

In this section the results will be discussed based on the method of analysis chosen for this thesis. Due to a heavy load of students who are working with adsorption projects and the limited time for acquiring results, the following results will be discussed:

- Characterization analysis of all samples
- LP Adsorption
- Fitting Data
- CO_2/N_2 Selectivity using IAST method
- Heat of Adsorption analysis of all samples
- Conclusion

4.1. Characterization Results

4.1.1. SEM

The pore structure of AC is usually formed from the evaporation and break-down of non-carbon materials used in the preparation of the AC. In addition, AC usually have a rough and irregular surface when compared to zeolite structures [67]. The roughness and sharp edges of a sample are most likely due to the method of activation and activation intensity of the carbon sample. The higher the activation intensity, the sharper the edges on the surface of the sample. It is important to note that the carbon samples denoted with the name "SAC" are the same base sample, but each was subjected to different activation intensities hence the different choice of numbering.

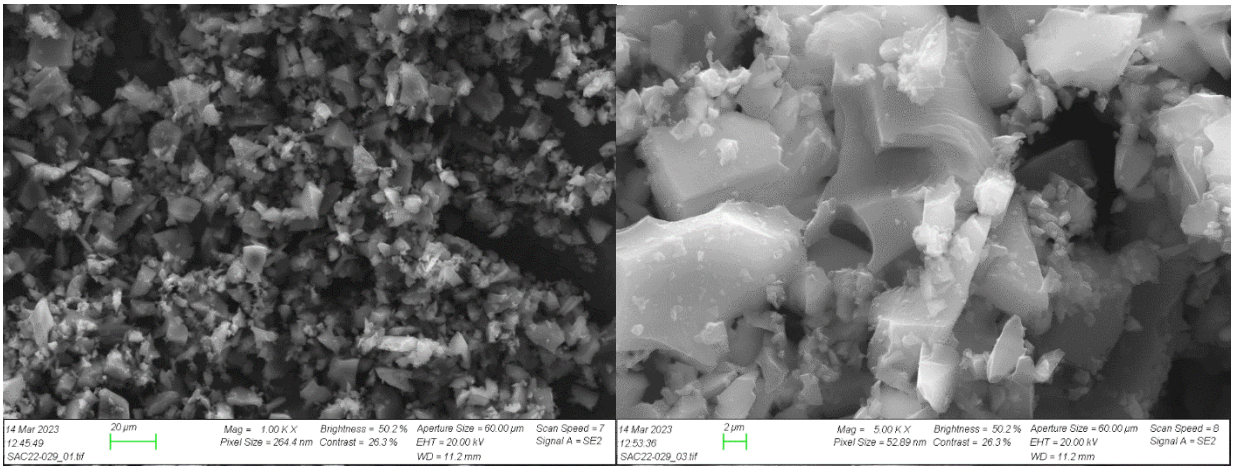

Figure 32. SEM Image of SAC22-029 (left: 1000X Mag, right: 5000X Mag)

The SAC22-029 sample has the lowest surface area among the carbon samples which is related to having a low intensity during activation. The left SEM image in **figure 32** shows a few clusters which aren't as clear as the image on the right. These bulky structures are consistent with the cellulose structure that makes up wood. The sample is clearly made from raw materials that contains wood or saw dust.

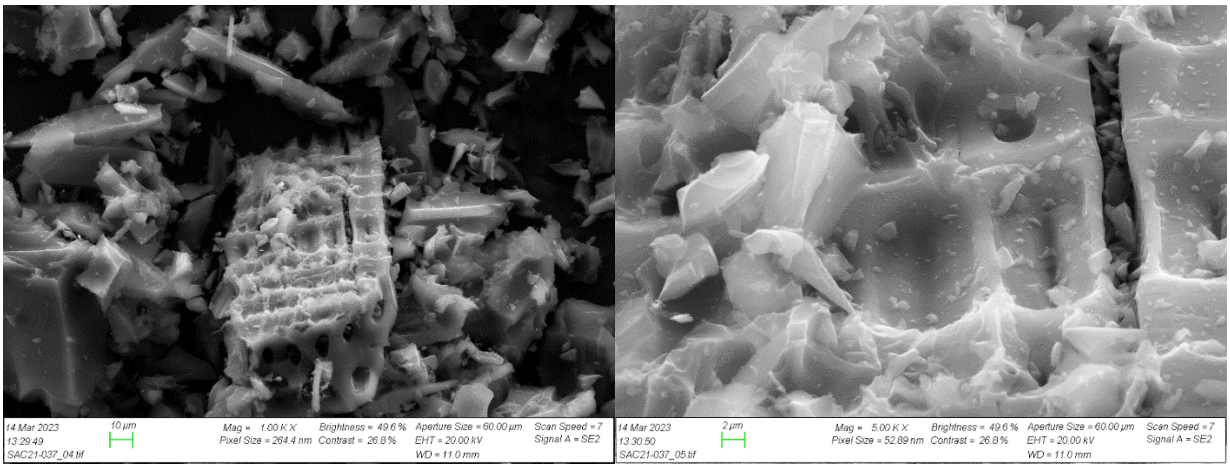

Figure 33. SEM Image of SAC21-037 (left: 1000X Mag, right: 5000X Mag)

The SAC21-037 is shown in the SEM image in **figure 33** where the image on the left clearly shows the cellulose structure clearly as I have mentioned earlier. In addition, the image on the right is consistent with a high activation intensity due to the rough and sharp surface of the sample. In general, the sample seems to show smaller structures than the previous sample however in some areas still has visible bulky structures.

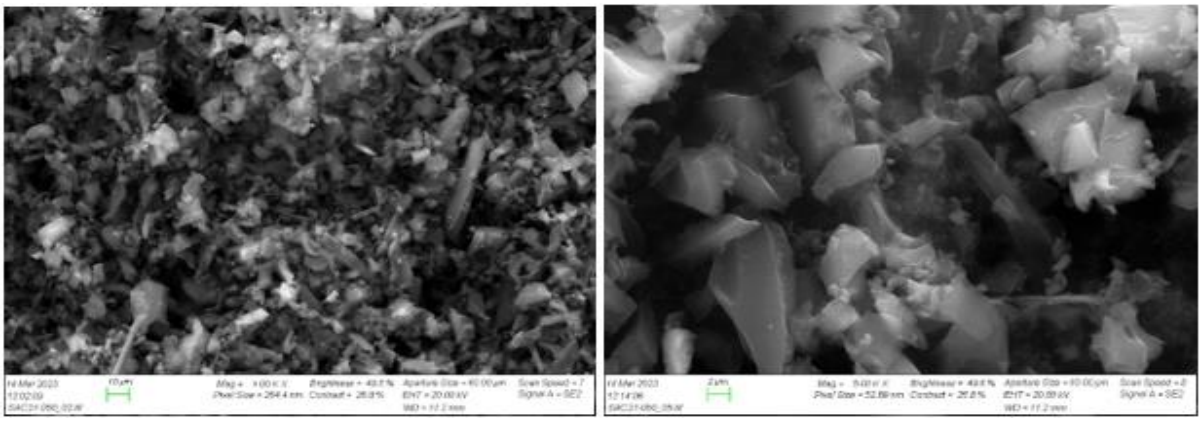

Figure 34. SEM Image of SAC21-050 (left: 1000X Mag, right: 5000X Mag)

The SAC21-050 was subjected to the highest activation intensity thus explaining the increase in its surface area. Both images in **figure 34** show a more uniform and smaller structures like that of YEC8B which is the commercial sample.

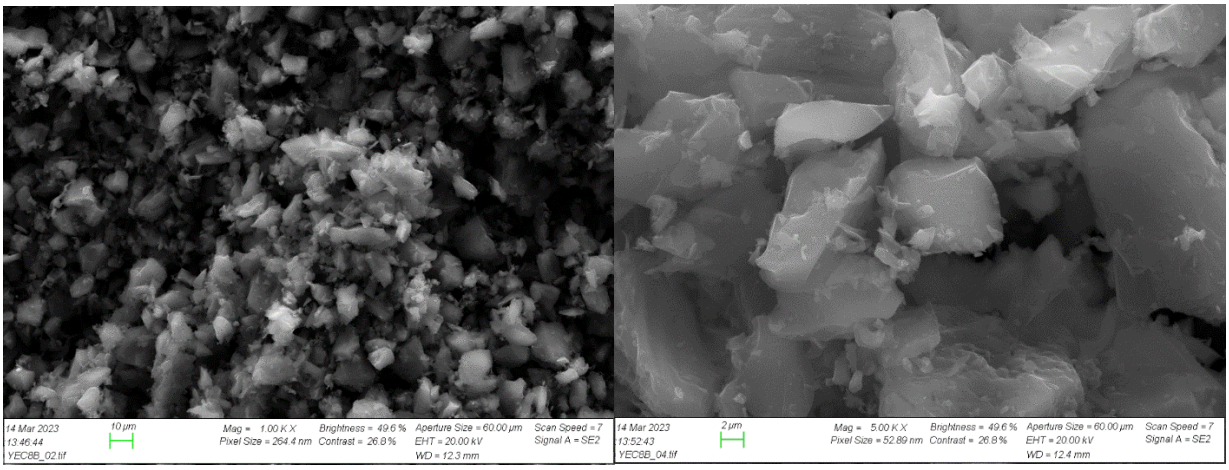

Figure 35. SEM Image of YEC8B (left: 1000X Mag, right: 5000X Mag)

The following carbon sample shown in **figure 35** is a commercially available AC that shows no visible bulky structures compared to the activated carbon samples from *Beyonder* denoted by "SAC". The sample seemingly shows a small and uniform structure which most likely suggests this sample contains more micropores than mesopores.

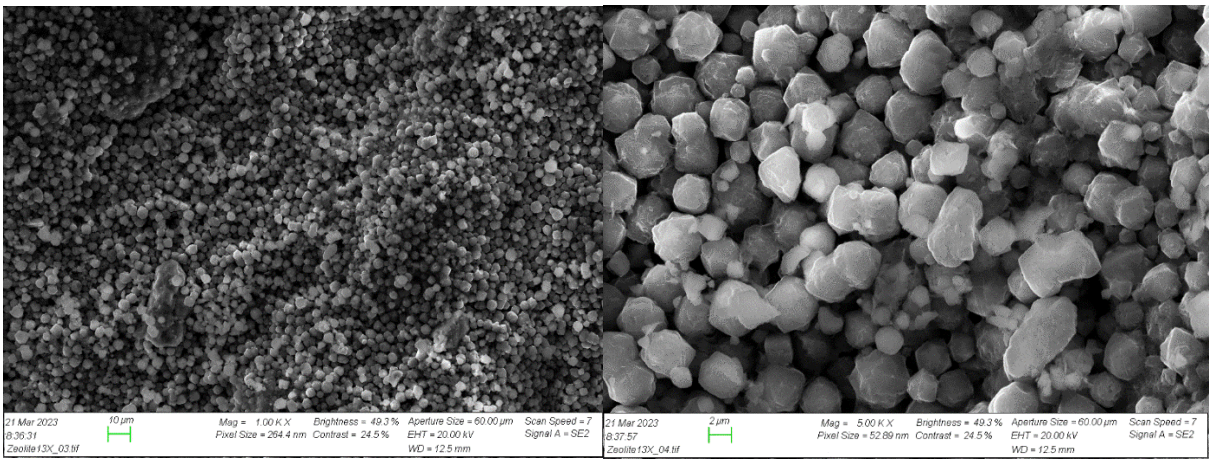

Figure 36. SEM Image of Zeolite 13X (left: 1000X Mag, right: 5000X Mag)

Zeolite 13X shown in **figure 36** is more spherical and uniform in structure where the average particle diameter is 4 micrometers as seen in the SEM image on the right (view scale). Silicone, aluminum and oxygen atoms are the building blocks of zeolite 13X. Each (Si) and (Al) atom is linked to four oxygen atoms resulting in (SiO_4) and (AlO_4) called a tetrahedral configuration. In addition, each oxygen atom is shared between different tetrahedral structures resulting in a uniform distribution of pore sizes [68]. **Figure 36** clearly shows the uniformity and consistency of pore size in the zeolite 13X sample in relation to its chemical structure.

4.1.2. Nitrogen Physisorption

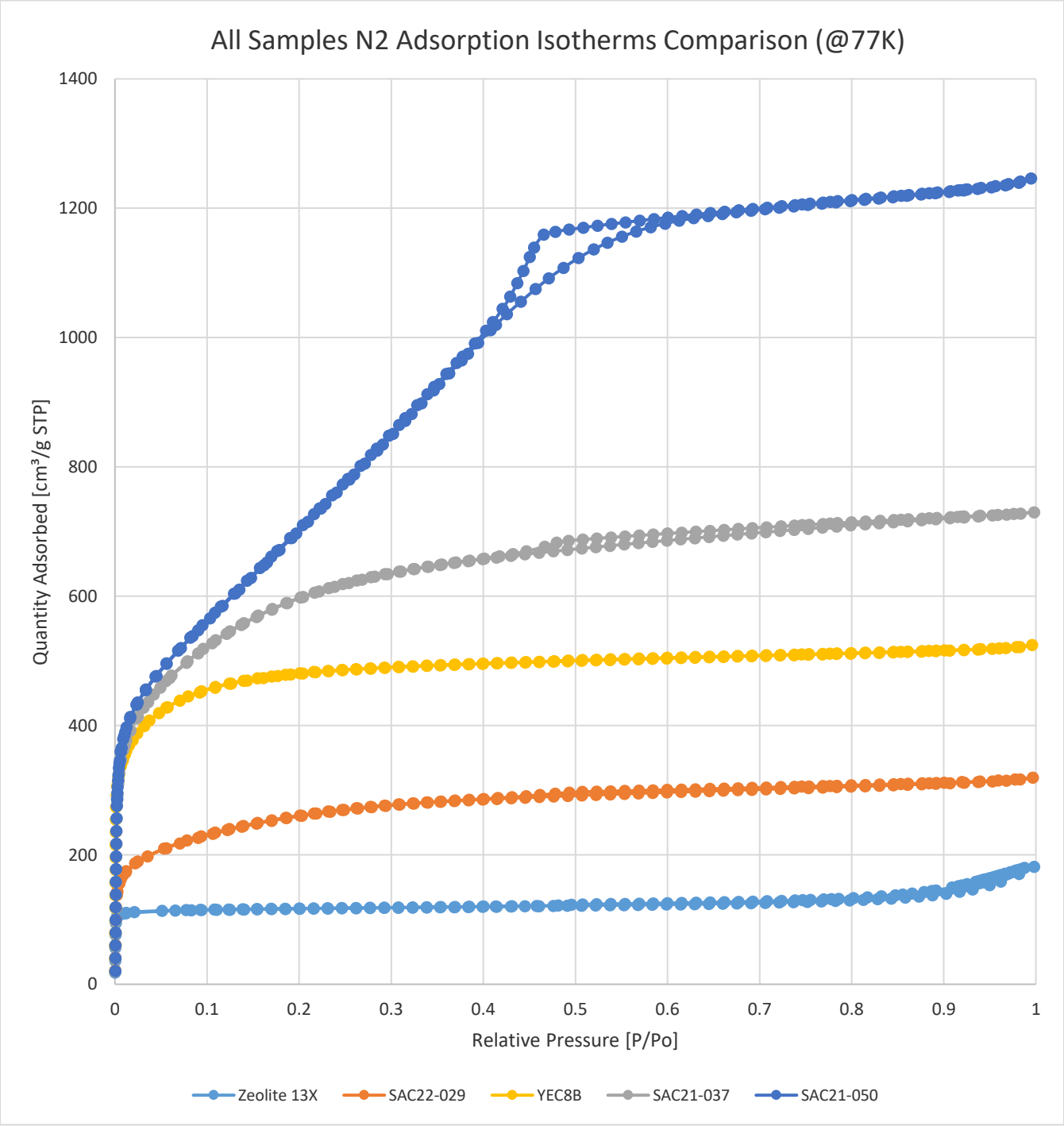

Figure 37. All Samples LP N2 Isotherm Comparison

The above N_2 adsorption isotherms illustrated in **figure 37** of the activated carbon samples and the zeolite sample can be directly correlated with their surface areas. The lowest adsorption capacity among the carbon samples which is SAC22-029, corresponds to it having the lowest surface area with no clear hysteresis loop. As the surface area of the samples increase, the nitrogen adsorption capacity increases

and the hysteresis loops become more prominent while also changing in shape (which corresponds to knowing that the pore structures are also changing). The hysteresis loop for SAC21-050 fits the type H2 hysteresis loop mentioned in **figure 7** previously which suggests that the pore type is a "ink-bottle" pore structure with a wide body. The hysteresis loop for SAC22-029 corresponds to type H4 which suggests that the pore structure is "narrow slit-shaped" pores. The hysteresis loop for SAC21-037 corresponds to type H3 which suggests that the pore structure is "slit-like". The YEC8B sample shows a barely visible hysteresis loop which means the sample is very microporous and shows very little mesoporosity thus making it difficult to determine the micropore structure of this sample from its hysteresis loop. The zeolite 13X hysteresis loop corresponds to type H4 which also suggests "narrow slit-shaped" micropores. The corresponding determination of the BET surface area from nitrogen physisorption are summarized in **Table 4** below.

Sample	Type	BET Surface Area [m^2/g]
SAC22-029	AC (Beyonder)	931.2095
SAC21-050	AC (Beyonder)	2613.0189
SAC21-037	AC (Beyonder)	2157.8749
YEC8B	AC (Commercial)	1672.4192
Zeolite 13X	Zeolite (Commercial)	395.4560

Table 4. Experimental BET Surface Area data results

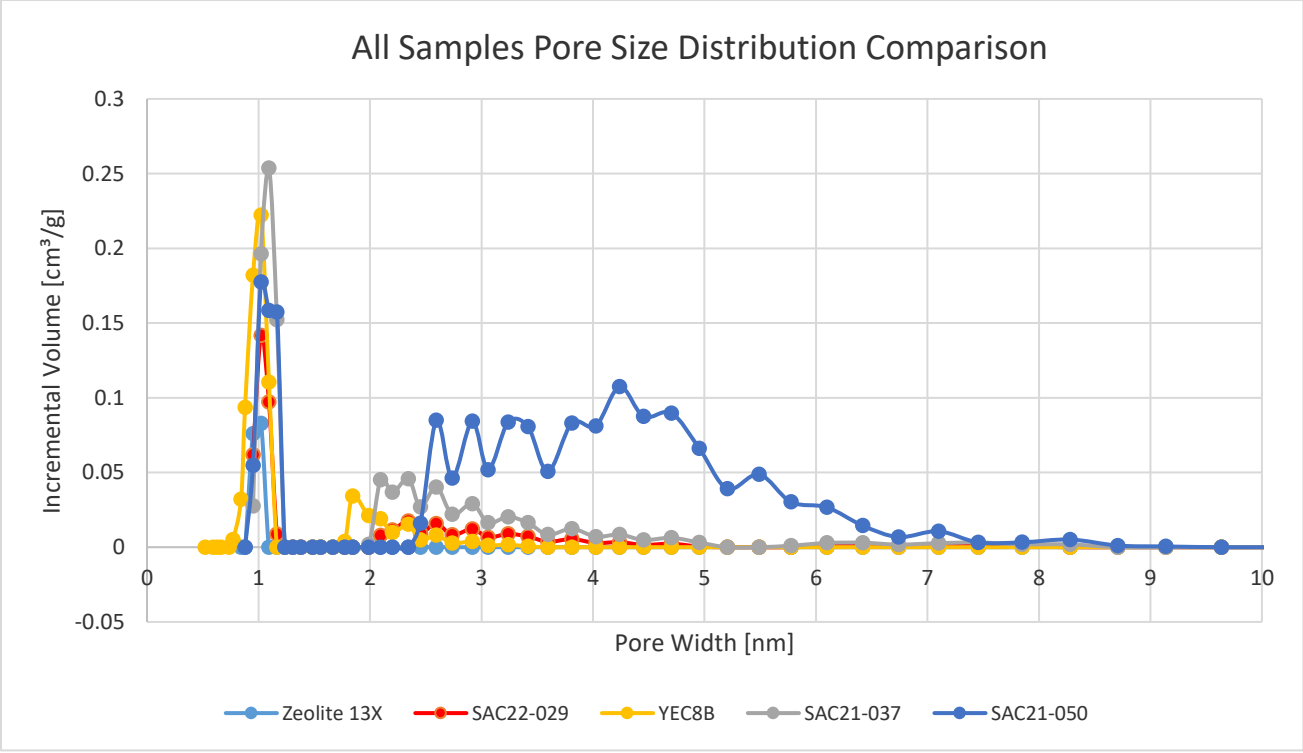

Figure 38. NLDFT All Samples Pore Size Distribution Comparison

In addition to measuring the BET surface area from nitrogen physisorption, the pore size distribution is also measured. The pore size distribution shown in **figure 38** above shows the pore size distribution of all the samples in increasing order of surface area where zeolite is the least and SAC21-050 is the largest. The

graph reveals the mesopore volume in all the samples which corresponds with the visibility of the hysteresis loop mentioned earlier.

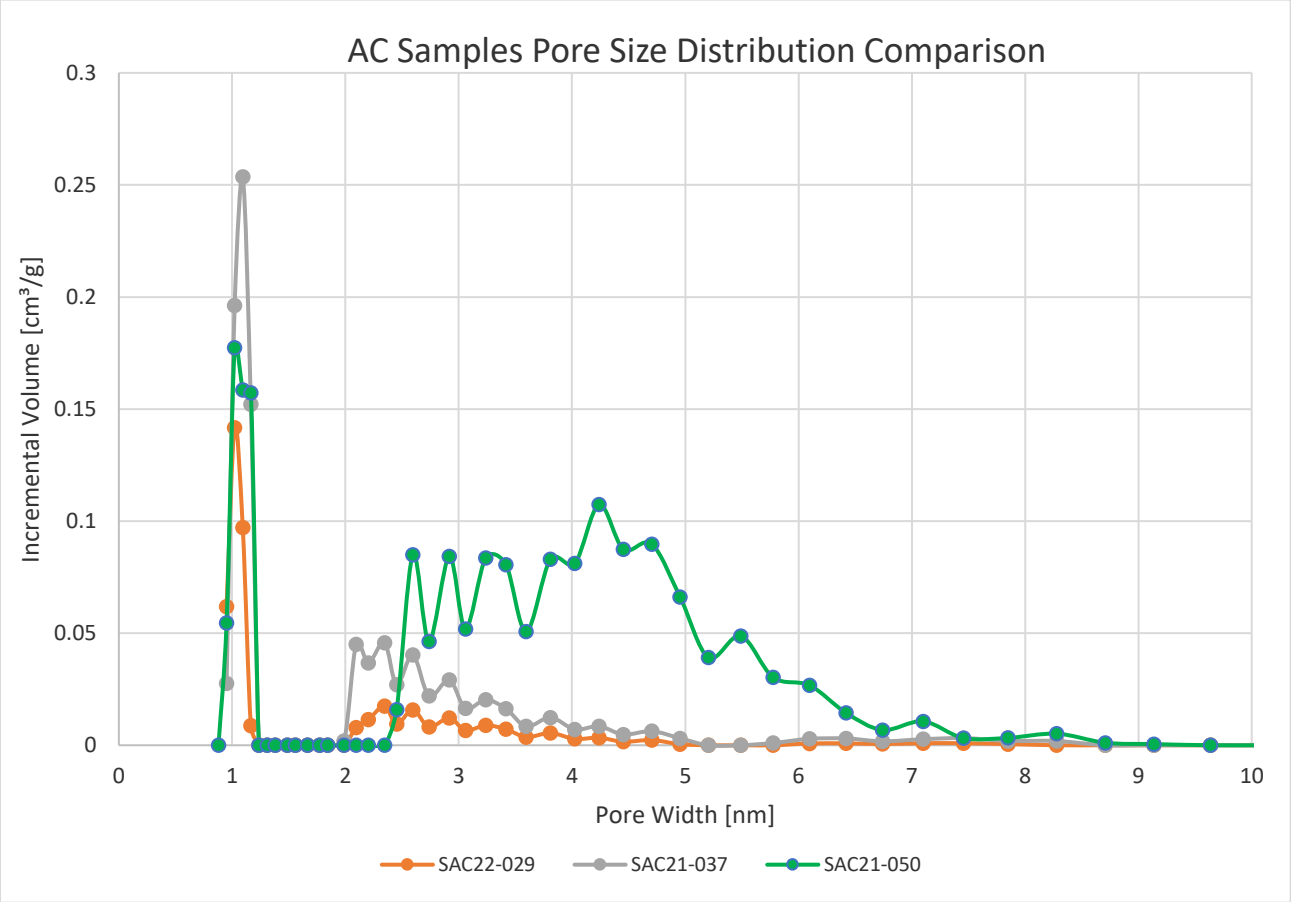

Figure 39. SAC Carbon Samples Comparison (Activation Intensity)

The SAC22-029 → SAC21-037 → SAC21-050 are the same sample but at increasing activation stages (higher activation intensity from left to right). As shown in **figure 39**, the micropore volume of the lowest surface area carbon sample SAC22-029 is at its peak at 0.14 cm^3/g with a peak of mesopore volume of 0.02 cm^3/g. After increasing the activation intensity of sample SAC22-029, the sample is then referred to as SAC21-037 where the higher intensity resulted in the increase in micropores to reach the highest peak of 0.26 cm^3/g while also showing an increase to a maximum mesopore volume to 0.05 cm^3/g. The increase in micropore and mesopore volume resulted in the increase in surface area of the sample from 931.21 m^2/g to 2157.87 m^2/g. After further increasing the activation intensity of the base sample which is referred to as SAC21-050, the peak micropore volume decreases from 0.26 cm^3/g to 0.17 cm^3/g while showing a significant increase in maximum mesopore volume from 0.05 cm^3/g to around 0.11 cm^3/g. This is seen from the three samples where the highest surface area does not have the highest micropore volume. This is due to the collapse of micropores into mesopores at increased activation intensity thus suggesting that there is a plateau between increasing activation intensity of a sample and micropore generation.

4.1.2.1. Samples Chosen for Adsorption Measurements

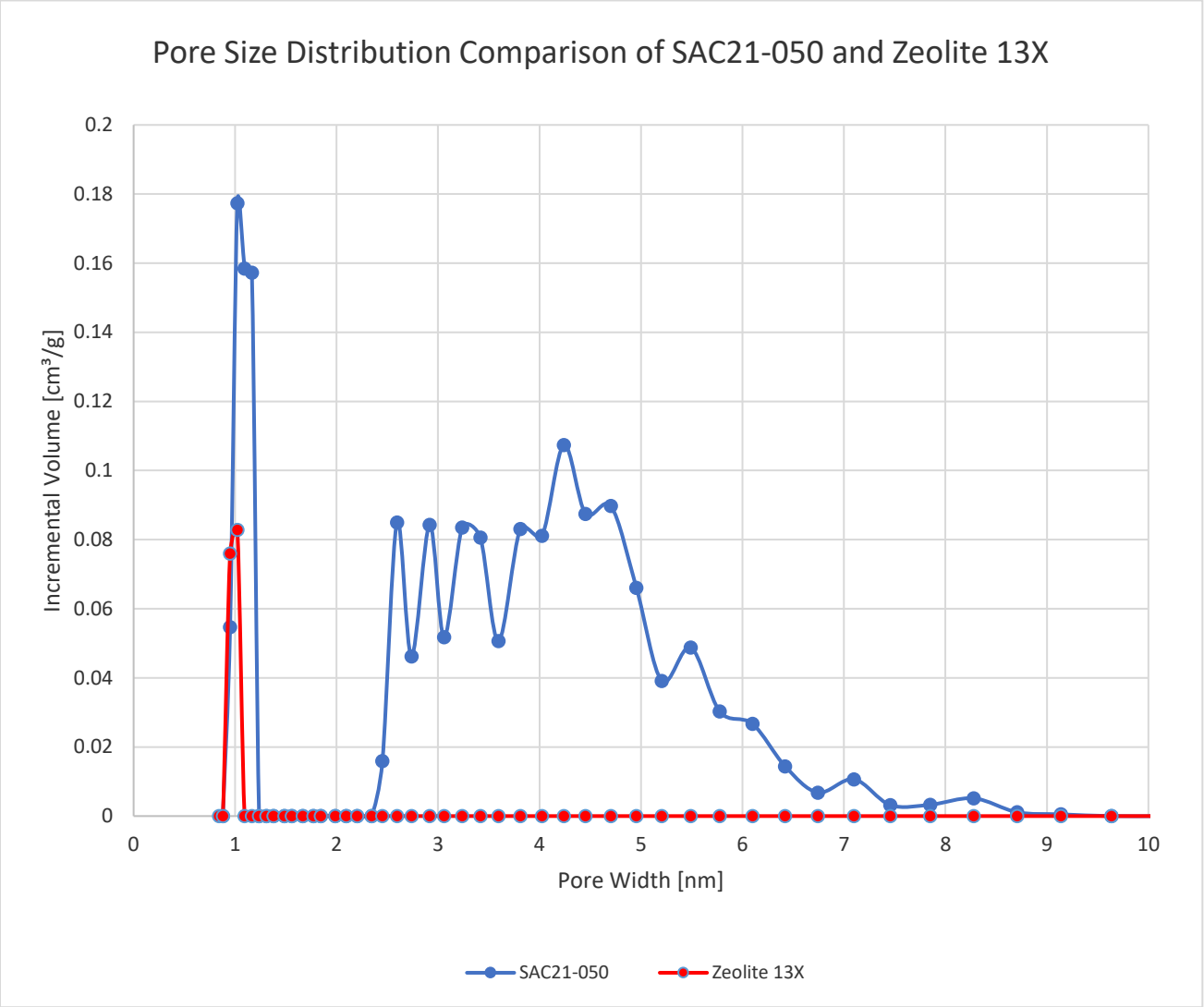

Figure 40. Pore Size Distribution AC and Zeolite 13X

Due to the limited access to the adsorption instrument, the highest surface area carbon sample (SAC21-050) as well as the zeolite 13X sample was chosen for low pressure adsorption measurements on Nitrogen and Carbon Dioxide. The pore size distribution of SAC21-050 is compared with that of the Zeolite 13X sample in **figure 40** and the AC sample shows to have the highest amount of micropores and mesopores compared to the zeolite 13X sample. From the pore size distribution data of these two samples alone, the SAC21-050 sample could suggest having a higher adsorption capacity for both N_2 and CO_2 due to larger pore size distributions which can accommodate both the sizes of N_2 molecules (0.364 nm) and CO_2 molecules (0.33 nm). However, pore size distribution alone cannot determine whether a certain sample will have a better adsorption performance.

4.1.3. Thermogravimetric Analysis

In addition to determining the surface area and pore size distribution of the samples in the previous sections, TGA analysis is as important in determining the thermal stability of the samples tested as well as determining ash content of the samples. TGA analysis with weight loss is consistent in the literature to have three main stages. The first stage is the removal of water, the second is degradation of the carbonaceous components of the sample, and the third is the ash residue (if any).

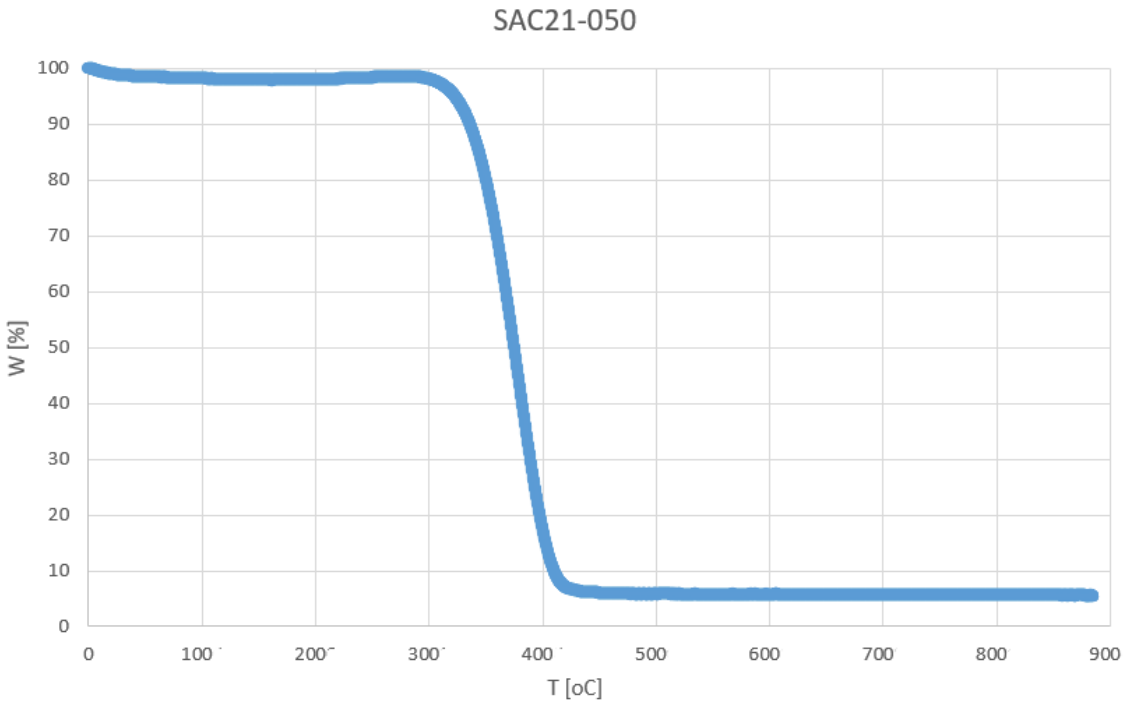

Figure 41. Weight Loss % of SAC21-050

In **figure 41**, the SAC21-050 sample has recorded a 2% initial weight loss in the temperature range of 0-150°C which is related to the removal of water adsorbed within the pores. The sample starts to degrade at around 320°C until it reaches 400°C where the weight loss reaches its maximum at 93% weight loss in that temperature range. In this range the weight loss is due to the decomposition of the carbon material in the sample [69]. The remaining weight recorded up to 900°C with no further weight loss representing a fixed weight is the ash content present in the sample which is at around 5%.

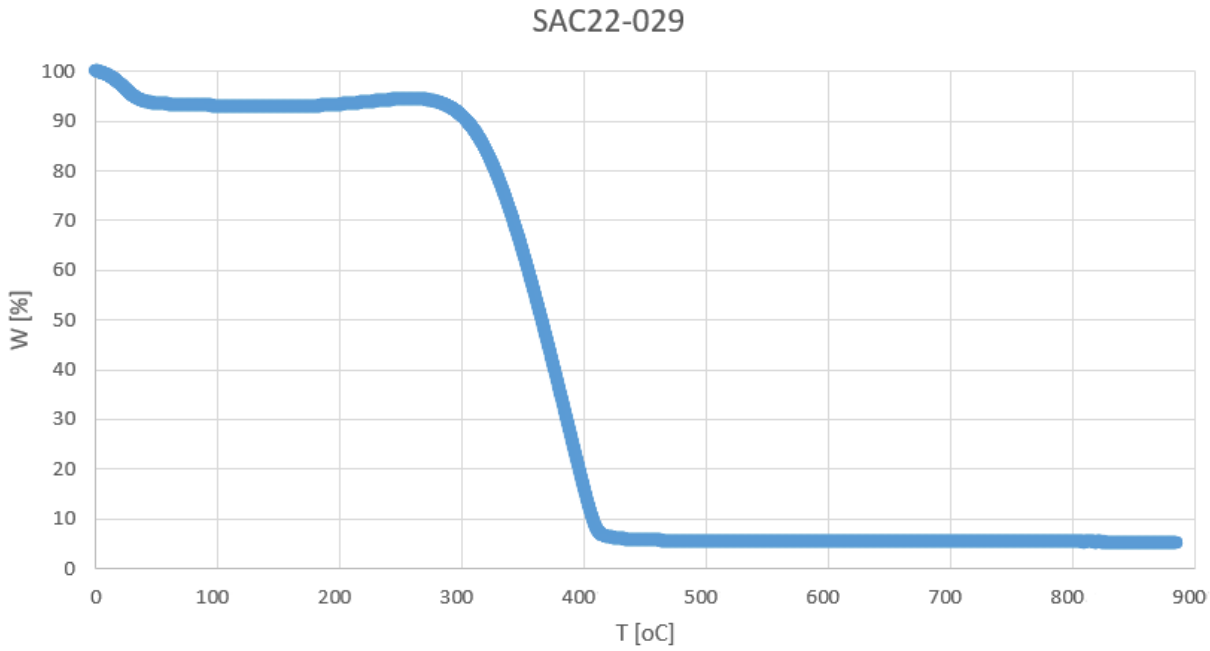

Figure 42. Weight Loss % of SAC22-029

In **figure 42**, the SAC22-029 sample shows a rapid decrease of 7-8% in weight in the temperature range of 0-100°C which is consistent with water removal as a first stage. The slight increase in weight noticed in the temperature range between 240-280°C is most likely a slight error in the instrument scale due to its high sensitivity. The second stage between 290-410°C and shows the highest weight loss of 87% which is the decomposition of the sample. Finally, the fixed weight of around 5% in the temperature range of 410-900°C is the ash content present within the sample.

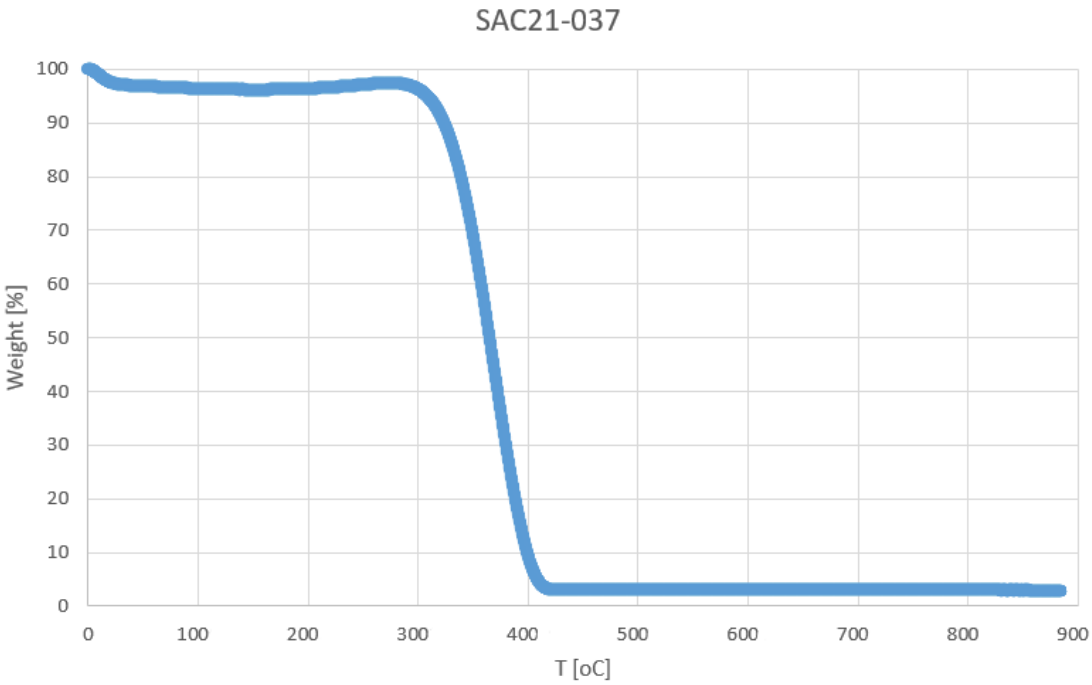

Figure 43. Weight Loss % of SAC21-037

In **figure 43**, the SAC21-037 sample in the first weight loss stage records a 4% weight loss in the temperature range between 0-150°C which is the initial water removal. The weight remains stable, despite the slight weight increase due to the sensitivity of the balance as mentioned earlier, until reaching 295°C where the major decomposition starts. The sample shows a 93% weight loss in the temperature range between 295-405°C which is the decomposition of the sample and the breaking down of molecules. In the temperature range between 405-900°C the weight remains fixed at 3% which is the total ash content remaining from the sample.

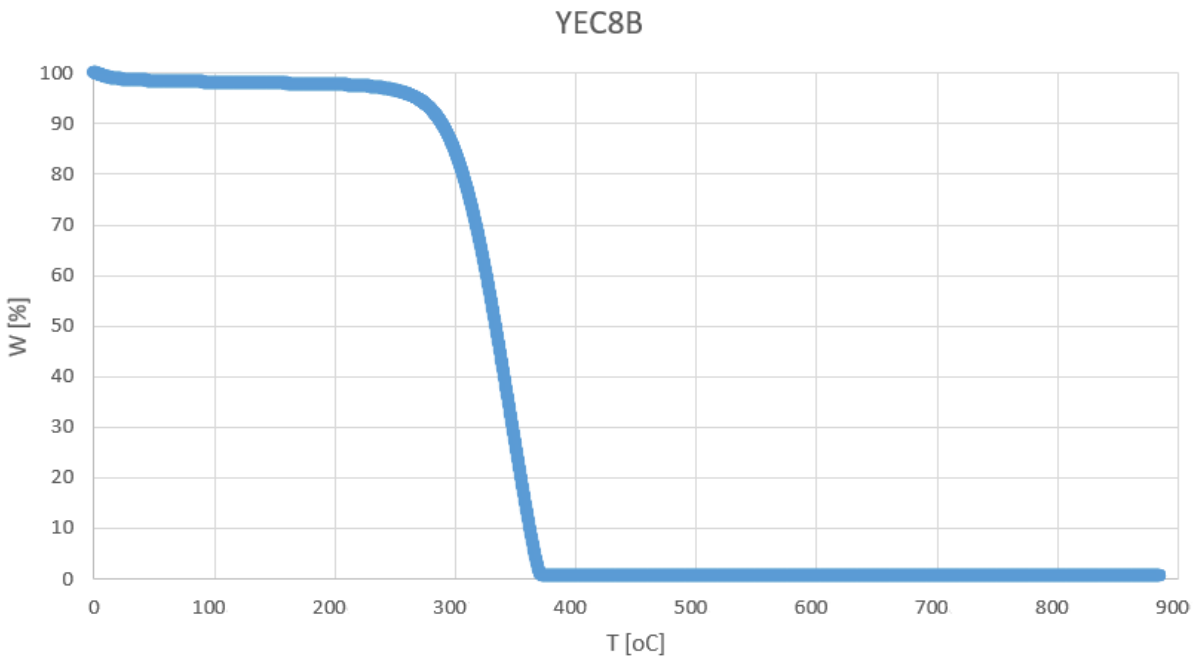

Figure 44. Weight Loss % of YEC8B

In **figure 44**, the YEC8B which is the commercial activated carbon sample shows a 2% initial weight loss in the temperature range between 0-150^{o}C which corresponds to water removal. A further slow and gradual decrease of 1% weight continues in a very stable manner until reaching a temperature of 290^{o}C. In the second stage which is in the temperature range of 290-380^{o}C records the highest weight loss of 96.5%. The remaining fixed weight of 0.5% that is recorded and unchanged between 380-900^{o}C is the ash content in the sample.

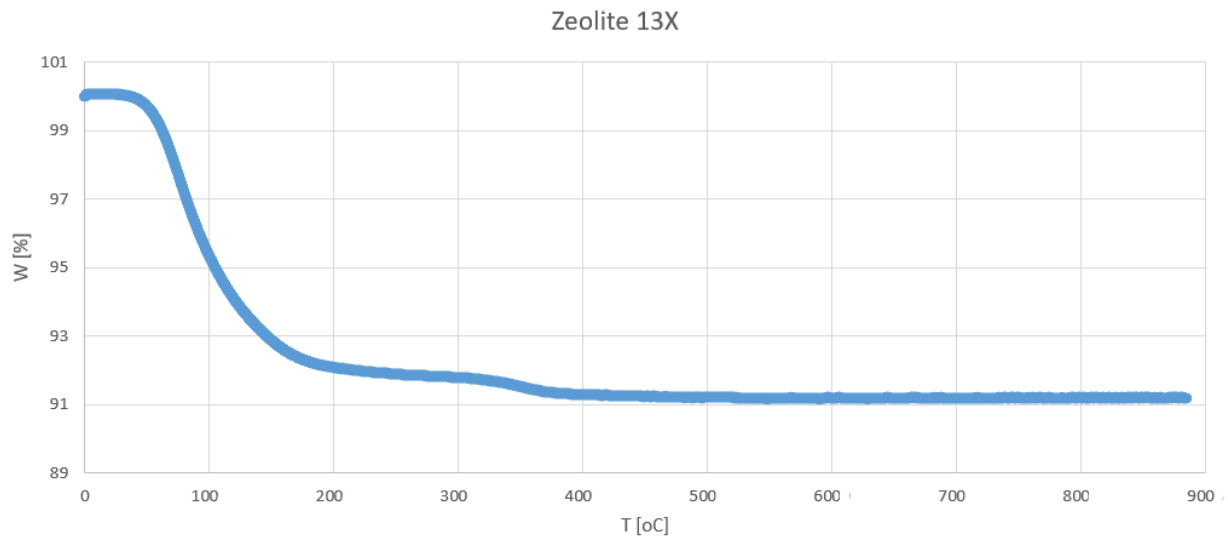

Figure 45. Weight Loss % of Zeolite 13X

The results of the zeolite 13X sample in **figure 45** shows an initial and gradual weight loss of 9% in the temperature range between 85-350°C which is consistent with the weight loss recorded for zeolite 13X sample in [70] where the weight loss due to water removal was 10%. In addition, the thermal stability of zeolite 13X after the initial weight loss remains stable up to 900°C which was the upper limit of the analysis. The TGA analysis in [70] has shown stability up to 1000°C. The zeolite demonstrates such high thermal stability because of its silicon oxide and aluminum oxide bonds. More energy is involved to break the Si-O bonds than it takes to break the Al-O bonds which demonstrated a direct correlation to increased thermal stability with increased Si/Al ratio [71].

4.1.3.1. Comparison

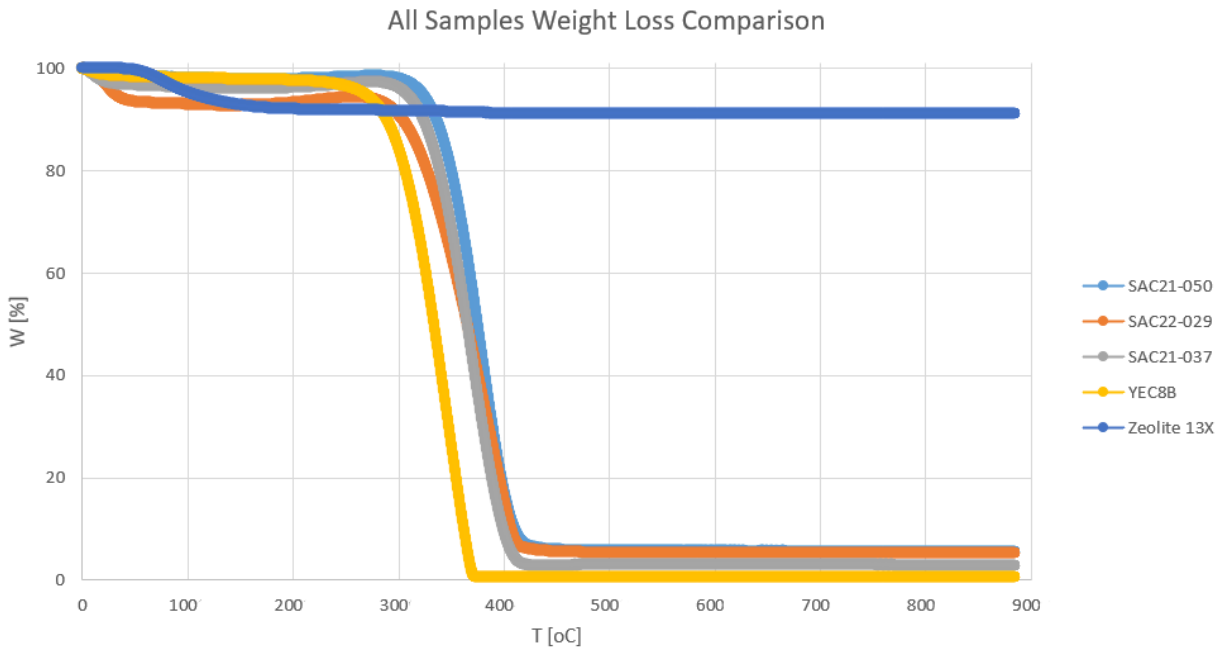

Figure 46. All Samples Weight Loss % Comparison

		Samples									
		SAC21-050		SAC22-029		SAC21-037		YEC8B		Zeolite 13X	
Stage	Parameters	W% Loss	T Range [oC]	W% Loss	T Range [oC]	W% Loss	T Range [oC]	W% Loss	T Range [oC]	W% Loss	T Range [oC]
1	Water Removal	2	0-150	8	0-100	4	0-150	2	0-150	9	85-350
2	Decomposition	93	320-400	87	290-410	93	295-405	96.5	290-380	N/A	N/A
3	Ash Content	5%		5%		3%		0.50%		N/A	

Table 5. TGA Analysis Results Summary

The data was plotted in a single graph illustrated by **figure 46** and the summary is shown in **Table 5** above. In terms of thermal stability, zeolite 13X shows the highest thermal stability among all the samples. SAC21-050 is the next favorable sample in terms of thermal stability where it can withstand 320°C before decomposition which is higher than that of the commercial AC (YEC8B) as well as being higher than the rest of the AC samples tested. The commercial AC (YEC8B) demonstrated the least ash content amongst the samples which was 0.5%. Microporous samples having a low ash content is the most favorable since higher ash contents can cause clogging of active pores resulting in lower surface area and thus lower quality of the AC [67].

4.2. Low Pressure Adsorption Isotherms

Due to the limited number of measurements and the heavy load of students who are using the BELSORP MAX II Adsorption instrument, the highest surface area carbon sample as well as the zeolite 13X sample were chosen to adsorb both nitrogen and carbon dioxide gases at three different temperatures (283.15K,293.15K,303.15K). This will allow the determination of both the heat of adsorption and the CO_2/N_2 selectivity of these chosen samples via the Ideal Adsorbed Solution Theory (IAST) method.

T	Gas	Sample	Degass Time [hr]	Degass T [oC]	Weight Before Degass [g]	Weight After Degass [g]	% Weight Loss
283.15 K	N2	**SAC21-050**	5(+1)	200(+250)	0.1299	0.1247	4.003079292
		Zeolite 13X	5(+1)	200(+250)	0.3906	0.3825	2.073732719
	CO2	**SAC21-050**	5(+1)	200(+250)	0.1757	0.1685	4.097894138
		Zeolite 13X	5(+1)	200(+250)	0.384	0.374	2.604166667
293.15K	N2	**SAC21-050**	5(+1)	200(+250)	0.1319	0.1253	5.003790751
		Zeolite 13X	5(+1)	200(+250)	0.4489	0.4364	2.78458454
	CO2	**SAC21-050**	5(+1)	200(+250)	0.178	0.1726	3.033707865
		Zeolite 13X	5(+1)	200(+250)	0.4239	0.4151	2.075961312
303.15K	N2	**SAC21-050**	5(+1)	200(+250)	0.1497	0.1432	4.342017368
		Zeolite 13X	5(+1)	200(+250)	0.442	0.4288	2.986425339
	CO2	**SAC21-050**	5(+1)	200(+250)	0.1231	0.1167	5.199025183
		Zeolite 13X	5(+1)	200(+250)	0.4323	0.4223	2.31320842

Table 6. Sample Preparation for LP Adsorption

Table 6 represents all the sample weights used in the LP adsorption measurements. It should be noted that the degassing of the samples was done for 5 hours at 200°C externally in the Belprep Degasser followed by 1 hour within the Belsorp instrument itself at 250°C to minimize any moisture adsorption when transferring the tubes from the degasser to the Belsorp unit. The percent weight loss for all carbon samples as well as the zeolite samples are consistent and are highlighted for comparison.

4.2.1. LP Nitrogen Adsorption Isotherms

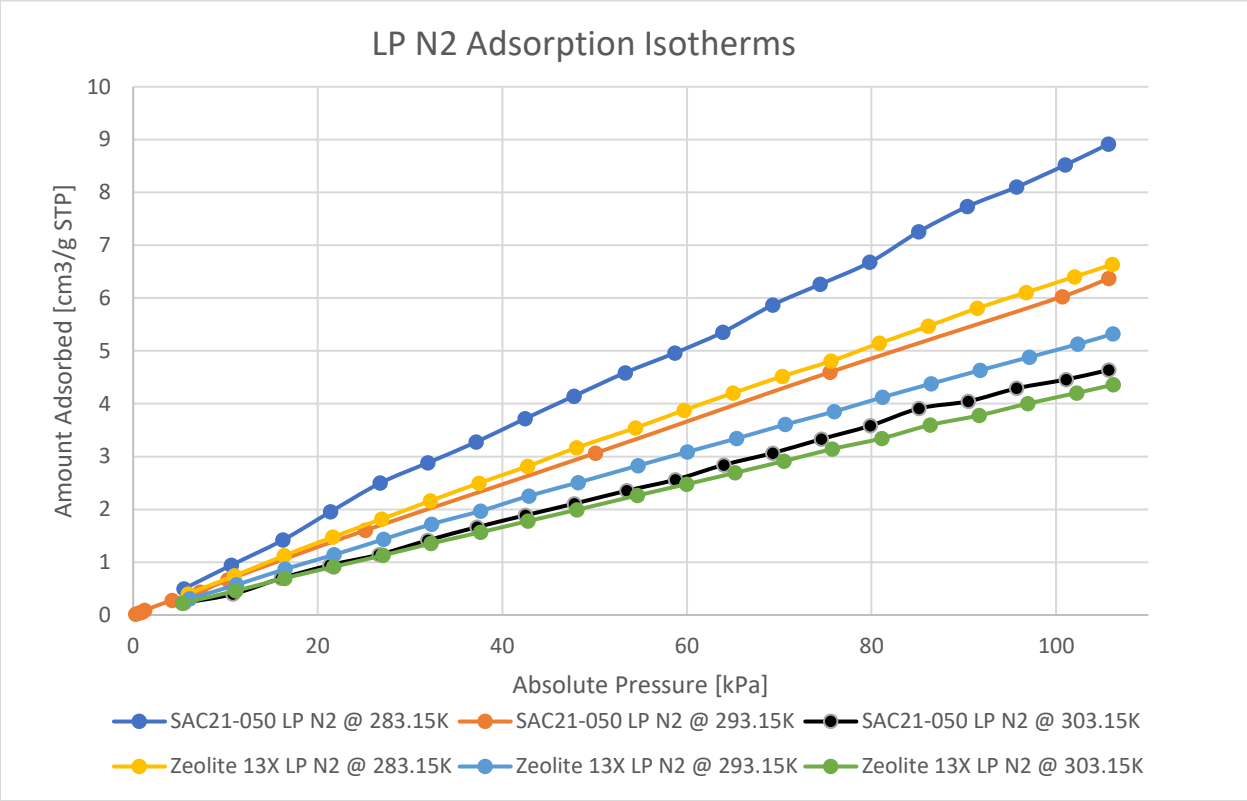

Figure 47. LP Nitrogen Adsorption Isotherms of Samples

Figure 47 shows the adsorption capacity of Nitrogen on the two chosen samples at three different temperatures. Physisorption is an exothermic process where heat is released upon the adsorption of gas, thus increasing the temperature will result in a decrease in adsorption capacity as illustrated for both samples. SAC21-050 at 283.15K shows the highest Nitrogen adsorption capacity of 9 cm^3/g up to 1 bar pressure which outperforms the Zeolite 13X having 6.8 cm^3/g at the same temperature condition and 1 bar. In addition, further increasing the temperature results in decreased adsorption capacity for both samples, however in all cases the SAC21-050 adsorbs more N_2 than Zeolite 13X sample suggesting different heat of adsorption. At 77K, SAC21-050 was able to adsorb 1200 cm^3/g of nitrogen compared to the 9 cm^3/g at 283.15K which shows that nitrogen adsorbs more at low temperatures. The nitrogen physisorption BET graphs are also consistent with the above graphs where all the activated carbon samples had higher adsorption capacities for nitrogen compared to the zeolite 13X sample suggesting that AC has a higher affinity towards nitrogen.

4.2.2. LP Carbon Dioxide Adsorption Isotherms

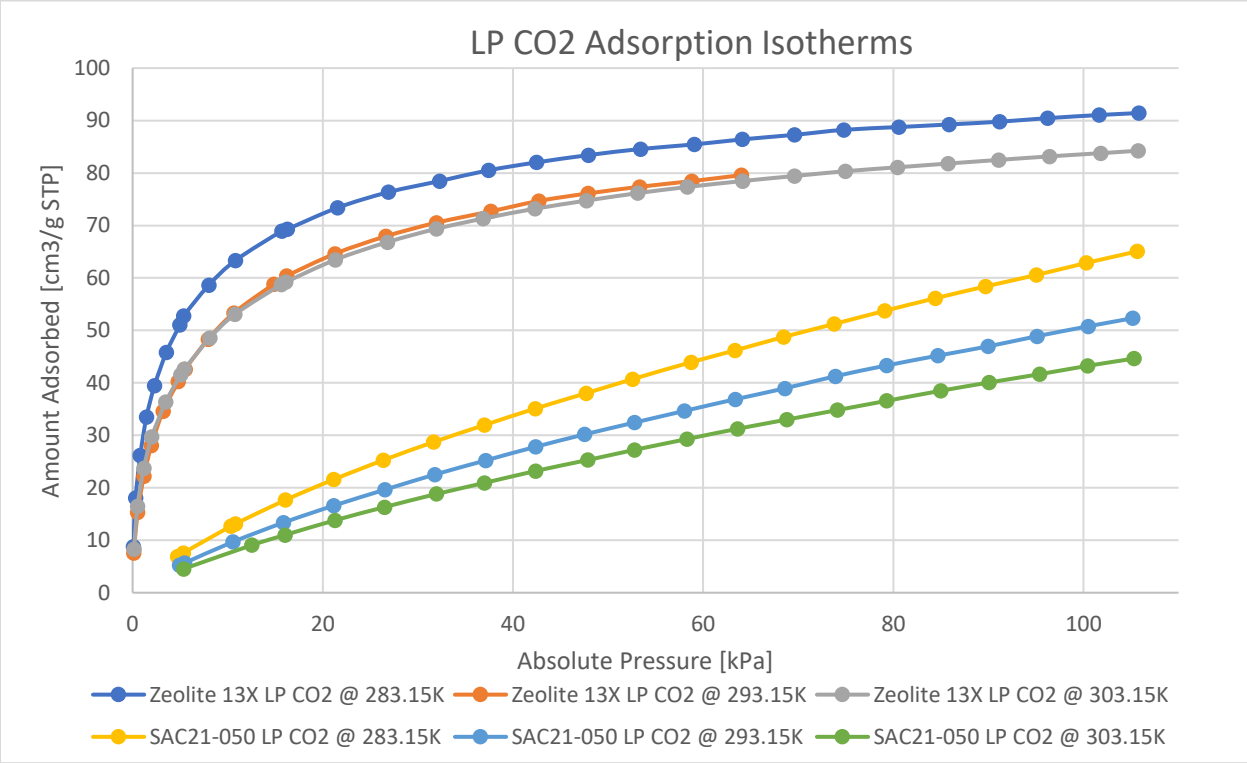

Figure 48. LP Carbon Dioxide Adsorption Isotherms of Samples

Figure 48 shows the adsorption capacity of carbon dioxide on the two chosen samples at three different temperatures. Firstly, it is noticed that with increased temperature the adsorption capacity for both samples decreases which is consistent with the literature. In addition, zeolite 13X shows the highest adsorption capacity at 283.15K of 92 cm^3/g of CO_2 adsorbed up to 1 bar compared to that of SAC21-050 which is 66 cm^3/g at the same temperature. The adsorption isotherm of Zeolite is sharper than the linear adsorption isotherm of SAC21-050 which suggests a higher affinity towards CO_2 molecules. SAC21-050 adsorbs CO_2 in a linear manner which means it has weaker bonds with CO_2 and can fully regenerate/desorb as compared to Zeolite 13X.

4.3. Adsorption Model Fitting

After careful consideration of the different existing models in the literature, the Langmuir and the Dual-Site Langmuir-Freundlich models were chosen to fit the experimental data. Based on relevant literature reviews, the model fitting will give a better understanding of the effect of surface heterogeneity of carbon dioxide and nitrogen adsorption on SAC21-050 and Zeolite 13X.

4.3.1. Langmuir Model Fitting

The Langmuir model is expressed in **section 2.1.2** however for simplicity the equation will be described again in the variable terms that I have used in my fitting calculations which is expressed by equation (16):

$$q = q_{max} \times \frac{\mathrm{KP}}{1+\mathrm{KP}} \quad (16)$$

In addition, the equation for the coefficient of determination was calculated through the "R-Squared" function on excel and it is based on equation (17):

$$R^2 = 1 - \frac{Sum\ of\ Squares\ of\ Residuals}{Total\ Sum\ of\ Squares} \quad (17)$$

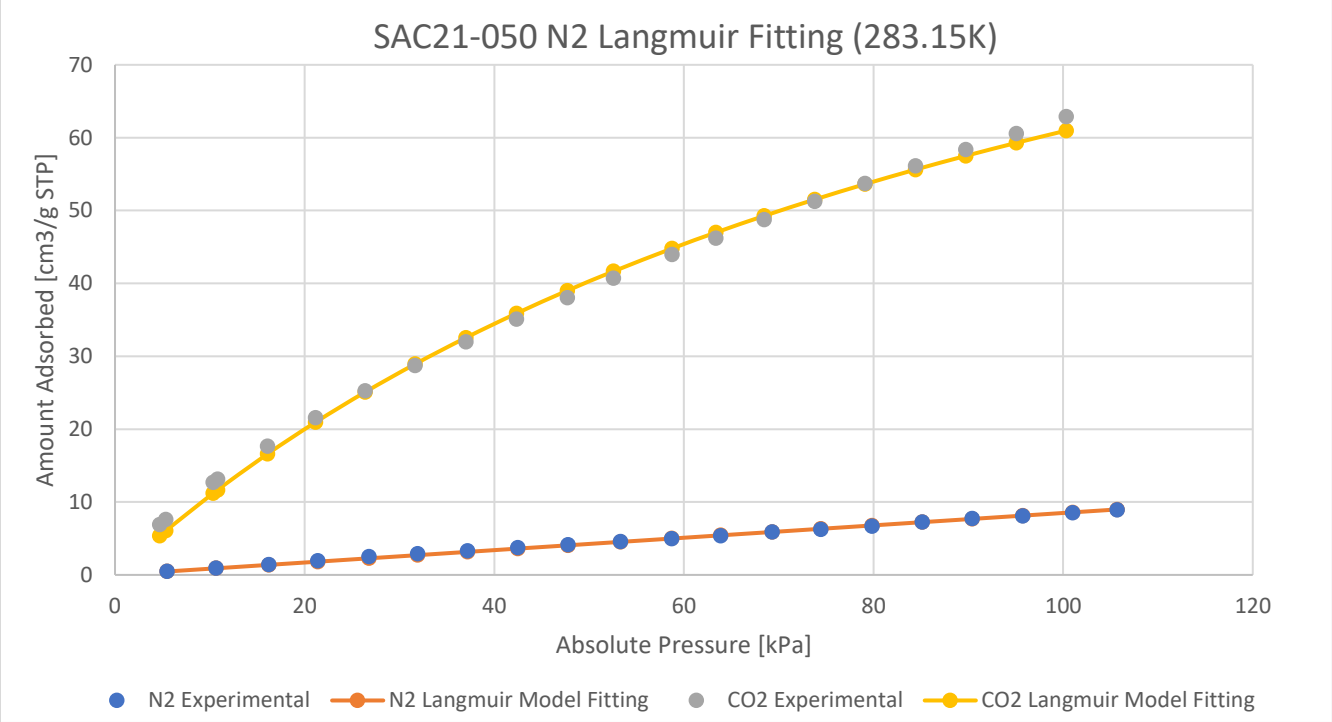

Figure 49. Langmuir Model Fitting on SAC21-050 (283.15K)

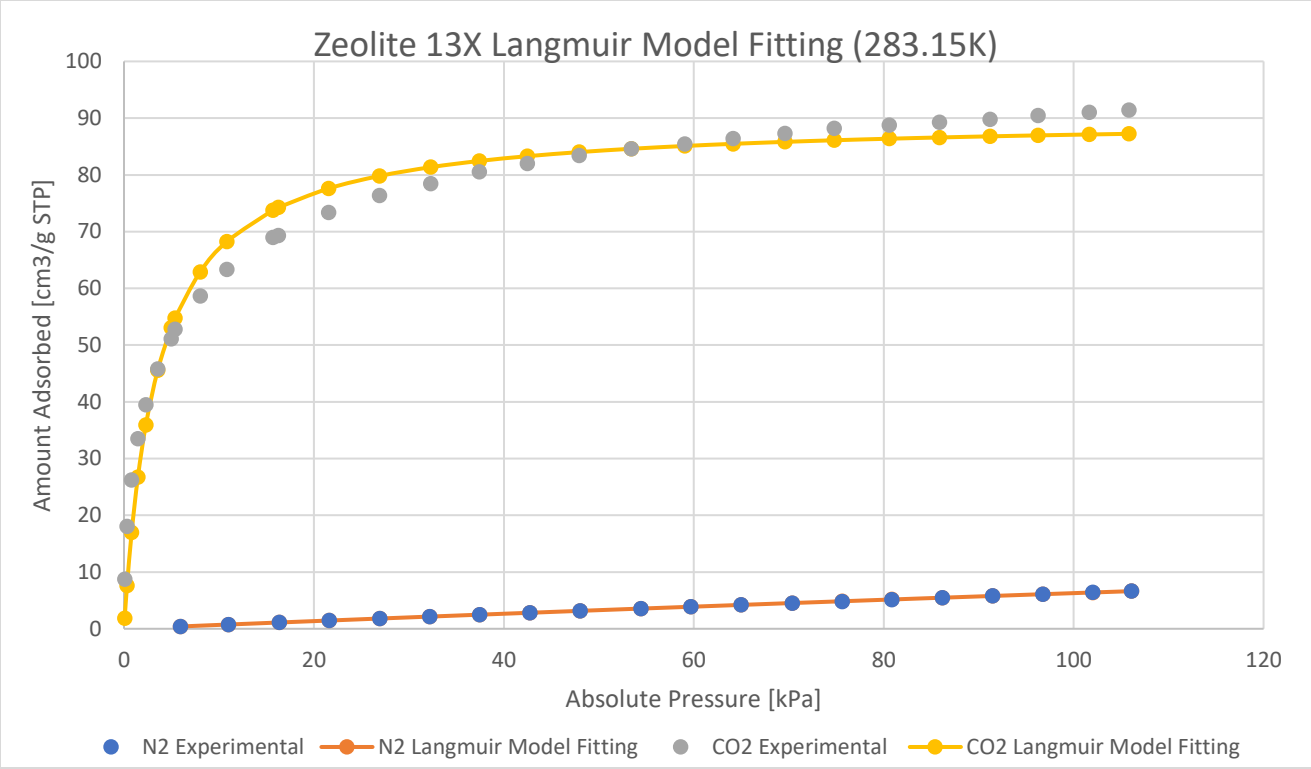

Figure 50. Langmuir Model Fitting on Zeolite (283.15K)

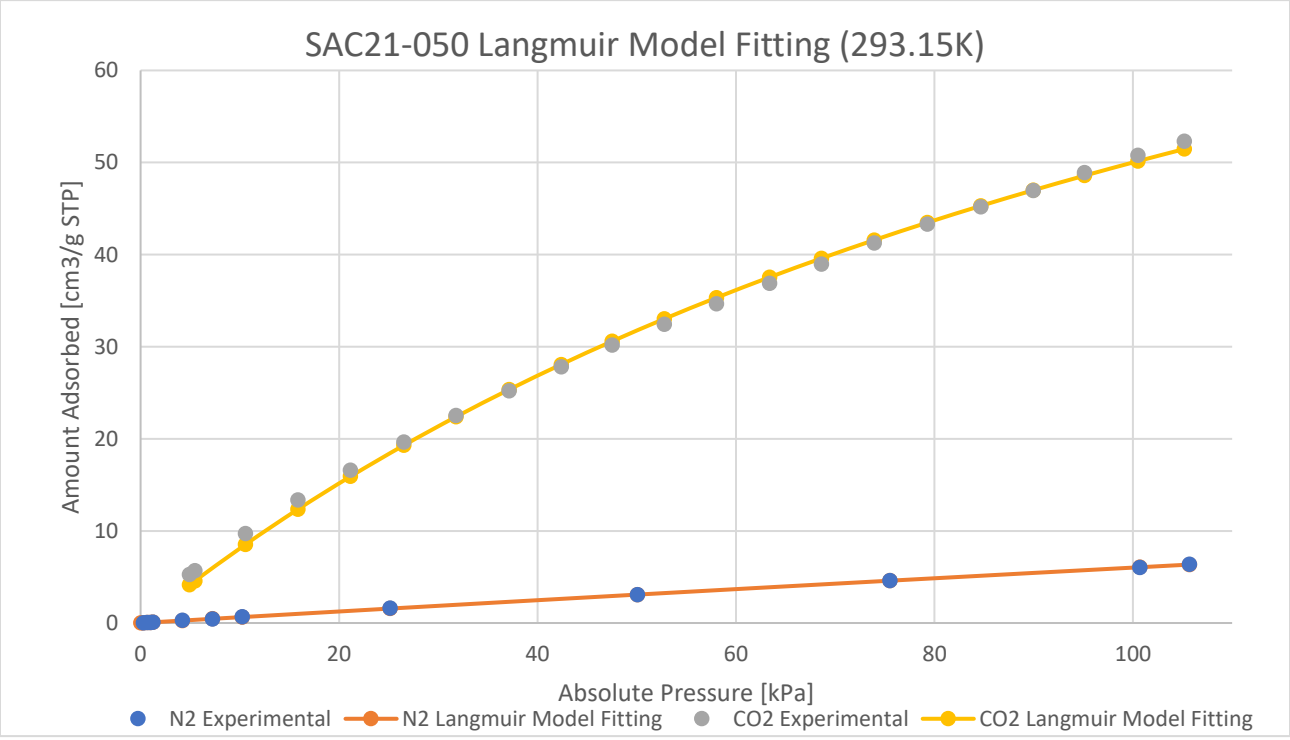

Figure 51. Langmuir Model Fitting on SAC21-050 (293.15K)

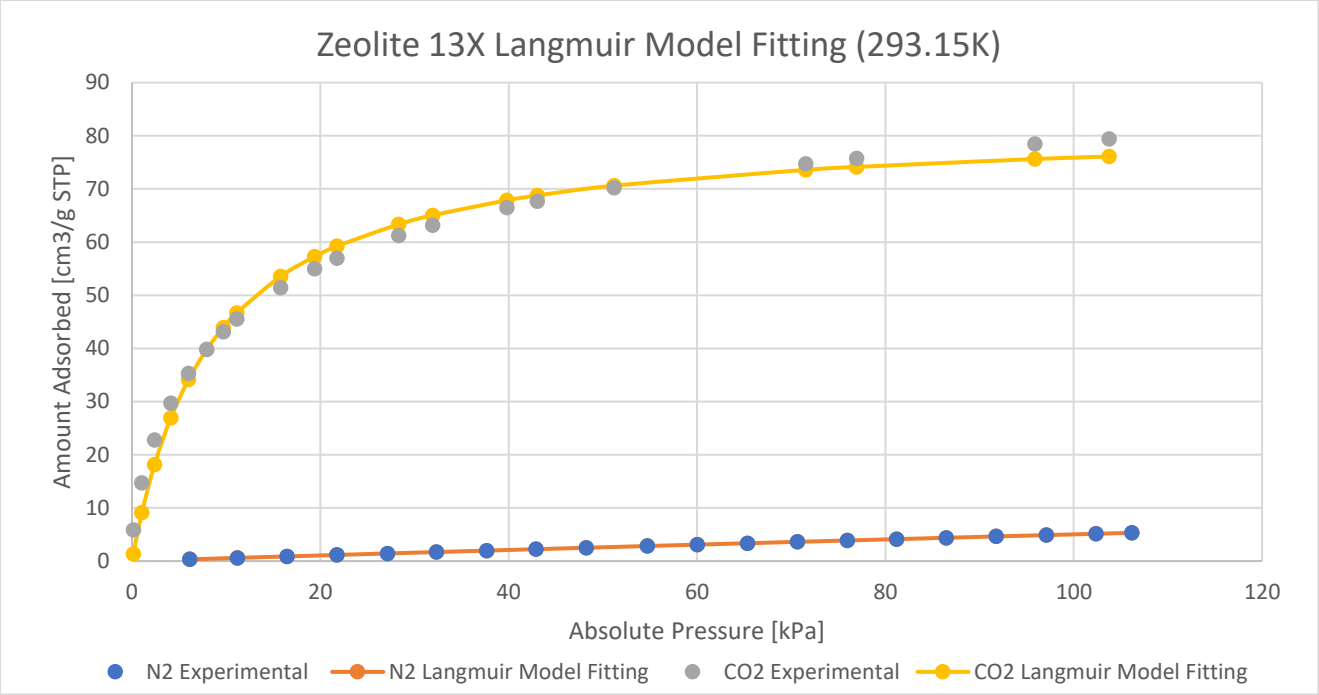

Figure 52. Langmuir Model Fitting on Zeolite (293.15K)

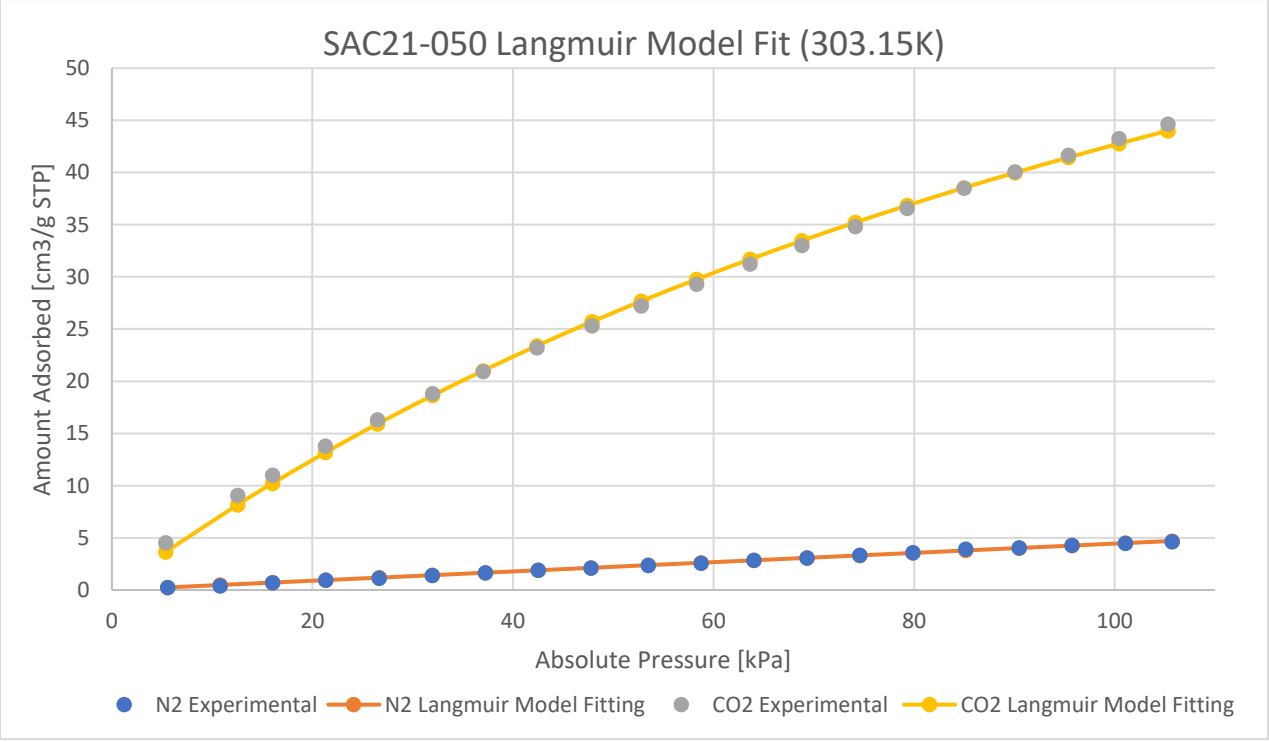

Figure 53. Langmuir Model Fitting on SAC21-050 (303.15K)

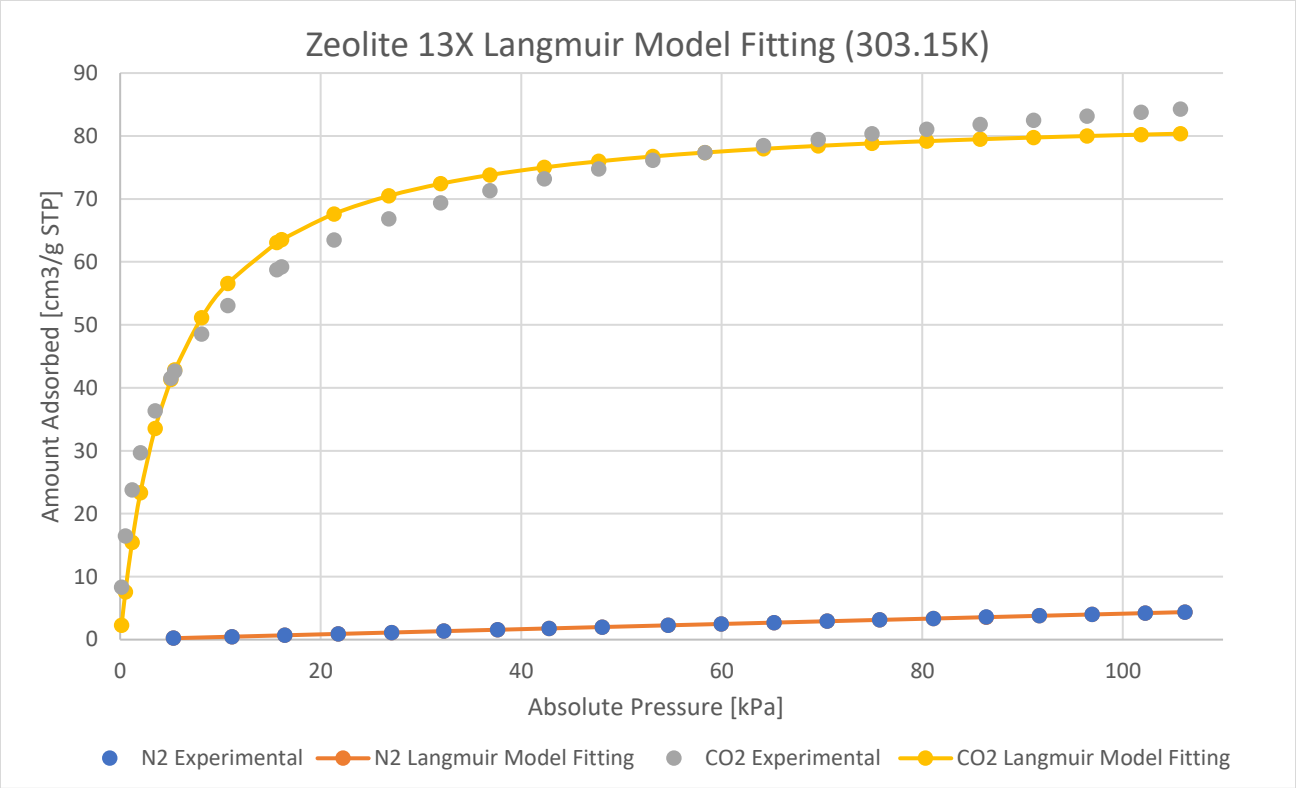

Figure 54. Langmuir Model Fitting on Zeolite 13X (303.15K)

The data shown in **figures 49-54** show the fitting of the experimental data on the Langmuir adsorption model. The model does not accurately fit the experimental data where there are visual deviations. It is expected that the coefficient of determination will not be very high especially for the carbon dioxide data which is affected by the heterogeneity of the adsorbent surface.

4.3.2. DSLF Model Fitting

The DSLF model is expressed in **section 2.1.5** however for simplicity I will describe the equation again in the variable terms that I have used in my fitting calculations which is expressed by equation (18):

$$q = q_1 \frac{b_1 p^{c_1}}{1+b_1 p^{c_1}} + q_2 \frac{b_2 p^{c_2}}{1+b_2 p^{c_2}} \quad (18)$$

In addition, the equation for the coefficient of determination was calculated through the "R^2" function on excel and it is based on the same equation (17) stated earlier.

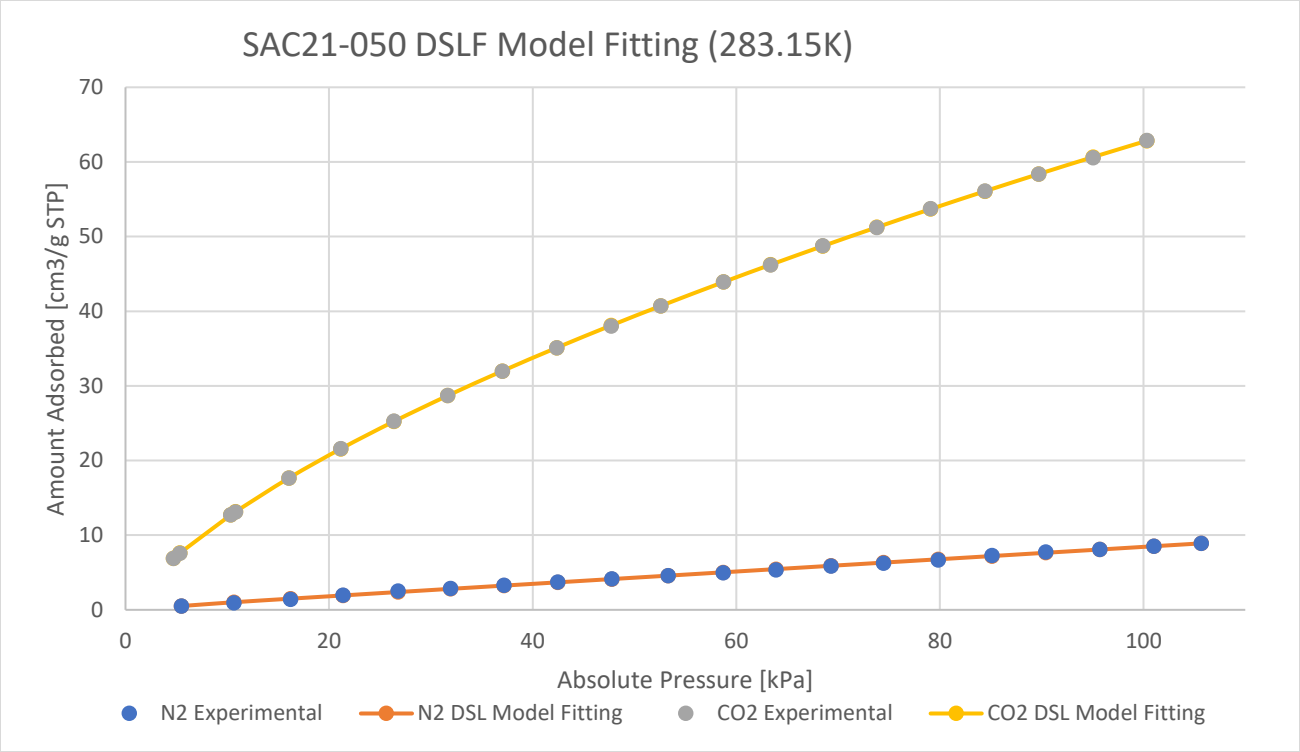

Figure 55. DSLF Model Fitting for SAC21-050 (283.15K)

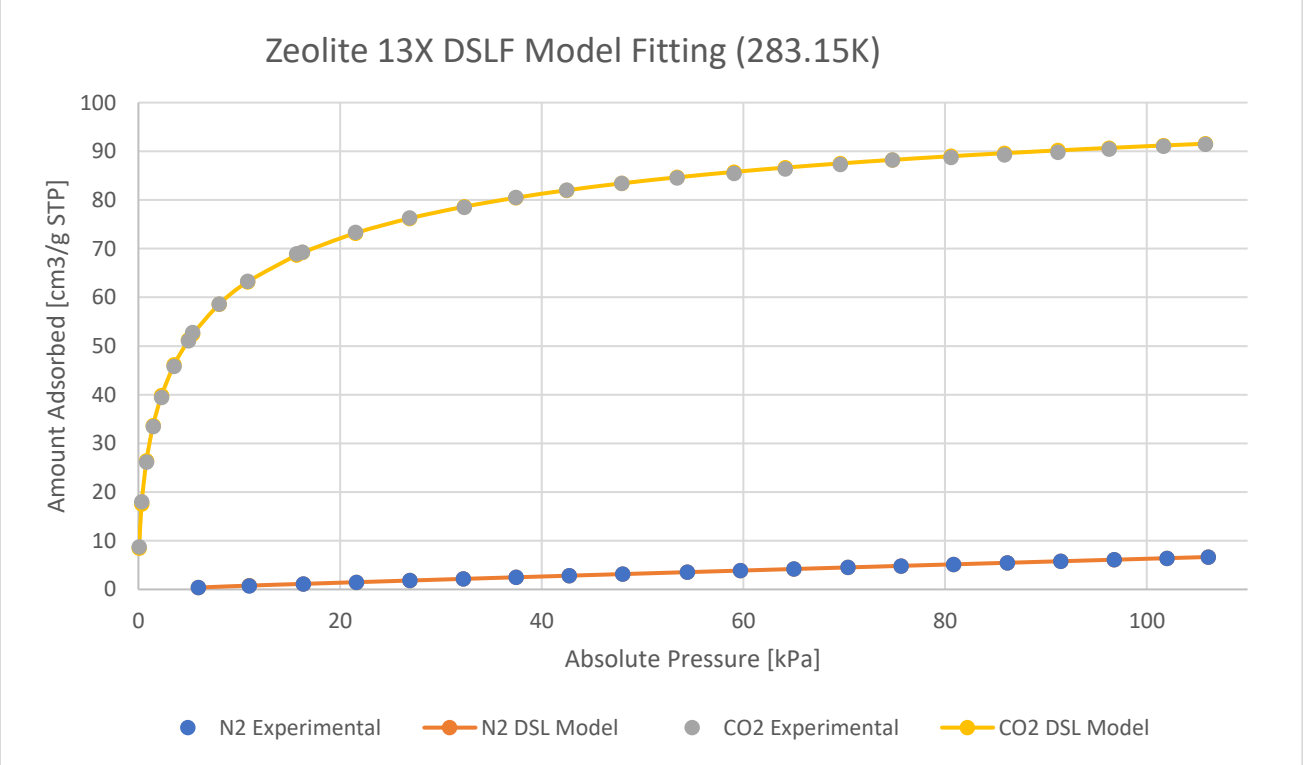

Figure 56. DSLF Model Fitting for Zeolite 13X (283.15K)

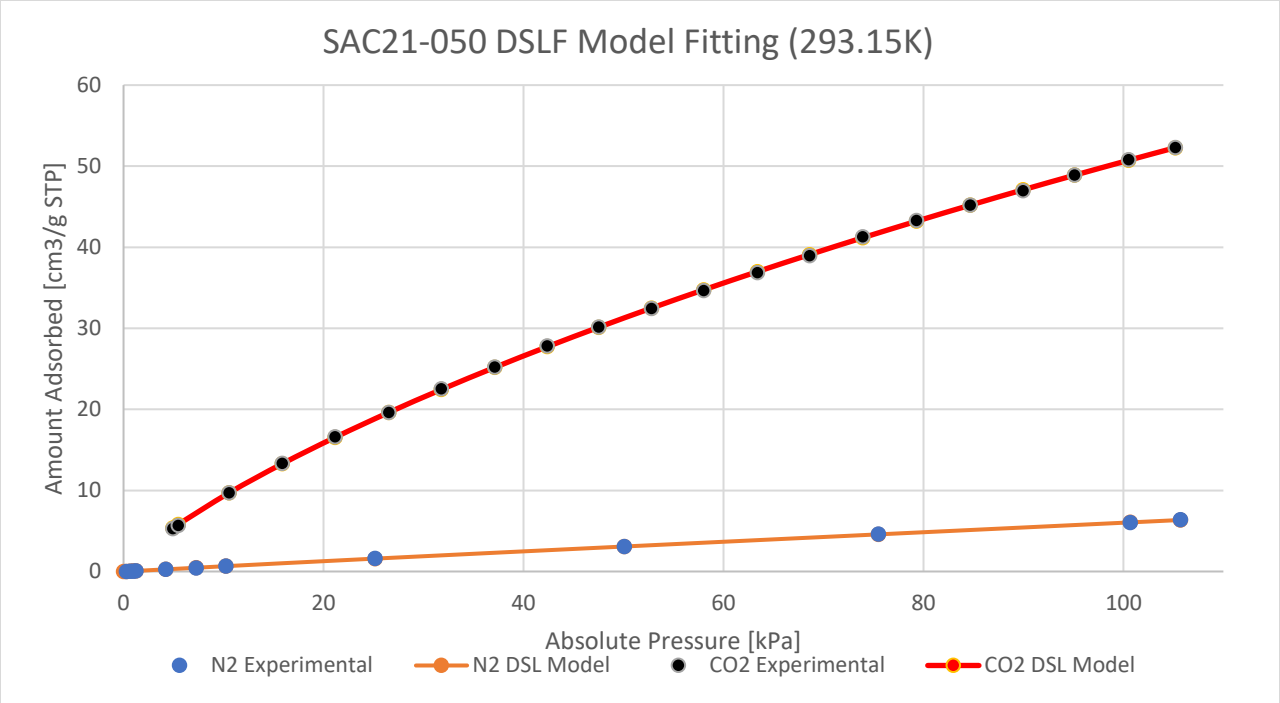

Figure 57. DSL Model Fitting for SAC21-050 (293.15K)

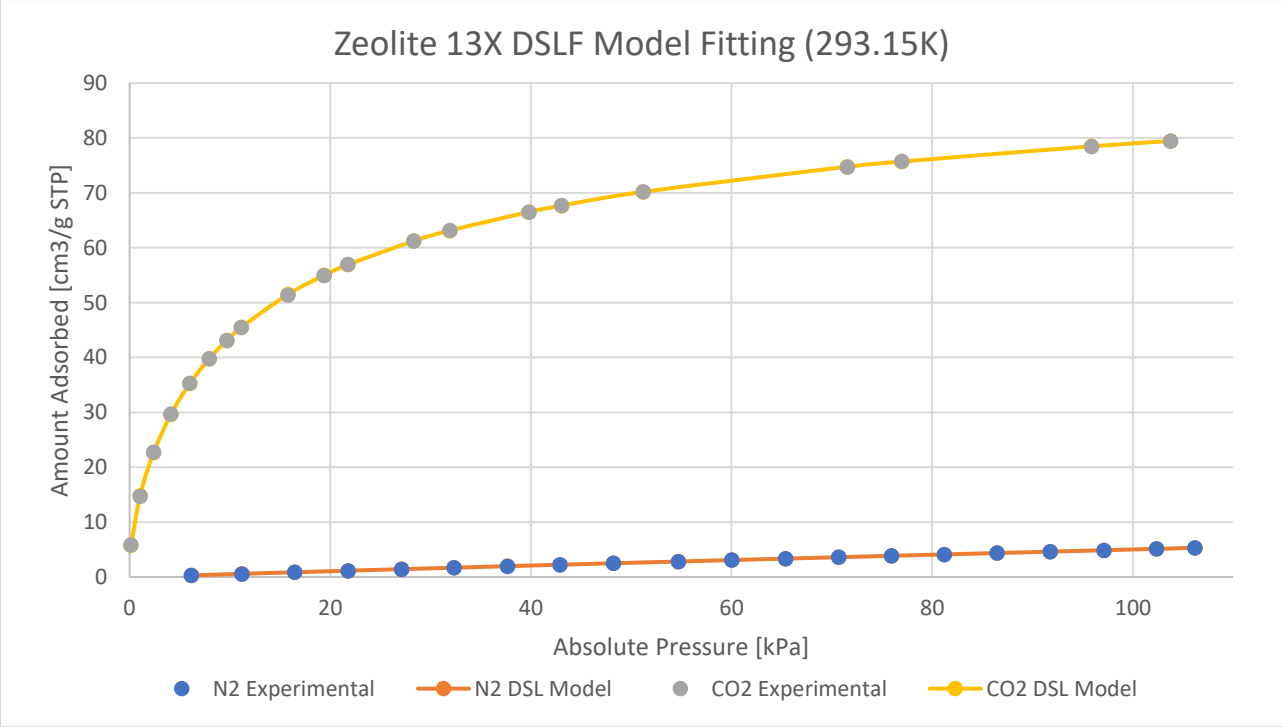

Figure 58. DSL Model Fitting for Zeolite 13X (293.15K)

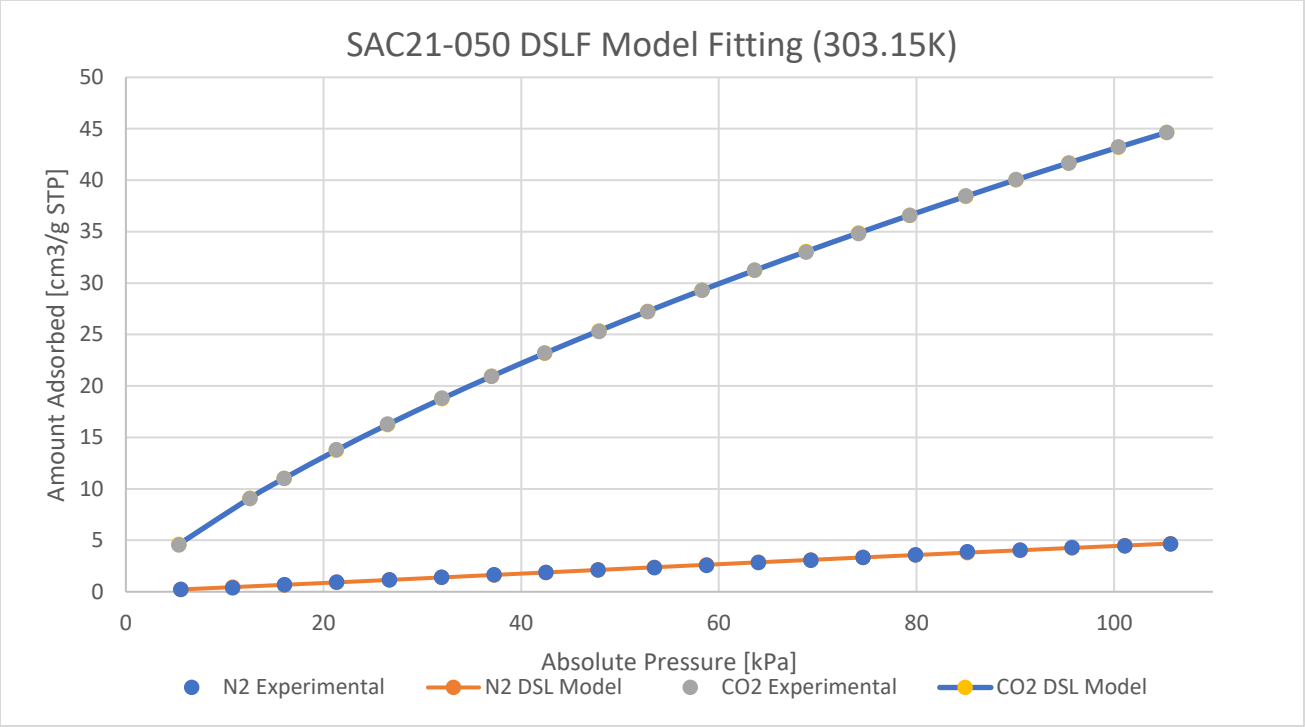

Figure 59. DSL Model Fitting for SAC21-050 (303.15K)

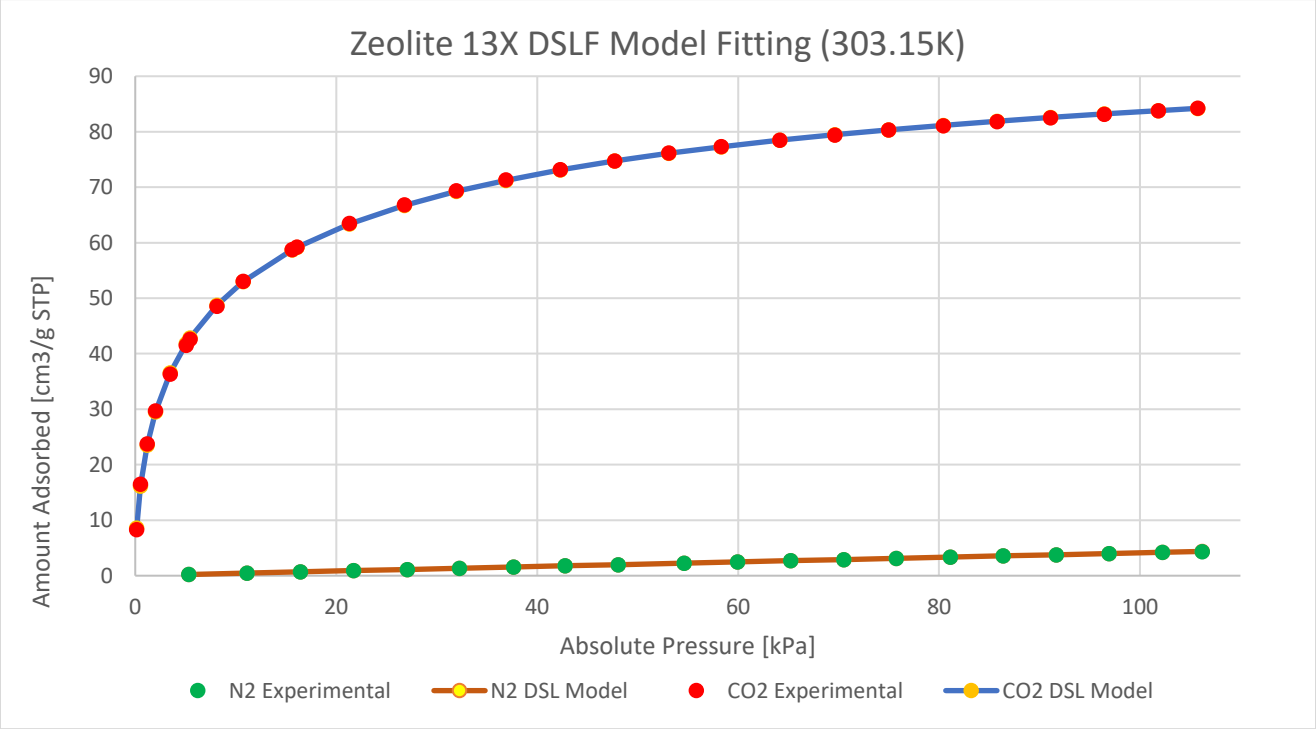

Figure 60. DSL Model Fitting for Zeolite 13X (303.15K)

As compared to the Langmuir model, the visual representation of the data in **figures 55-60** shows a much more accurate fit where it is expected to have a higher coefficient of determination. The effect of

considering the surface heterogeneity constant in the DSLF model gives a more accurate representation of the data.

4.3.3. Fitting Parameters Comparison

			Langmuir Model			Dual-Site Langmuir-Freundlich Model						
Sample	Gas	Parameters	qmax	K	R^2	q1	q2	b1	b2	c1	c2	R^2
SAC21-050	N2	283.15K	0.5592	0.9273	**0.9993**	57.201	0.9601	0.0016	0.0495	0.6745	1.0786	**0.9994**
		293.15K	125.7206	0.0005	**0.9999**	0.3568	0.1298	0.01948	0.6574	1.296	1.0221	**0.9999**
		303.15K	5191.444	0.000008	**0.9991**	22.6382	0.8598	0.0008	0.0339	1.2055	0.6552	**0.9993**
	CO2	283.15K	124.4966	0.0096	**0.9973**	82.2106	73.1241	0.0234	0.0001	0.8544	1.7676	**0.9999**
		293.15K	117.5913	0.0074	**0.9989**	112.5894	208.6828	0.0024	0.006	0.8227	0.7979	**0.9999**
		303.15K	108.1367	0.0065	**0.9987**	108.9495	48.1141	0.0108	0.0001	0.8295	1.6381	**0.9999**
Zeolite 13X	N2	283.15K	74.2372	0.0009	**0.9999**	0	2.6901	0.07947	0.0311	0	0.9448	**0.9999**
		293.15K	80.1239	0.0007	**0.9999**	5.5034	0.0399	0.0078	0.1137	1.0253	1.389	**0.9999**
		303.15K	243.1103	0.0002	**0.9999**	0	2.8188	0.01834	0.01563	0	0.9887	**0.9999**
	CO2	283.15K	90.0972	0.2882	**0.9874**	55.657	55.657	0.3512	0.3512	0.5534	0.5534	**0.9999**
		293.15K	82.3174	0.1179	**0.9901**	191.5343	62.2397	0.0403	0.1277	0.2841	0.8598	**0.9999**
		303.15K	84.3824	0.1892	**0.9879**	54.4703	54.4703	0.251	0.251	0.5595	0.5595	**0.9999**

Table 7. Fitting Parameters Table Comparison

The fitting parameters in **Table 7** along with the non-linear regression fitting graphs of both models clearly shows that the Dual-Site Langmuir-Freundlich model fits the experimental data more accurately than the Langmuir model. To perform the IAST selectivity analysis, the DSLF model is chosen due to its accuracy in representing the data.

4.4. IAST Selectivity Analysis

The Ideal Adsorbed Solution theory is a thermodynamic approach which was developed by Myers and Prausnitz. This theoretical approach accurately predicts the adsorption of a mixture of gases using single pure component isotherm data of those gases [72]. This is performed on the condition that the experimental isotherm data fits with the chosen adsorption model to a high degree of precision ($R^2 > 0.999$)[25]. As seen in the previous sections, the DSLF model very accurately fits the adsorption experimental data as depicted by the value of R^2 shown in **Table 7** compared to the Langmuir model. In this method, the adsorbed phase (gas) is considered to have no interaction or changes in the system which means the mole fractions used in the equation is for gas mole fraction (y_i) and the liquid mole fraction (x_i) remains a constant. The general term for selectivity by IAST is expressed by equation (16) [72]:

$$S_{CO2,N_2} = \frac{x_{CO_2}/x_{N_2}}{y_{CO_2}/y_{N_2}} \rightarrow \frac{y_{N_2}}{y_{CO_2}} \quad (16)$$

The accuracy of the model allows to implement it in the IAST method for predicting the selectivity of CO2 over N2 for the samples tested through equation (17) specific for the DSL model:

$$S_{CO2/N2} = \frac{y_{N_2}}{y_{CO_2}} \times \frac{q_{1,CO_2}\frac{b_1 p_.^{c_1}}{1+b_1 p_.^{c_1}} + q_{2,CO_2}\frac{b_2 p_.^{c_2}}{1+b_2 p_.^{c_2}}}{q_{1,N_2}\frac{b_1 p_.^{c_1}}{1+b_1 p_.^{c_1}} + q_{2,N_2}\frac{b_2 p_.^{c_2}}{1+b_2 p_.^{c_2}}} \quad (17)$$

The CO_2/N_2 mixture is relevant to common flue gas stream compositions containing CO_2 and N2 mentioned in the literature and that is having 85% N_2 ($y_{N_2} = 0.85$) and 15% CO_2 ($y_{CO_2} = 0.15$) mixtures.

The resulting selectivity results are plotted against a pressure range from 0-100 kPa at an increment of 1 kPa.

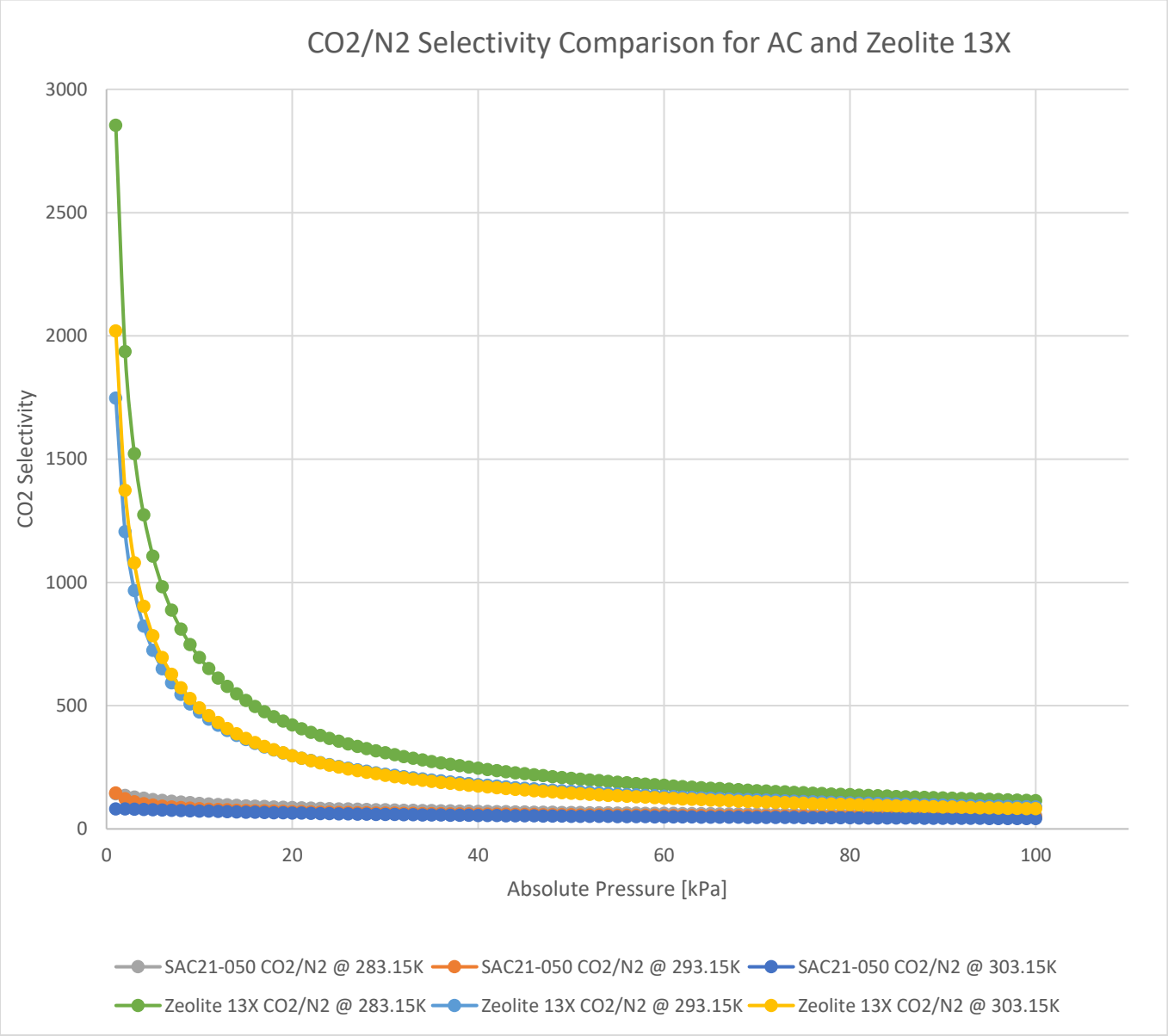

Figure 61. Predicted CO2 Selectivity Comparison

The predicted selectivity of SAC21-050 as well as Zeolite 13X on CO_2 over N_2 is consistent with the experimental results. Zeolite 13X shows a higher selectivity of CO2 over N_2 which is clear from the adsorption isotherms shown in the previous section as well. It has been reported that the highest CO_2/N_2 selectivity on AC is not by having the highest CO_2 adsorption condition, but at the lowest N_2 adsorption condition [73]. Zeolite can thus adsorb carbon dioxide more naturally than activated carbon. Equilibrium separation is the term used to describe the separation of CO_2 through electrostatic interaction between the gas and solid adsorbent [74]. There are several factors that affect the selective electrostatic interaction of the gas molecules with the surface of zeolites which includes Si/Al ratio, polarity and polarizability, in addition to the electric field gradient that increases with decreasing Si/Al ratio [75]. This ratio has a very

significant effect on the selectivity of polar molecules. The lower the ratio, the higher the presence of Al thus increasing the cationic framework in the zeolite which are the active sites that allow adsorption. Even though CO_2 is a nonpolar molecule, which means having an unequal distribution of electron density, it is selectively adsorbed on the zeolite due to its large quadrupole moment compared to other gases as shown in the table below.

	Kinetic diameter (Å)	Quadrupole ($C\ m^{-2}$)	Polarizability (cm^3)
CO_2	3.30	13.4×10^{-40}	2.65×10^{-24}
N_2	3.64	4.6×10^{-40}	1.76×10^{-24}
CH_4	3.80	0	2.60×10^{-24}

Figure 62. Table comparing size, quadrupole moment, and polarizability of different gases ([76],[77])

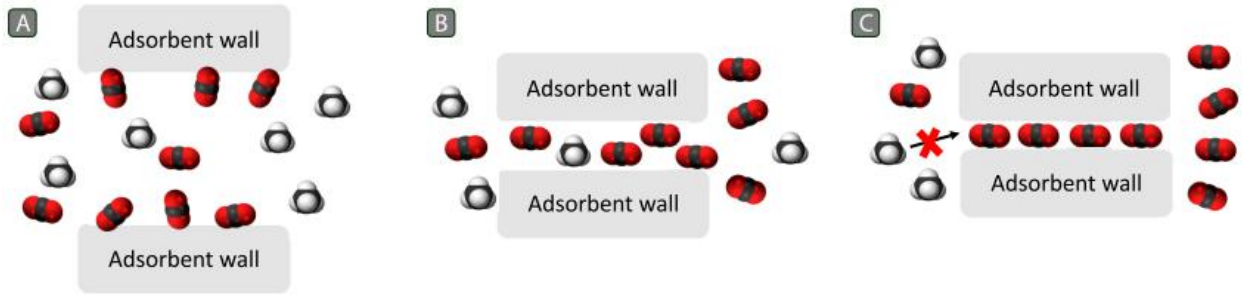

Figure 63. Adsorption Mechanism on different pore-sized Zeolite of a CO2/CH4 gas mixture (A: Equilibrium Separation, B: Kinetic Separation, C: Molecular Sieving Separation) [40]

As a result of the strength of interaction between CO2 and zeolite, it can be selectively separated from gas streams containing N_2 and CH_4. The mechanism of separation in Zeolite 13X follows equilibrium separation as seen in **figure 63-A** where carbon dioxide selectively adsorbs on the surface while the methane passes through. However, in smaller pore-sized Zeolites such as 3A-4A-5A, the selectivity of CO_2 on the surface is dependent on the rate of diffusion of the gas into the pore structures. As stated in the table above noted by **figure 62**, carbon dioxide molecules have a kinetic diameter of 0.33 nm which is smaller than that of nitrogen or methane which will affect the diffusivity of the gases through the smaller-sized pores of this type of zeolite [78]. For smaller pore-sized zeolites, the adsorption mechanism for a CO_2/CH_4 and CO_2/N_2 gas mixtures follows that of kinetic separation and/or molecular sieving separation as shown in **figure 63-B** and **63-C**. **Figure 63-B** illustrates carbon dioxide having a smaller kinetic diameter than methane which diffuses faster through the pore structure. However, in **figure 63-C** the molecular sieving effect having pore size being large enough to allow carbon dioxide (0.33 nm) to pass through while being small enough to restrict the larger nitrogen and methane molecules (0.364 nm and 0.38 nm respectively) from passing through to the pores [79]. Understanding the mechanism of adsorption on Zeolite 13X due to its pore size and surface chemistry confirms the selectivity results obtained in **figure 61** when compared to activated carbons.

4.5. Heat of Adsorption

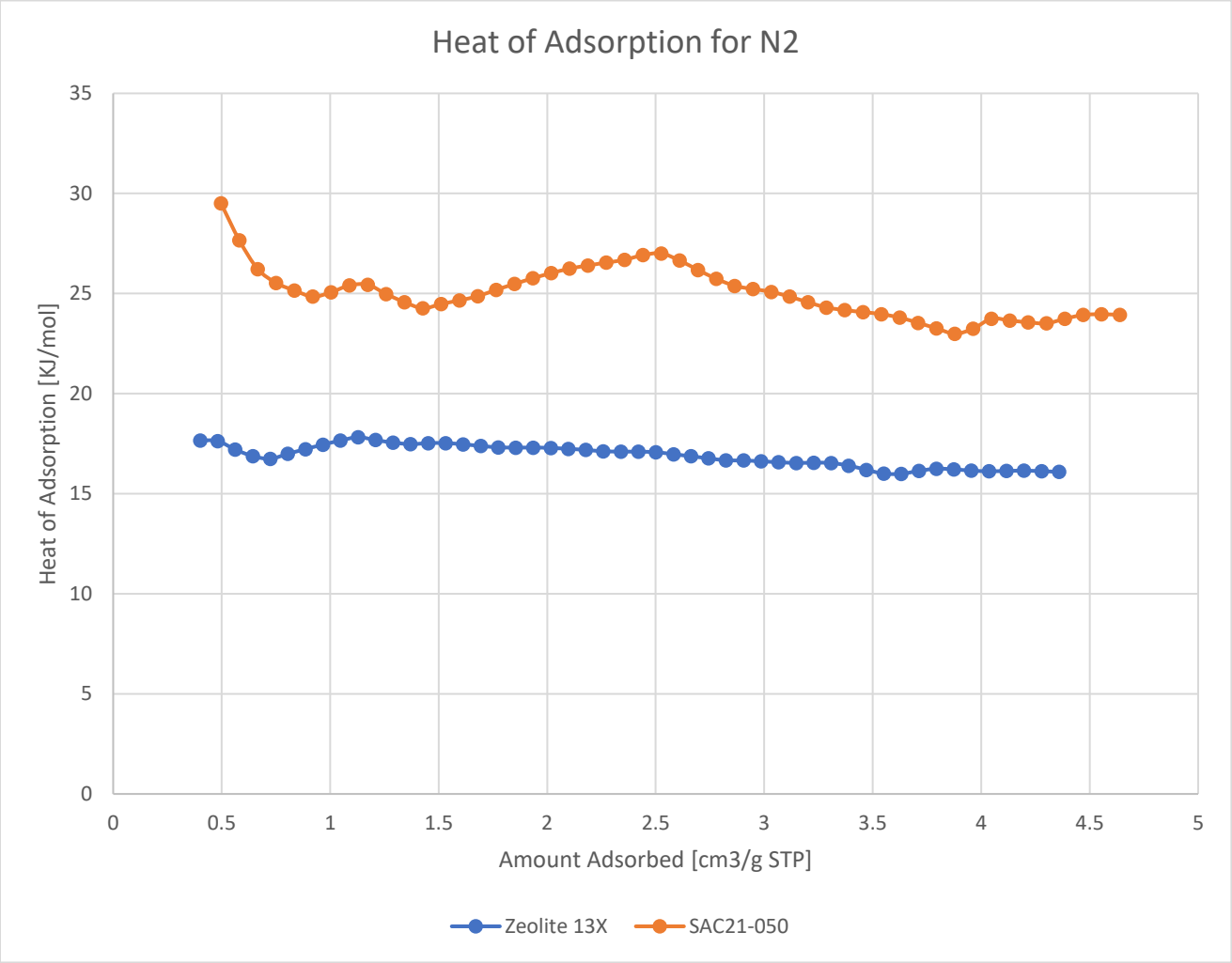

Figure 64. Heat of Adsorption of samples (N2)

Along with the pore size distribution data, adsorption data, and selectivity; The heat of adsorption of N_2 and CO_2 were also calculated, and they are consistent with the experimental data presented earlier. In **figure 64**, SAC21-050 shows a higher heat of adsorption for N_2 which translates to having a higher affinity towards N2 adsorption than that of Zeolite 13X. The mean heat of adsorption of N_2 across the range of data points for SAC21-050 is 25 KJ/mol as compared to 17 KJ/mol for Zeolite 13X which shows a stronger bond between nitrogen molecules and the activated carbon sample.

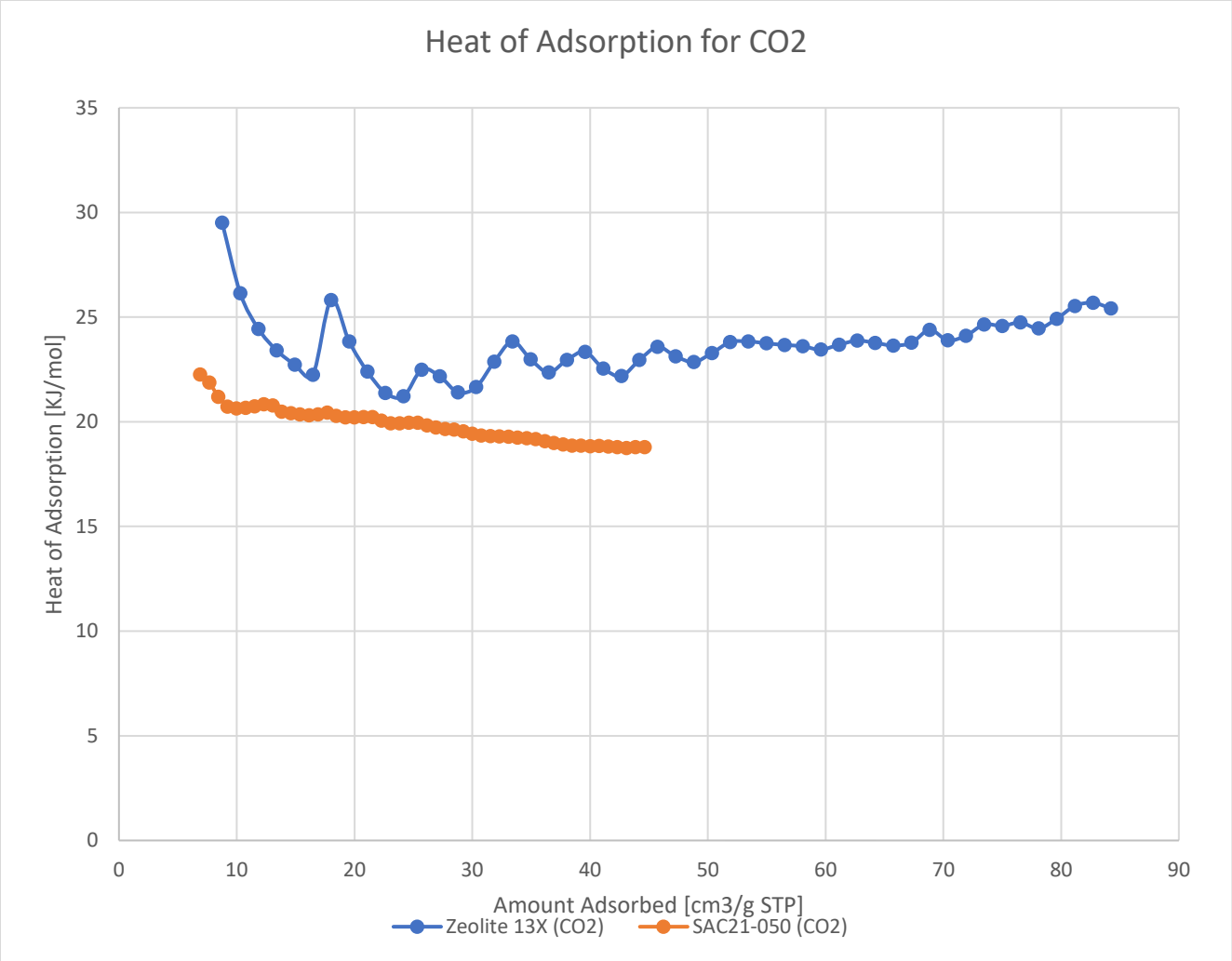

Figure 65. Heat of Adsorption of samples (CO2)

Similarly, the heat of adsorption of CO2 on Zeolite 13X shown in **figure 65** is higher than that of SAC21-050 which is consistent in the CO_2 adsorption isotherm data as well as with the predicted selectivity analysis. Zeolite shows stronger bonds when adsorbing CO_2 than that of SAC21-050 where the mean heat of adsorption was 24 KJ/mol as compared to 19 KJ/mol for SAC21-050.

5. Conclusions and Prospect for Future Work

The SEM images of all samples has been a clear representation of how the activation intensity affects the pore structure and pore sizes of the solid adsorbents. The activation intensity of the sample is directly proportional to its surface area where increasing the intensity will result in an increase in the surface area of the sample. The SEM images show clearly when the intensity increases, the shape of the pores on the surface of the samples become smaller. In the lower surface area samples, the bulky cellulose structures are still visible due to the low activation intensity that has not broken these structures down. As the intensity increases the large particles collapse and have more uniformity.

This is also verified in the pore size distribution data where the increase in intensity clearly shows an increase in micropore volume of the samples. The lowest surface area sample SAC22-029 had a micropore volume of 0.14 cm^3/g while having the peak of mesopore volume at 0.02 cm^3/g. As the intensity increases it is clear the micropore volume increased to 0.26 cm^3/g while also having a higher mesopore volume of 0.05 cm^3/g. Finally, the most important take is the clear indication of a plateau when increasing activation intensity to increase micropore volume. In the case of SAC21-050 which has the highest activation intensity, the surface area is the highest amongst the samples. However, there is a clear decrease in micropore volume from 0.26 cm^3/g to 0.17 cm3/g while having the highest recorded mesopore volume of 0.11 cm^3/g. This is because the activation intensity was high enough to collapse the micropores into bigger pores thus explaining the increase in mesopore volume. This is crucial to consider when synthesizing activated carbon samples and deciding the activation intensity, since the AC is most ideal in having the highest micropore volume as opposed to mesopores which mainly assist the diffusion of the gas towards the micropores. Even though the higher intensity results in a higher surface area, it does not necessarily mean it will be the most efficient at adsorption based on surface area alone. The zeolite sample has a surface area of 395.456 m^2/g which is the lowest among all samples, yet its pore size distribution data shows that it only consists of 0.08 cm^3/g micropore volume and no mesopore volume.

The thermogravimetric analysis has shown that the SAC21-050 was the most stable among the carbon samples which recorded the highest temperature reached before decomposing at 320^oC. Both SAC21-050 and SAC22-029 have recorded the highest ash content among the samples at 5%. The SAC21-037 sample shows similar thermal stability as that of the commercial AC where they both decompose around 290^oC. The difference among these two mentioned samples is that the SAC21-037 has 5% ash content while the commercial AC has 0.5% which is the most ideal. The Zeolite 13X sample is the most stable due to its inorganic nature and has a thermal stability of up to 900^oC and does not decompose.

It is important to note again that due to the heavy load on the adsorption instrument, two out of the five samples were chosen for adsorption measurements. It was suggested that the highest surface area carbon and the Zeolite 13X sample were the suitable choice for this study to perform the adsorption analysis.

In conclusion, Zeolite 13X has a higher selectivity and heat of adsorption towards CO_2 when compared to the SAC21-050 which is clearly confirmed by the adsorption isotherms. The pore size distribution of Zeolite consisting of only micropores has proven to be the most ideal when dealing with CO_2 adsorption as opposed to having both micropores and mesopores as in the SAC21-050. Similarly, the SAC21-050 sample has a higher selectivity and heat of adsorption towards N2 when compared to Zeolite 13X which is also consistent with the experimental data as well as the literature data. Not only is the higher adsorption capacity due to the pore size distribution of the samples, but also due to the surface chemistry and

electrostatic differences between the gas and both samples. In the case of activated carbon, the basic functional groups on the surface are linked with higher forces of attraction towards CO_2 molecules which is considered a Lewis acid. In comparison, for zeolite 13X the charge difference between the surface and the CO_2 molecules increases with decreasing Si/Al ratio. The higher heat of adsorption of CO_2 on zeolite is also verified by the sharp increase in the adsorption isotherm which shows stronger bonds forming between the surface of the zeolite and the CO_2 molecules. The linear adsorption of CO_2 on SAC21-050 suggests a lower heat of adsorption which was also proven. CO_2 adsorbs less on AC, yet it adsorbs in a smoother manner which allows the AC sample to fully desorb the CO_2 from its pores. This is consistent with the literature data which describes the strength of adsorption of CO_2 and zeolite and the difficulty of regenerating the zeolite sample after CO_2 adsorption. The Langmuir adsorption model was proven to be the least accurate when compared to the DSLF model. This highlights the importance of considering the "surface heterogeneity factor" which is taken into consideration in the DSLF model yet is not considered in the Langmuir model. Considering a heterogenous surface rather than assuming it is a homogeneous one has described the adsorption behavior more accurately in the DSLF model. The most deviation in the coefficient of determination (R^2) was seen in the CO_2 adsorption in the Langmuir model which shows that CO_2 adsorption is more dependent on the heterogeneity of the surface of the solid adsorbent than N_2 gas.

Considering the above and after careful consideration of the data presented, Zeolite 13X is superior at adsorbing CO_2 while SAC21-050 shows moderate CO_2 adsorption capabilities. However, there are some limitations for Zeolite being a hydrophilic adsorbent which favors adsorbing water or moisture that will limit its capacity for CO_2 adsorption if present. This hydrophilicity comes from the high affinity of Al atoms of the Zeolite towards water molecules. The more Al is present, the more negative charges are introduced in the zeolite structure which attracts polar molecules such as water [68]. Thus, in terms of including these solid adsorbents in a PSA system, the gas stream composition is essential to determine if water/moisture is present that can adhere the zeolite adsorption capabilities. In addition, AC and zeolites should be used in combination to minimize the need to regenerate the zeolite which is difficult and requires high energy consumption. The PSA system should be designed around the solid adsorbent and must consider the thermal stability, moisture in the gas stream, heat of adsorption of the adsorbent, selectivity of the adsorbent towards the desired gas, regeneration of the adsorbents as well as cost.

As an additional note and for future work recommendation, based on the characterization data of all the samples I predict SAC21-037 would have been a better alternative than SAC21-050 in terms of CO2 adsorption. The sample might not have the highest surface area; however, it has the highest micropore volume among all the samples. In addition, it has the least ash content amongst the AC samples (excluding the commercial AC: YEC8B) which will most likely have a better adsorption capacity. The sample also shows thermal stability like that of YEC8B. It is recommended to note the plateau effect of activation intensity on micropore generation for enhancing future synthesized activated carbon samples. In addition, reducing ash content from the synthesized samples by acid washing for the consistent removal of mineral impurities will also be an important aspect in commercializing promising activated carbons such as the SAC21-037 sample. A careful consideration of the effect of moisture in zeolite gas separation processes should be studied further.

References

1. Luberti, M. and H. Ahn, *Review of Polybed pressure swing adsorption for hydrogen purification.* International Journal of Hydrogen Energy, 2022. **47**(20): p. 10911-10933.
2. Rahimpour, M.R., et al., *The enhancement of hydrogen recovery in PSA unit of domestic petrochemical plant.* Chemical Engineering Journal, 2013. **226**: p. 444-459.
3. Hunt, A.J., et al., *Generation, capture, and utilization of industrial carbon dioxide.* ChemSusChem, 2010. **3**(3): p. 306-322.
4. Li, J.-R., et al., *Carbon dioxide capture-related gas adsorption and separation in metal-organic frameworks.* Coordination Chemistry Reviews, 2011. **255**(15): p. 1791-1823.
5. Solomon, S., et al., *Irreversible climate change due to carbon dioxide emissions.* Proceedings of the National Academy of Sciences, 2009. **106**(6): p. 1704-1709.
6. Anderson, T.R., E. Hawkins, and P.D. Jones, *CO2, the greenhouse effect and global warming: from the pioneering work of Arrhenius and Callendar to today's Earth System Models.* Endeavour, 2016. **40**(3): p. 178-187.
7. Lee, S.-Y. and S.-J. Park, *A review on solid adsorbents for carbon dioxide capture.* Journal of Industrial and Engineering Chemistry, 2015. **23**: p. 1-11.
8. Scholes, C., S. Kentish, and G. Stevens, *Carbon Dioxide Separation through Polymeric Membrane Systems for Flue Gas Applications.* Recent Patents on Chemical Engineering, 2010. **1**.
9. Ko, V.Y., et al., *Adsorption of methane on biochar for emission reduction in oil and gas fields.* Biochar, 2023. **5**(1).
10. Bao, Z., et al., *Adsorption of CO2 and CH4 on a magnesium-based metal organic framework.* Journal of Colloid and Interface Science, 2011. **353**(2): p. 549-556.
11. Shafeeyan, M.S., et al., *A review on surface modification of activated carbon for carbon dioxide adsorption.* Journal of Analytical and Applied Pyrolysis, 2010. **89**(2): p. 143-151.
12. Sircar, S., T.C. Golden, and M.B. Rao, *Activated carbon for gas separation and storage.* Carbon, 1996. **34**(1): p. 1-12.
13. Siriwardane, R.V., et al., *Adsorption of CO2 on Molecular Sieves and Activated Carbon.* Energy & Fuels, 2001. **15**(2): p. 279-284.
14. *Energetics of Gas Adsorption by Carbons: Thermodynamic Quantities*, in *Adsorption by Carbons*, E.J. Bottani and J. M.D. Tascón, Editors. 2008, Elsevier: Amsterdam. p. 53-71.
15. Soliman, n.k. and A. Moustafa, *Industrial solid waste for heavy metals adsorption features and challenges; a review.* Journal of Materials Research and Technology, 2020. **9**: p. 10235-10253.
16. Kalman, V., et al., *Hydrogen Purification by Pressure Swing Adsorption: High-Pressure PSA Performance in Recovery from Seasonal Storage.* Sustainability, 2022. **14**(21): p. 14037.
17. Alothman, Z., *A Review: Fundamental Aspects of Silicate Mesoporous Materials.* Materials, 2012. **5**: p. 2874-2902.
18. Chang, S.-S., et al., *Mesoporosity as a new parameter for understanding tension stress generation in trees.* Journal of Experimental Botany, 2009.
19. Khan, D., et al., *Formation and Distribution of Different Pore Types in the Lacustrine Calcareous Shale: Insights from XRD, FE-SEM, and Low-Pressure Nitrogen Adsorption Analyses.* ACS Omega, 2022. **7**(12): p. 10820-10839.
20. Golchoubi, A. and H. Pahlavanzadeh, *Extra-Framework Charge and Impurities Effect, Grand Canonical Monte Carlo and Volumetric Measurements of CO2/CH4/N2 Uptake on NaX Molecular Sieve.* Separation Science and Technology, 2017. **52**: p. 2499–2512.
21. Tun, H. and C.-C. Chen, *Isosteric heat of adsorption from thermodynamic Langmuir isotherm.* Adsorption, 2021. **27**(6): p. 979-989.

22. Son, K.N., et al., *Measurement and Prediction of the Heat of Adsorption and Equilibrium Concentration of CO2 on Zeolite 13X.* Journal of Chemical & Engineering Data, 2018. **63**(5): p. 1663-1674.
23. Sumida, K., et al., *Carbon dioxide capture in metal-organic frameworks.* Chemical Reviews, 2012. **112**(2): p. 724-781.
24. Ammendola, P., F. Raganati, and R. Chirone, *CO2 adsorption on a fine activated carbon in a sound assisted fluidized bed: Thermodynamics and kinetics.* Chemical Engineering Journal, 2017. **322**: p. 302-313.
25. Guo, Q., et al., *Constructing Hierarchically Porous N-Doped Carbons Derived from Poly(ionic liquids) with the Multifunctional Fe-Based Template for CO 2 Adsorption.* ACS Omega, 2021. **XXXX**.
26. Swenson, H. and N.P. Stadie, *Langmuir's Theory of Adsorption: A Centennial Review.* Langmuir, 2019. **35**(16): p. 5409-5426.
27. Kumar, V., et al., *A site energy distribution function from Toth isotherm for adsorption of gases on heterogeneous surfaces.* Physical chemistry chemical physics : PCCP, 2011. **13**: p. 5753-9.
28. Kalam, S., et al., *Surfactant Adsorption Isotherms: A Review.* ACS Omega, 2021. **6**(48): p. 32342-32348.
29. Li, P., et al., *Adsorption separation of CO2 and N2 on MIL-101 metal-organic framework and activated carbon.* Journal of the Iranian Chemical Society, 2014. **11**.
30. Acevedo, S., L. Giraldo, and J.C. Moreno-Piraján, *Adsorption of CO2 on Activated Carbons Prepared by Chemical Activation with Cupric Nitrate.* ACS Omega, 2020. **5**(18): p. 10423-10432.
31. Muttil, N., et al., *Production, Types, and Applications of Activated Carbon Derived from Waste Tyres: An Overview.* Applied Sciences, 2023. **13**(1): p. 257.
32. Marsh, H. and F. Rodríguez-Reinoso, *Chapter 2 - Activated Carbon (Origins)*, in *Activated Carbon*, H. Marsh and F. Rodríguez-Reinoso, Editors. 2006, Elsevier Science Ltd: Oxford. p. 13-86.
33. Paraskeva, P., D. Kalderis, and E. Diamadopoulos, *Production of activated carbon from agricultural by-products.* Journal of Chemical Technology & Biotechnology, 2008. **83**(5): p. 581-592.
34. Rashidi, N.A. and S. Yusup, *An overview of activated carbons utilization for the post-combustion carbon dioxide capture.* Journal of CO2 Utilization, 2016. **13**: p. 1-16.
35. Saha, B.B., et al., *Carbon Dioxide Adsorption Isotherms on Activated Carbons.* Journal of Chemical & Engineering Data, 2011. **56**(5): p. 1974-1981.
36. Idris, I., et al., *Optimizing purity and recovery of hydrogen from syngas by equalized pressure swing adsorption using palm kernel shell activated carbon adsorbent.* AIP Conference Proceedings, 2019. **2124**(1): p. 020059.
37. Dujearic-Stephane, K., et al., *The Effect of Modifications of Activated Carbon Materials on the Capacitive Performance: Surface, Microstructure, and Wettability*. Journal of Composites Science, 2021. **5**(3): p. 66.
38. Chiang, Y.-C. and R.-S. Juang, *Surface modifications of carbonaceous materials for carbon dioxide adsorption: A review.* Journal of the Taiwan Institute of Chemical Engineers, 2017. **71**: p. 214-234.
39. Samanta, A., et al., *Post-Combustion CO2 Capture Using Solid Sorbents: A Review.* Industrial & Engineering Chemistry Research, 2012. **51**(4): p. 1438-1463.
40. Boer, D.G., J. Langerak, and P.P. Pescarmona, *Zeolites as Selective Adsorbents for CO2 Separation.* ACS Applied Energy Materials, 2023. **6**(5): p. 2634-2656.
41. Guo, Y., H. Zhang, and Y. Liu, *Desorption characteristics and kinetic parameters determination of molecular sieve by thermogravimetric analysis/differential thermogravimetric analysis technique.* Adsorption Science & Technology, 2018. **36**: p. 026361741877266.
42. Chester, A.W. and E.G. Derouane, *Zeolite Characterization and Catalysis : A Tutorial*. 2009, Springer Netherlands : Imprint: Springer: Dordrecht.

43. Liang, Z., M. Marshall, and A.L. Chaffee, *CO2 Adsorption-Based Separation by Metal Organic Framework (Cu-BTC) versus Zeolite (13X).* Energy & Fuels, 2009. **23**(5): p. 2785-2789.
44. Yu, C.-H., C.-H. Huang, and C.-S. Tan, *A Review of CO2 Capture by Absorption and Adsorption.* Aerosol and Air Quality Research, 2012. **12**(5): p. 745-769.
45. Li, J.-R., J. Sculley, and H.-C. Zhou, *Metal–Organic Frameworks for Separations.* Chemical Reviews, 2012. **112**(2): p. 869-932.
46. Holder, C.F. and R.E. Schaak, *Tutorial on Powder X-ray Diffraction for Characterizing Nanoscale Materials.* ACS Nano, 2019. **13**(7): p. 7359-7365.
47. Hammond, C. and C. International Union of, *The basics of crystallography and diffraction*. 2015, Oxford University Press: Oxford.
48. Sing, K. *The use of nitrogen adsorption for the characterisation of porous materials*. in *Colloids and Surfaces A: Physicochemical and Engineering Aspects*. 2001.
49. Lehman, J.H., et al., *Evaluating the characteristics of multiwall carbon nanotubes.* Carbon, 2011. **49**(8): p. 2581-2602.
50. Jagiello, J. and M. Thommes, *Comparison of DFT characterization methods based on N2, Ar, CO2, and H2 adsorption applied to carbons with various pore size distributions.* Carbon, 2004. **42**(7): p. 1227-1232.
51. Kwiatkowski, M., V. Fierro, and A. Celzard, *Confrontation of various adsorption models for assessing the porous structure of activated carbons.* Adsorption, 2019. **25**(8): p. 1673-1682.
52. Seaton, N.A., J.P.R.B. Walton, and N. quirke, *A new analysis method for the determination of the pore size distribution of porous carbons from nitrogen adsorption measurements.* Carbon, 1989. **27**(6): p. 853-861.
53. Olivier, J.P., *Improving the models used for calculating the size distribution of micropore volume of activated carbons from adsorption data.* Carbon, 1998. **36**: p. 1469-1472.
54. Landers, J., G.Y. Gor, and A.V. Neimark, *Density functional theory methods for characterization of porous materials.* Colloids and Surfaces A: Physicochemical and Engineering Aspects, 2013. **437**: p. 3-32.
55. Corp., M.I. *An introduction to NLDFT*. Available from: https://www.micromeritics.com/Repository/Files/WP_An_Introduction_to_NLDFT.pdf.
56. Engelsen, D., et al., *Contrast and decay of cathodoluminescence from phosphor particles in a scanning electron microscope.* Ultramicroscopy, 2015. **157**.
57. Dusevich, V., *Choosing the Right Accelerating Voltage for SEM (An Introduction for Beginners).* Microscopy Today, 2010. **18**: p. 48-52.
58. Rahul, M., *Interactions, Imaging and Spectra in SEM*, in *Scanning Electron Microscopy*, K. Viacheslav, Editor. 2012, IntechOpen: Rijeka. p. Ch. 2.
59. Li, Z., et al., *Characterization of Chicken Feather Biocarbon for Use in Sustainable Biocomposites.* Frontiers in Materials, 2020. **7**.
60. Chaturvedi, S., et al., *Characterization, bioenergy value, and thermal stability of biochars derived from diverse agriculture and forestry lignocellulosic wastes.* Biomass Conversion and Biorefinery, 2023. **13**(2): p. 879-892.
61. De Witte, N., J.F.M. Denayer, and T.R.C. Van Assche, *Effect of Adsorption Duration and Purge Flowrate on Pressure Swing Adsorption Performance.* Industrial & Engineering Chemistry Research, 2021. **60**(37): p. 13684-13691.
62. Yu, X., et al., *Multi-objective optimization of ANN-based PSA model for hydrogen purification from steam-methane reforming gas.* International Journal of Hydrogen Energy, 2021. **46**(21): p. 11740-11755.

63. Zhang, N., et al., *Optimization of pressure swing adsorption for hydrogen purification based on Box-Behnken design method.* International Journal of Hydrogen Energy, 2021. **46**(7): p. 5403-5417.
64. Hauchhum, S. and P. Mahanta, *Carbon dioxide adsorption on zeolites and activated carbon by pressure swing adsorption in a fixed bed.* International Journal of Energy and Environmental Engineering, 2014. **5**: p. 349-356.
65. Gordienko, Y., et al., *Research Facilities of IAE NNC RK (Kurchatov) for Investigations of Tritium Interaction with Structural Materials of Fusion Reactors.* Fusion Science and Technology, 2020. **76**(6): p. 703-709.
66. MRB, M. *Characterization of Porous Materials*. BELSORP SERIES 2016; Available from: https://analysisdoo.com/product/belsorp-max-ii/.
67. Maulina, S. and M. Iriansyah, *Characteristics of activated carbon resulted from pyrolysis of the oil palm fronds powder.* IOP Conference Series: Materials Science and Engineering, 2018. **309**: p. 012072.
68. Banaei, A. and A. Zanj, *A Review on the Challenges of Using Zeolite 13X as Heat Storage Systems for the Residential Sector.* Energies, 2021. **14**(23): p. 8062.
69. Salgado, M., et al., *Preparation of activated carbon from babassu endocarpunder microwave radiation by physical activation.* IOP Conference Series: Earth and Environmental Science, 2018. **105**: p. 012116.
70. Masika, E. and R. Mokaya, *Preparation of ultrahigh surface area porous carbons templated using zeolite 13X for enhanced hydrogen storage.* Progress in Natural Science: Materials International, 2013. **23**(3): p. 308-316.
71. Cruciani, G., *Zeolites upon heating: Factors governing their thermal stability and structural changes.* Journal of Physics and Chemistry of Solids, 2006. **67**(9): p. 1973-1994.
72. Ismail, M., et al., *Ideal Adsorbed Solution Theory (IAST) of Carbon Dioxide and Methane Adsorption Using Magnesium Gallate Metal-Organic Framework (Mg-gallate).* Molecules, 2023. **28**(7): p. 3016.
73. Wang, S., et al., *Insights into CO2/N2 Selectivity in Porous Carbons from Deep Learning.* ACS Materials Letters, 2019. **1**(5): p. 558-563.
74. Santos, M., C. Grande, and A. Rodrigues, *Pressure Swing Adsorption for Biogas Upgrading. Effect of Recycling Streams in Pressure Swing Adsorption Design.* Industrial & Engineering Chemistry Research, 2010. **50**.
75. Cheung, O. and N. Hedin, *Zeolites and related sorbents with narrow pores for CO2 separation from flue gas.* RSC Advances, 2014. **4**(28): p. 14480-14494.
76. Hudson, M.R., et al., *Unconventional, Highly Selective CO2 Adsorption in Zeolite SSZ-13.* Journal of the American Chemical Society, 2012. **134**(4): p. 1970-1973.
77. Jiang, Q., et al., *Synthesis of T-type zeolite nanoparticles for the separation of CO 2 /N 2 and CO 2 /CH 4 by adsorption process*. 2013.
78. Krishna, R., *Diffusion in porous crystalline materials.* Chemical Society reviews, 2012. **41**: p. 3099-118.
79. Song, Z., et al., *Continuously Adjustable, Molecular-Sieving "Gate" on 5A Zeolite for Distinguishing Small Organic Molecules by Size.* Scientific Reports, 2015. **5**(1): p. 13981.

APPENDIX

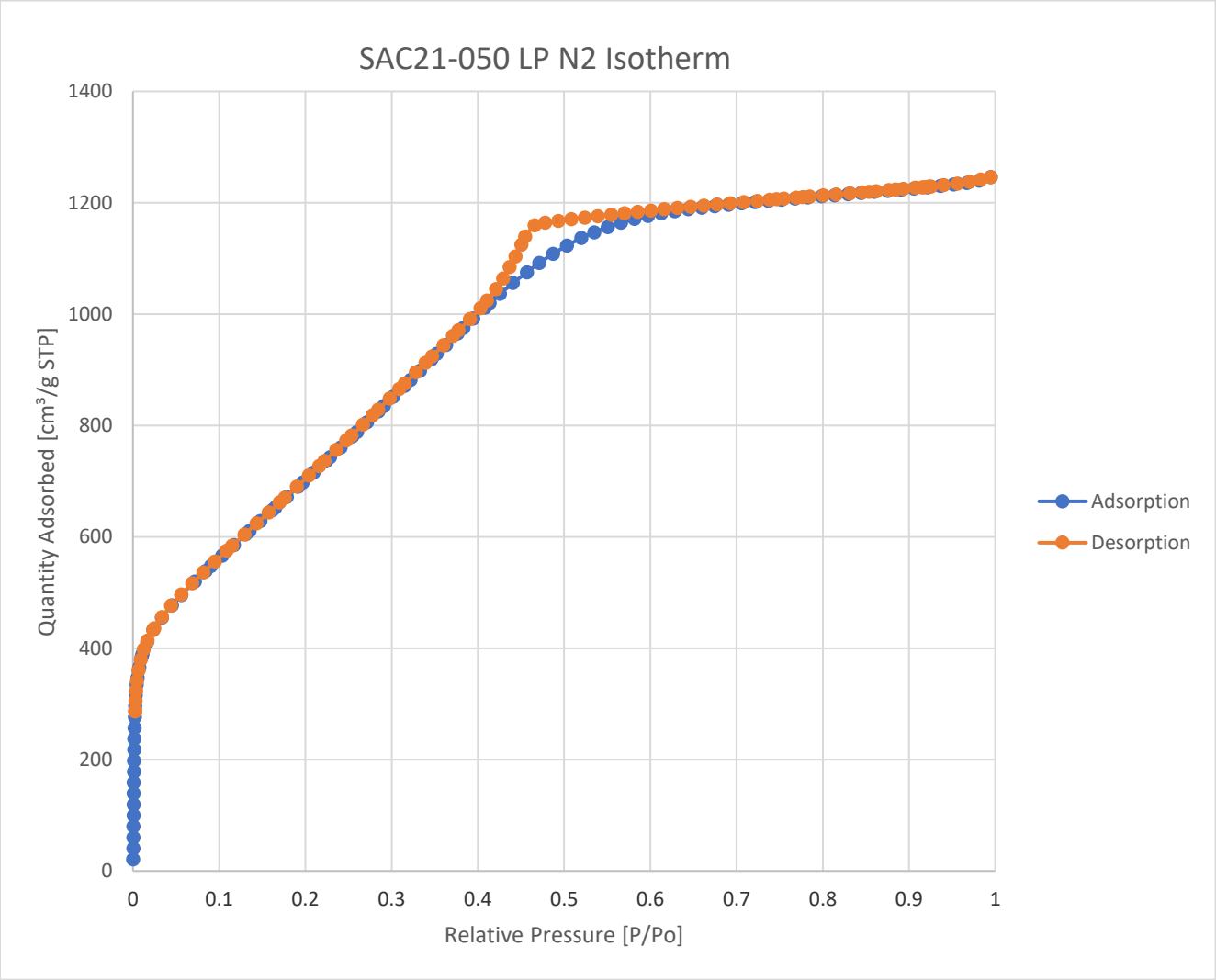

Figure 66. LP N2 Adsorption on SAC21-050 (77K)

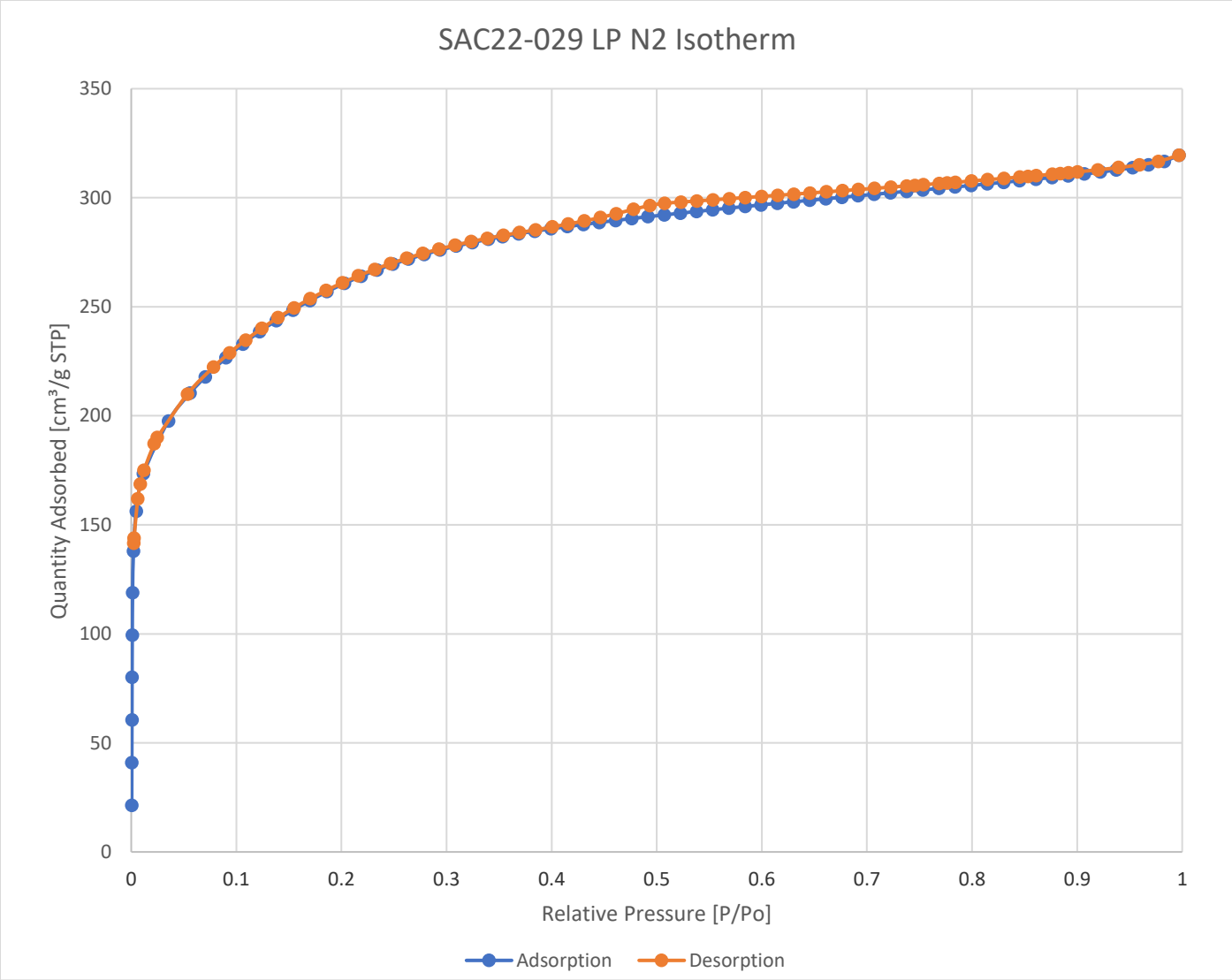

Figure 67. LP N2 Adsorption on SAC22-029 (77K)

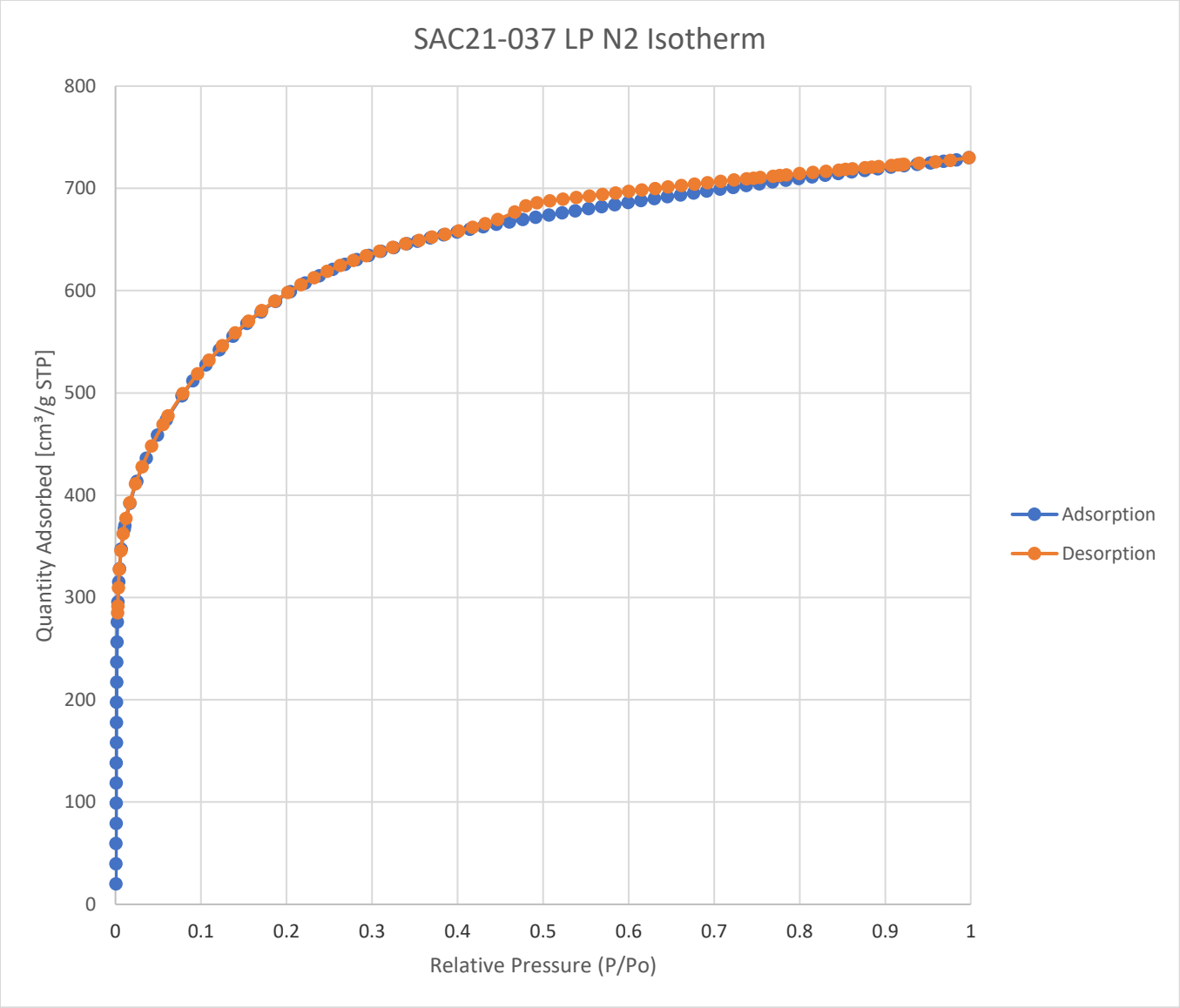

Figure 68. LP N2 Adsorption on SAC21-037 (77K)

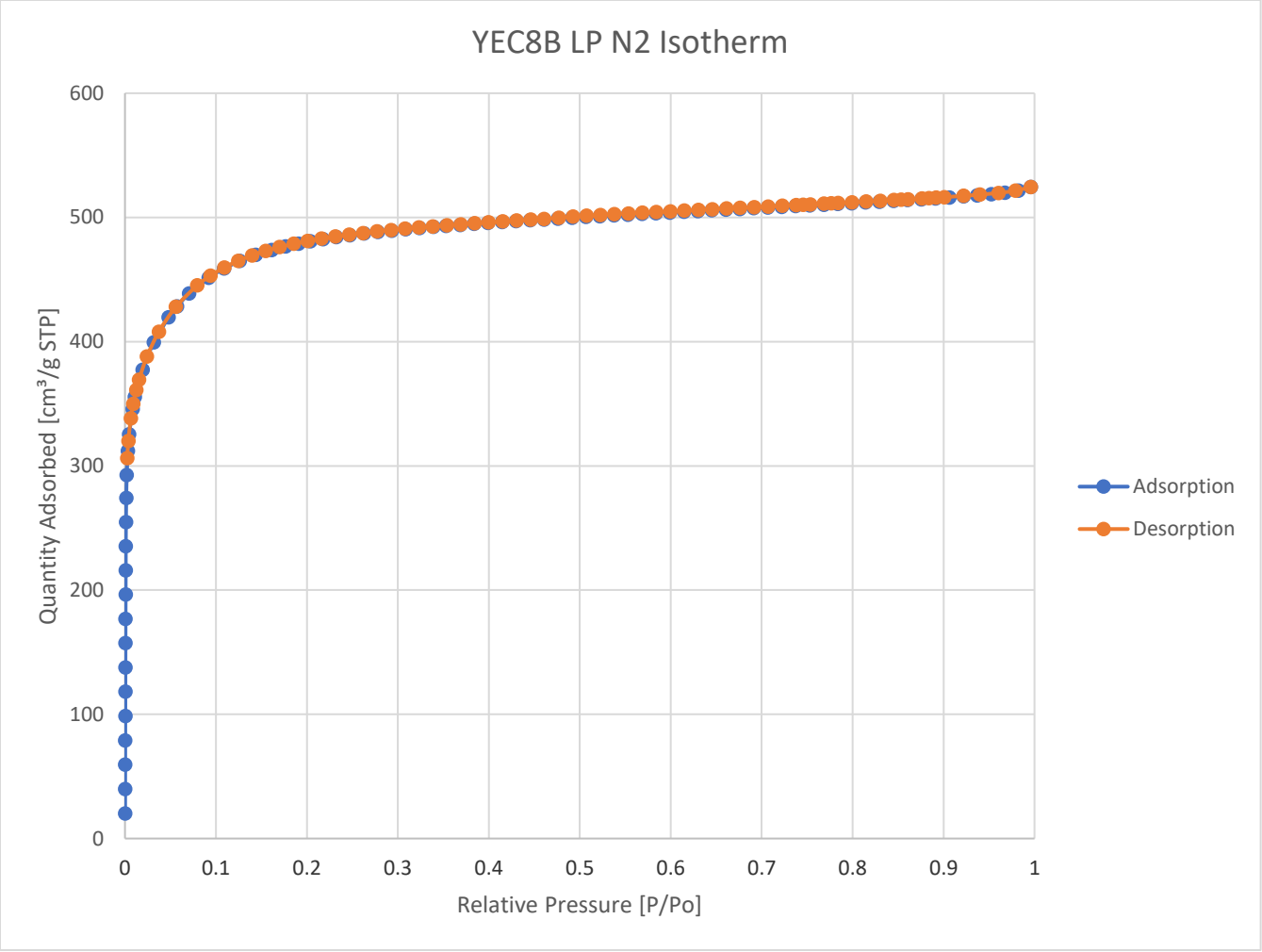

Figure 69. LP N2 Adsorption on YEC8B (77K)

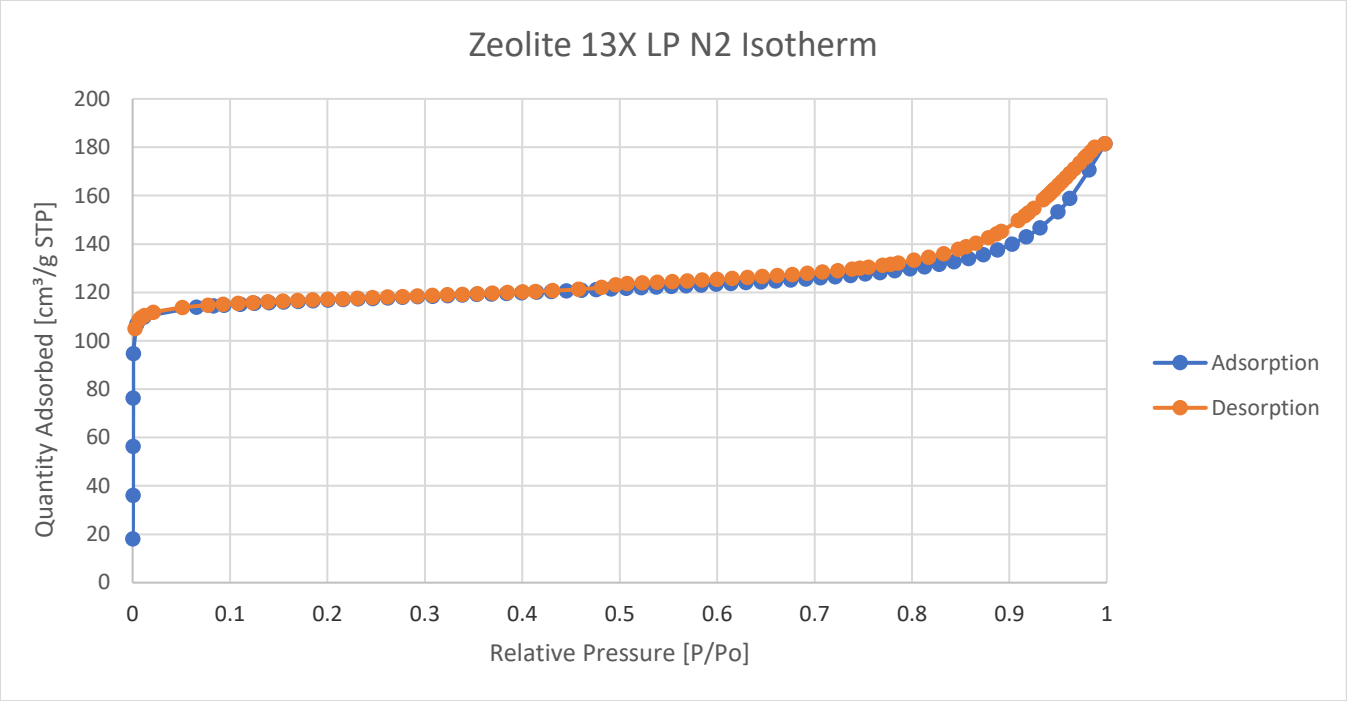

Figure 70. LP N2 Adsorption on Zeolite 13X (77K)

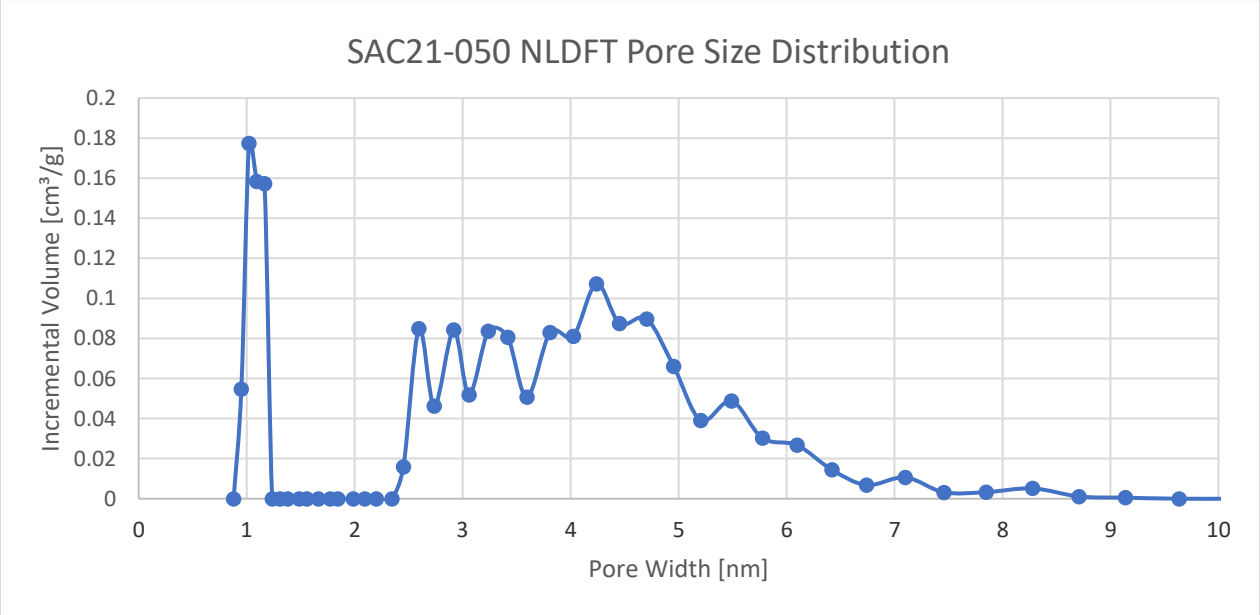

Figure 71. SAC21-050 NLDFT Pore Size Distribution

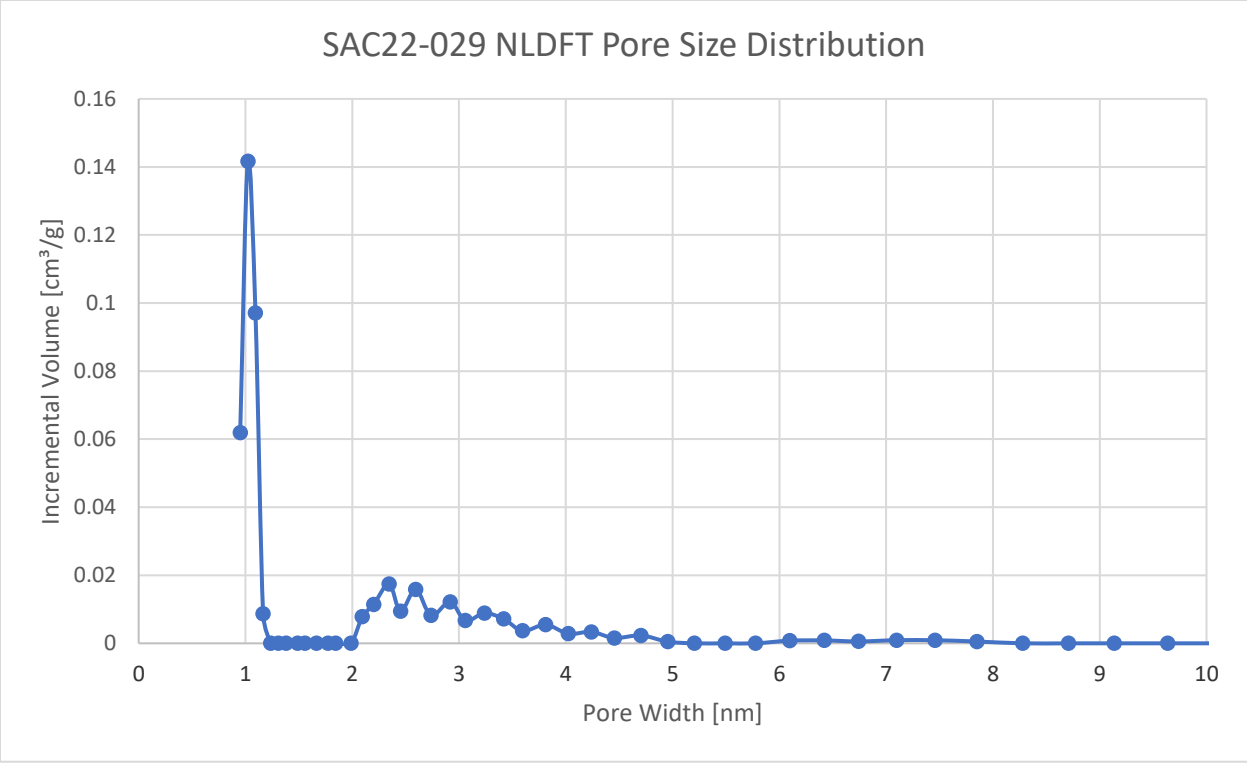

Figure 72. SAC22-029 NLDFT Pore Size Distribution

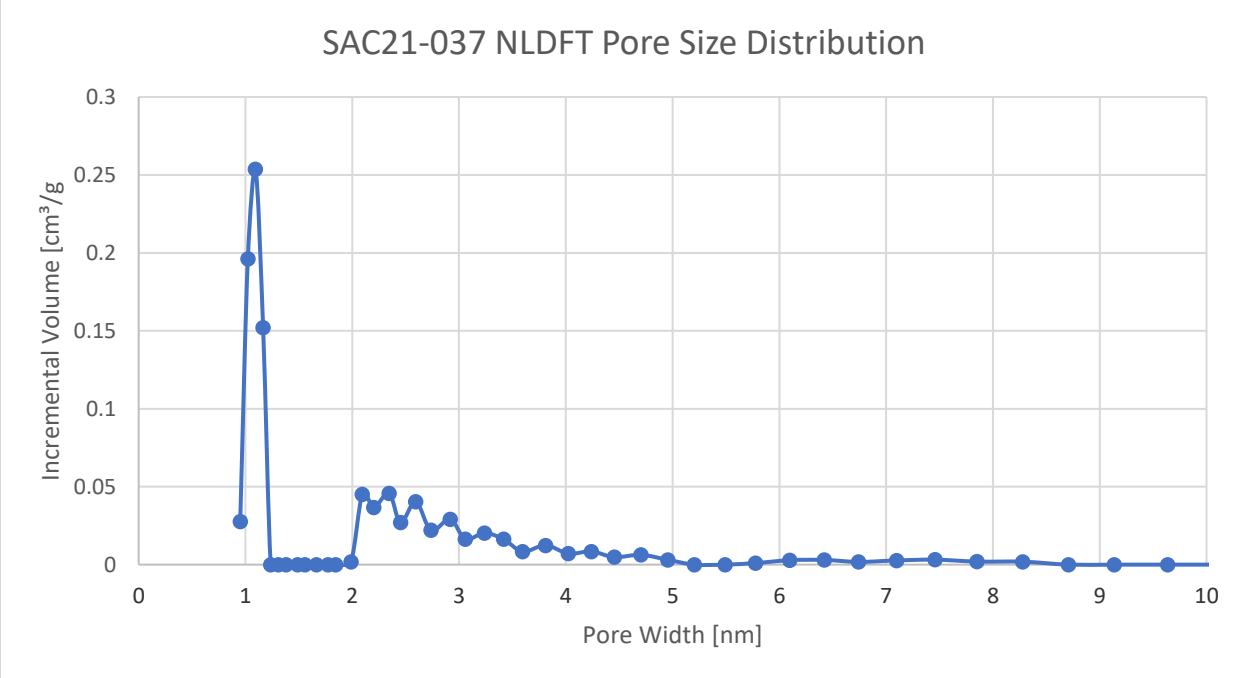

Figure 73. SAC21-037 NLDFT Pore Size Distribution

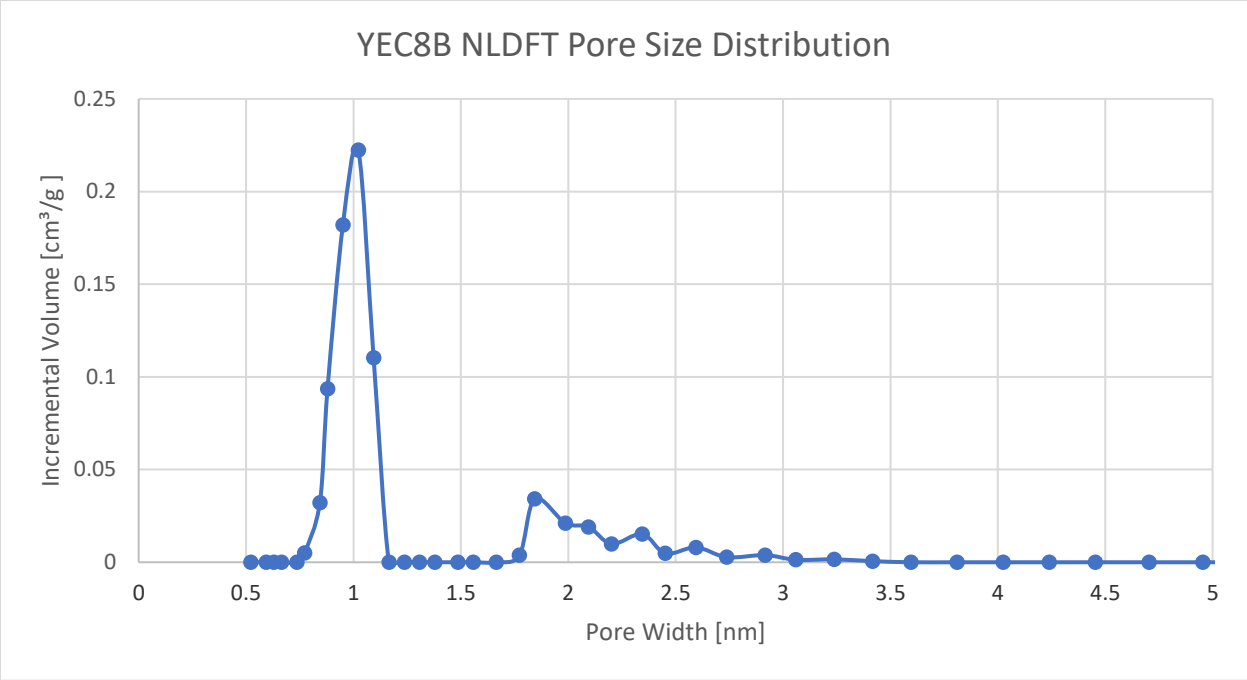

Figure 74. YEC8B NLDFT Pore Size Distribution

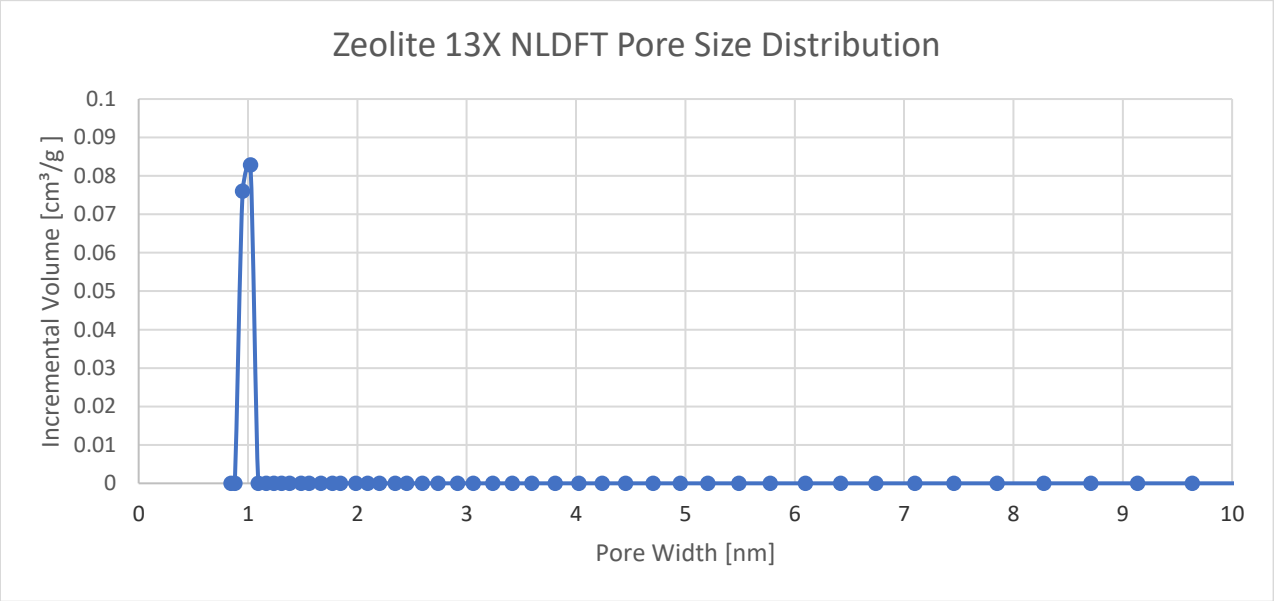

Figure 75. Zeolite 13X NLDFT Pore Size Distribution

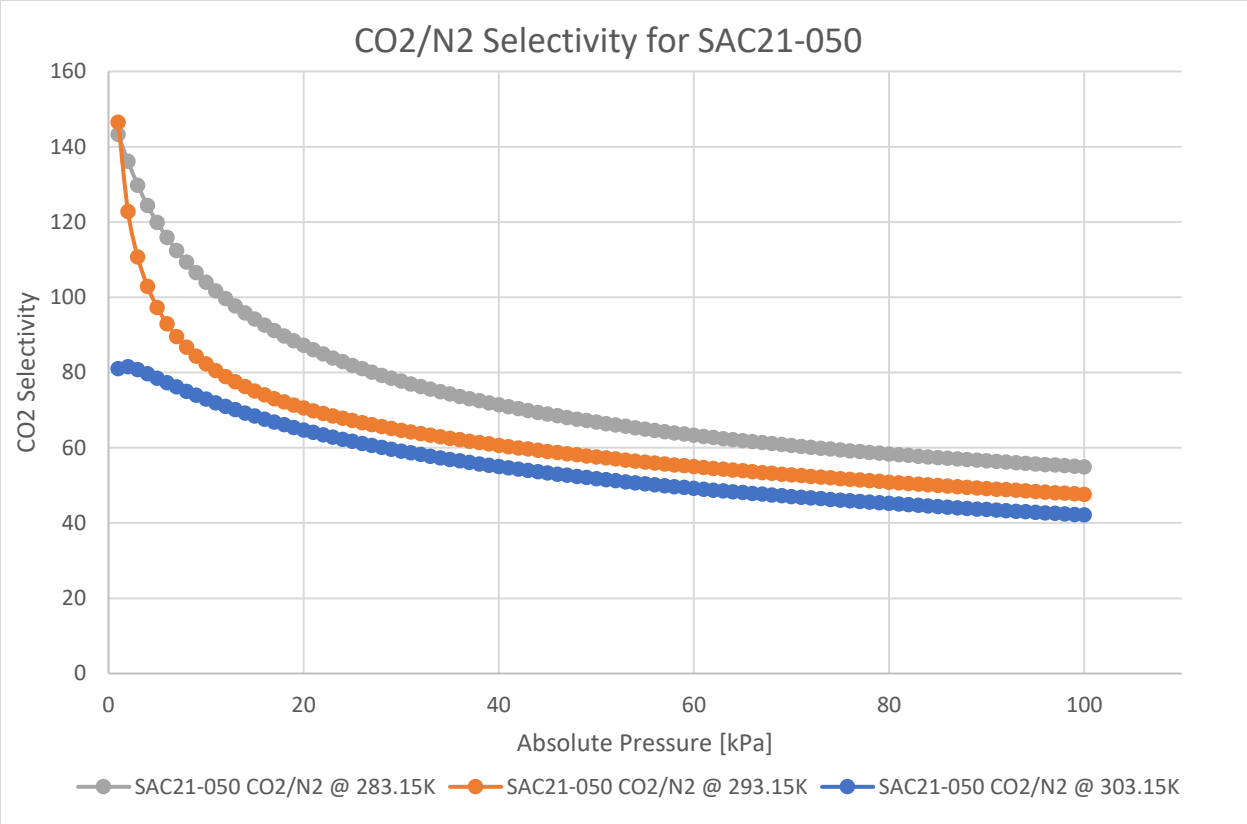

Figure 76. SAC21-050 Selectivity for CO2/N2

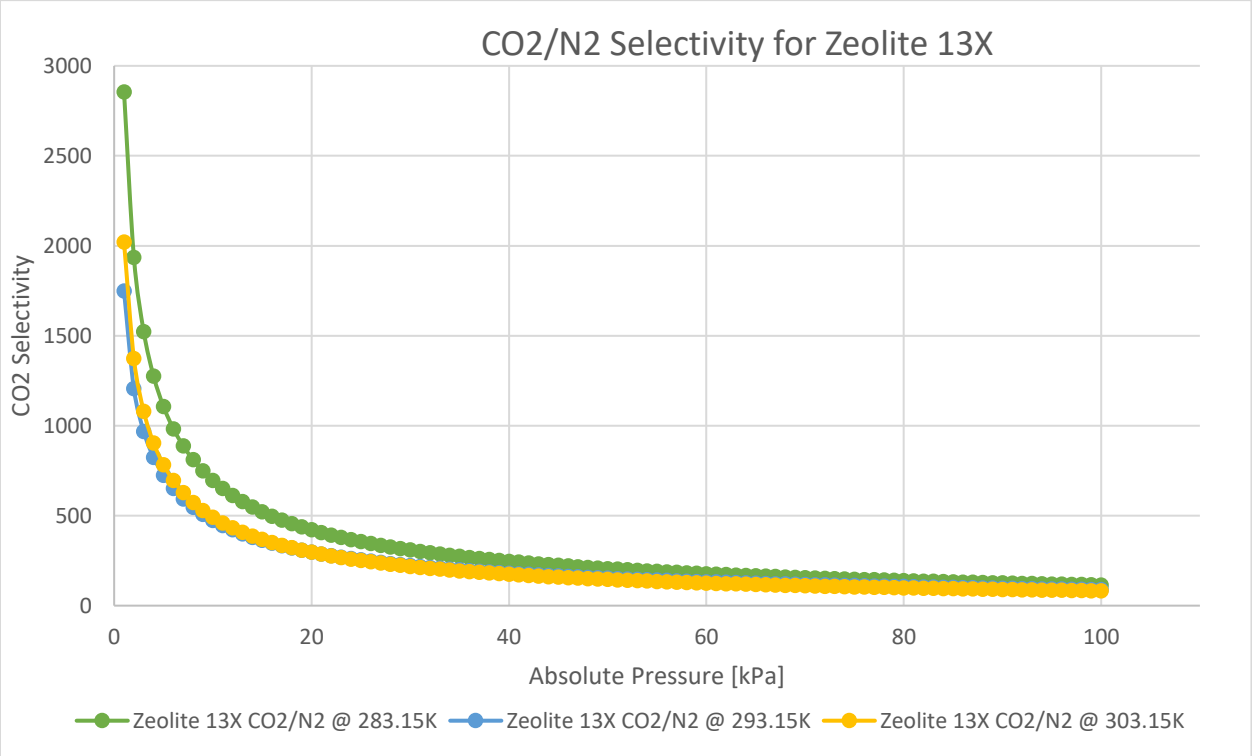

Figure 77. Zeolite 13X Selectivity for CO2/N2